Causal Representations of Rate-Independent Linear Damping and Their Applications in Low-Frequency Structures Subjected to Extreme Earthquake Events

TOHOKU UNIVERSITY

DOCTORAL THESIS

Causal Representations of Rate-Independent Linear Damping and Their Applications in Low-Frequency Structures Subjected to Extreme Earthquake Events

---

Author:
Hao LUO

Supervisor:
Prof. Kohju IKAGO

A thesis submitted in fulfillment of the requirements
for the degree of Doctor of Philosophy

in the

Department of Architecture and Building Science
School of Engineering

September, 2020

@ Technology for Optimum Mitigation Laboratory

Abstract

It is well known that rate-independent linear damping (RILD) originates from the simulation of the internal friction of engineering materials, which is thought to be one of the main sources of the inherent damping in an actual building structure. Therefore, RILD is expected to be a straightforward model for the simulation of structural inherent damping without adopting the assumption of Rayleigh damping, which has been doubted for a long time. Moreover, RILD is thought to have important applications for the seismic response control of a low-frequency structure, because it is well established that RILD can achieve effective displacement reduction at the expense of lower damping force compared with other damping types. This suggests that RILD can serve as a promising solution in protecting a low-frequency structure from excessive response displacements without increasing floor-response accelerations when the structure is subjected to extreme earthquake events, such as the future expected Nankai mega-thrust earthquake in Japan and the Cascadia earthquake in North America.

However, an ideal RILD model suffers an issue of noncausality, which hinders its use for practical applications. On the one hand, the noncausal property makes it challenging to numerically implement RILD in a nonlinear response history analysis for the performance evaluation of a building structure subjected to extreme ground motions. On the other hand, this property also suggests that it is impossible to physically realize an ideal RILD model by using real-life devices, which can be installed in an actual building structure for seismic protection purposes. In this dissertation, aimed at facilitating the practical applications of RILD in the above two situations, novel causal models which can mimic the behavior of RILD are pursued. The main contents of this dissertation are summarized as follows:

- *Chapter 1 Introduction*

  The research background of this dissertation was illustrated first, and the urgent necessity of suppressing the excessive response displacement of a low-frequency structure subjected to the future expected extreme earthquake events and the potential problems associated with the use of Rayleigh damping for the simulation of structural inherent damping were pointed out. As a potential solution to addressing these issues, RILD was then introduced and reviewed in detail. It follows the introduction of the purposes and structure of this dissertation.

- *Chapter 2 A Simple Model to Utilize the Benefit of RILD in Low-frequency Structures*

  The behavior of RILD in low-frequency structures subjected to strong ground motion was discussed first. Comparisons between the transfer functions in terms of displacement and damping force for RILD and linear viscous damping (LVD) separately incorporated into a single-degree-of-freedom (SDF) system were made. It is suggested that RILD generates lower floor-response accelerations compared to LVD without increasing the response displacements, when they are separately incorporated into a low-frequency structure subjected to strong ground motion, which contains dominating

high-frequency components. A base-isolated five-story building structure was used as an analytical example, and the benefits of RILD were illustrated by using the results of incremental dynamic analyses and parametric studies.

In order to utilize the benefit of RILD for practical applications, a causal model for mimicking the behavior of RILD was derived and it can be passively implemented by using a Maxwell and a negative stiffness (MNS) elements connected with each other in parallel. Comparisons between the seismic responses of structures incorporated with the MNS and LVD models showed that when excited by high-frequency-dominated ground motion, the structure equipped with the proposed MNS model yielded lower damping forces than those with LVD model. However, the two structures exhibited similar isolator displacements. Moreover, the performance of the MNS model was not compromised, even when excited by ground motion containing low-frequency components. These comparisons exemplified the feasibility of the proposed method to mimic RILD in reducing the response displacement without increasing floor-response acceleration.

A linear negative stiffness element (LNSE) is thought to be essential in order to passively realize a causal model that mimics the behavior of RILD. A straightforward way to creating an LNSE is achieved by equivalently reducing the horizontal stiffness of primary structure (or isolators). Otherwise, a design example of negative stiffness device was also given, and it provided an alternative for approximating a physical LNSE within the displacement range of interest, making the proposed MNS model more attractive for mimicking the performance of RILD. The MNS model is expected to be a viable option for improving the seismic performance of low-frequency structures subjected to strong ground motion.

- *Chapter 3 A Unified Framework of Causal RILD Models*

  For reference, some representative existing RILD models were first reviewed in detail. It followed that a novel model which can mimic the behavior of RILD was proposed in the frequency domain by generalizing a bilinear digital filter into a fractional-order filter, and its causality was confirmed. In terms of physical representation of the proposed model, a mechanical model consisting of a fractional-order Maxwell and a negative stiffness (FMNS) elements coupled in parallel was constructed, which can be considered as a generalization of the MNS model proposed in Chapter 2. Both passive and semi-active methods were proposed to realize the FMNS model by using real-life devices for practical applications.

  Comparisons between the FMNS model with those of the existing causal models for RILD were made, and some subtle relationships between the FMNS model with those existing models were revealed and proved. It was suggested that the FMNS model can be considered as a unified causal model for RILD because it can encompass the other existing causal models. On the basis of the newly revealed relationships in this study, along with those well established ones, a unified framework of causal models for mimicking the behavior of RILD was developed.

In order to numerically implement the FMNS model in the time domain, a so-called L1-algorithm-based internal variable method (labeled as L1-algorithm) was developed by directly calculating the fractional derivative. Such a method was thought to be convenient for application, because it required little calculations for the parameter estimation, and could also be readily embedded into established numerical integration schemes for response history analyses. Moreover, the computational efficiency of the developed method can be largely improved by applying the fixed memory principle without significant loss of accuracy. Its effectiveness for a nonlinear response history analysis was verified by using a base-isolated benchmark structure as an analytical example. Comparisons between the seismic responses of the base-isolated structure incorporated with different RILD elements were made, and it was further shown that the MNS model can be used as a simpler option to mimic the behavior of RILD for use in a nonlinear base-isolation system without significantly compromising the seismic performance, when compared with other more complicated models in the unified framework.

- *Chapter 4 An Efficient Method for a Structural Model Incorporated with RILD*

  For further accelerating the dynamic analysis of a structure with the FMNS model, a recursive method was developed by using a Prony series to approximate the damping kernel function in terms of Mittag-Leffler relaxation function, which can avoid the calculation of the fractional derivative for response history analyses. For practical applications, both time- and frequency-domain methods were discussed to estimate the characteristic parameters of a Prony series. The developed recursive method can be readily embedded into the established numerical integration schemes for nonlinear response history analyses, and it was also shown that this recursive method can be more computationally efficient than the L1-algorithm-based method without compromising the simulation accuracy.

  Furthermore, the feasibility of the FMNS model to causally mimic the behavior of RILD for simulating the structural inherent damping was verified by using a ten-story benchmark building structure as an analytical example. First, linear time history analyses were conducted to examine the seismic performance of the example structure separately incorporated with the ideal RILD, Nakamura, and FMNS models, respectively. Comparisons between the seismic responses of differently damped structures suggested that the FMNS model can be used as a competitive candidate of mimicking the behavior of ideal RILD for simulating the structural inherent damping when compared with the Nakamura model. Furthermore, the FMNS model was compared with the tangent stiffness proportional and nonlinear modal damping models when they were incorporated into the example structure with the nonlinearities of structural stiffness elements into account. It was suggested that the FMNS model can be superior to the nonlinear modal damping model in terms of computational efficiency without compromising the accuracy.

Lastly, parametric studies were conducted to investigate the effect of the tunable parameter on the seismic performance of the FMNS system. It was suggested that in terms of simulating the structural inherent damping in an MDF structure, a small fractional tunable parameter was preferred for the FMNS model to provide an improved approximation of the ideal RILD model.

- *Chapter 5 Conclusions and future work*

  On the basis of the research work done in the previous chapters, some conclusions were made and further challenges to be overcome in the future were pointed out in Chapter 5.

Acknowledgments

Time really flies! It has been three years since I came to study at the present laboratory, which has been well known with its very long history in the field of earthquake engineering. Carrying a high responsibility along with this great honor, I started the doctoral program under the guidance of Prof. Ikago, who has a very deep impact on me, not only in the aspect of research activity, but also in the aspect of dealing with people. In the past years, I benefited a lot from the professional guidance of Prof. Ikago, particularly when I was missing in the world of mathematics, Prof. Ikago always helped me to relocate myself in the physical world and guided me to find a more promising direction to the end. Because of his continuous help and support, I never felt cold and alone. I really appreciate it a lot and would like to express my special thanks to him. I am also very grateful to Prof. Inoue for his valuable suggestions to the research work and future career in the past years.

I would also like to thank Prof. Maeda, Prof. Ohno, and Prof. Xue for being the referees of this dissertation. Their suggestive comments and advices not only contributed to the improvement of the present work in both length and depth, but also helped me to recognize the large extendability and high potential of this research topic for the future practical engineering applications.

With the financial support provided by the Tohoku-Tsinghua collaborative research fund, I studied in Prof. Ji's laboratory at Tsinghua University for three months. Here, I would like to express my gratitude for the helps from Prof. Ji. I would also like to express my thanks for the helps from Prof. Zhang at Tongji University, Prof. Hori at Tohoku Institute of Technology, Prof. Kanno at Akita Prefectural University, Prof. Phillips at University of Florida, Prof. Ikenaga at Kansai University, Prof. Enokida and Prof. Guo at Tohoku University, Prof. Cao at Tohoku Institute of Technology.

In the past years, I have obtained many sweet memories while I stayed with other members in our laboratory. These pleasant and great moments mean a lot to me and will never vanish in my deep heart. Here, I would like to express my thanks to Dr. Li, Dr. Chong, Mr. Sasaki, Mr. Higano, Mr. Matsumoto, Mr. Zhang, Ms. Kurashige, Mr. Kikuchi, Ms. Ban, Mr. Liu, Mr. Hanzawa, Mr. Yasuda, Mr. Ito, Mr. Fukuda, Mr. Wang, Mr. Kamizawa, Mr. Kobayashi, Mr. Kezuka, and so on. I also had many unforgeable experiences with many good friends in Sendai and other places, but I would like to make apologies to them that I cannot list all their names in this short acknowledgment.

I would also like to express my thanks for the financial supports from the President Fellowship Committee of Tohoku University, the Honjo International Scholarship Foundation (HISF), and also the Japanese Society for Promotion of Science (JSPS). These supports really made my life in Sendai much easier.

Lastly, I would like to thank all my family members for firmly supporting me to pursue further study in Japan. They provide me with the source of strength to overcome any challenge in the research activities and dairy life.

Hao LUO

August 7th, 2020

Contents

List of Figures

List of Tables

List of Abbreviations

RILD	**R**ate-**I**ndependent **L**inear **D**amping
LVD	**L**inear **V**iscous **D**amping
SDF	**S**ingle **D**egree of **F**reedom
MDF	**M**ultiple **D**egree of **F**reedom
TMW	**T**uned **M**axwell-**W**iechert
MNS	**M**axwell-**N**egative-**S**tiffness
FMNS	**F**ractional-**M**axwell-**N**egative-**S**tiffness
NSD	**N**egative **S**tiffness **D**evice
LNSE	**L**inear **N**egative **S**tiffness **E**lement
MHF	**M**odulated **H**omogeneous **F**riction
JMA	**J**apan **M**eteorological **A**gency
RMS	**R**oot **M**ean **S**quare
PGV	**P**eak **G**round **V**elocity
PGA	**P**eak **G**round **A**cceleration
IDA	**I**ncremental **D**ynamic **A**nalysis
SF	**S**cale **F**actor
NS	**N**orth-**S**outh
EW	**E**ast-**W**est
HD	**H**ysteretic **D**amper
FIR	**F**inite-duration **I**mpulse **R**esponse
FFT	**F**ast **F**ourier **T**ransform
DFT	**D**iscrete **F**ourier **T**ransform
SVD	**S**ingular **V**alue **D**ecomposition
TSP	**T**angent-**S**tiffness-**P**roportional
NLM	**N**on-**L**inear-**M**odal
CPU	**C**entral **P**rocessing **U**nit

Chapter 1

Introduction

1.1 Research background

1.1.1 Lessons form the 2011 Tohoku earthquake

In the afternoon of March 11, 2011, the eastern Japan was hit by a devastating earthquake (hereafter referred to as the Tohoku earthquake) with the moment magnitude of 9.0, which is the strongest earthquake in Japan since the 1923 Kanto earthquake [1]. Huge losses of property and life were caused by this earthquake and the tremendous tsunami.

Strong earthquake observation data show that the Tohoku earthquake induced severe ground motions with high intensity and long duration, e.g., a ground motion recorded in the K-NET Tsukidate station in Kurihara city, Miyagi prefecture, has a maximum recorded acceleration of *3 000 gal*, and a duration as long as nearly *6 minutes* [2]. The damages directly caused by these ground motions were not thought to be as severe as those caused by the tsunami, partly because the dominant period of the main earthquake was at the range of 0.2 to 1.0 second. However, the following issues during the Tohoku earthquake still should be paid enough attentions:

1) *Large isolator deformations in seismically isolated structures*

   Large isolator deformations and resulting damages in lead dampers incorporated into the isolation layer were reported in seismically isolated structures during the Tohoku earthquake. For example, a maximum isolator deformation as large as *0.355 m* was observed in a seismically isolated building, which is located 1.0 km away from the K-NET MYG013 station in Sendai city, Miyagi prefecture [3]. These large deformations occurred in the isolation layer may cause damages of supplemental damping devices, or severe impact between the isolated structure and the moat wall, consequently resulting in failure of the isolation system. For example, the *failure of a lead damper in a seismically isolated hotel building* near the K-NET Furukawa station (MYG006) in Osaki city, Miyagi prefecture was reported due to the large deformation during this huge earthquake [4].

2) *Large-amplitude long-duration vibration of super high-rise building structures*

   Large-amplitude long-duration vibration of super high-rise building structures were observed in mega cities like Tokyo and Osaka [1], which are relatively far away from

the epicenter. For example, a 54-story building (height = 223 m, fundamental natural period = 6.2 second in the short-span direction) retrofitted with passive oil dampers including in the supporting bracing system in Shinjuku, Tokyo experienced a top-story displacement of 0.54 m during the Tohoku earthquake, and the duration of vibration was reported to be over *13 minutes*. Another example is a 55-story super high-rise building in Osaka (height=256 m, fundamental natural period = 5.3 second in the short-span direction), which experienced a top-story displacement as large as *1.4 m* in the short-span direction during the Tohoku earthquake, even though it is located far away from the epicenter (about 800 km).

The above observations made it urgently necessary to develop techniques to effectively suppress the large deformation of low-frequency structures (e.g., seismically isolated or super high-rise buildings) subjected to large-amplitude long-duration ground motions induced by extreme earthquake events. On the basis of the experience obtained in the past earthquake events, the community of earthquake engineering recently started to concern that low-frequency structures, like seismically isolated or super high-rise building structures, might suffer excessive response displacements beyond the design limit in the event of an extreme earthquake, such as the future expected Nankai mega-thrust earthquake in Japan and the Cascadia earthquake in North America. These excessive deformations may cause the damages of isolators and/or supplemental damping devices, and even result in impact between the isolated structure and the moat wall. Consequently, damages of structural and/or nonstructural components at the upper floors of the structure may occur. This research background is illustrated in Fig.1.1.

Indeed, in order to suppress those excessive response deformations in a seismically isolated structure, more damping can be supplemented into the isolation layer by simply increasing the number of traditional damping devices (e.g., oil damper, or metal yielding dampers). However, excessive damping through high damping force provided by these damping devices may result in increased floor-response accelerations, and consequently compromises the effect of base isolation. *To overcome this contradiction, novel damping devices need to be developed so that both isolator deformations and floor-response accelerations in seismically isolated structures can be simultaneously controlled*, as shown in Fig.1.2. Rate-independent linear damping (RILD) is thought to be one of the most promising solutions to achieving this goal [5], because it can benefit a low-frequency structure by reducing the response displacement without increasing the floor-response acceleration when the structure is subjected to the ground motion dominated by high-frequency components [6].

Despite of its important application for seismic protection of low-frequency structures, RILD is also expected to be a straightforward model for the simulation of structural inherent damping without adopting the mathematically convenient assumption of Rayleigh damping, as discussed below.

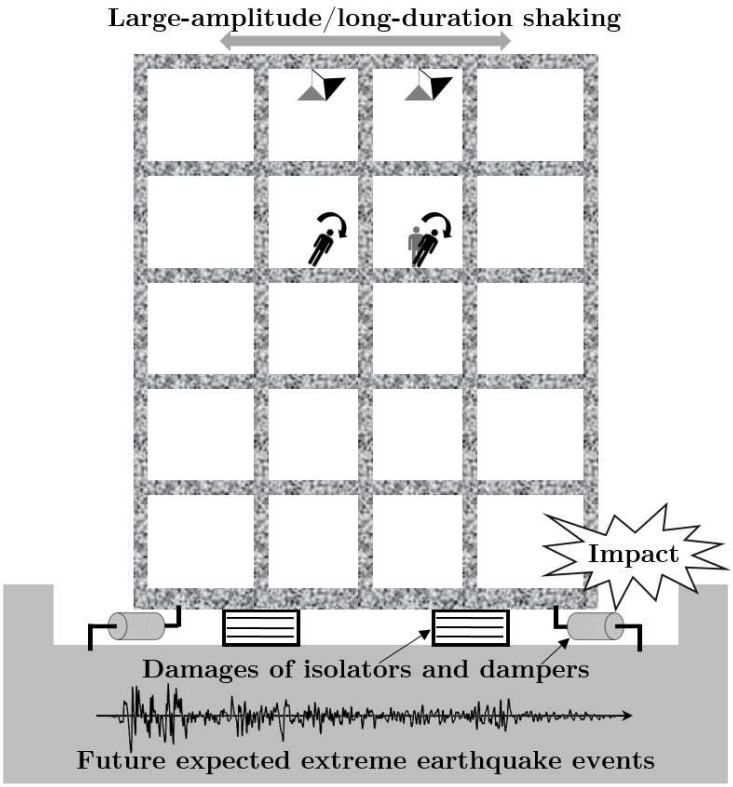

FIGURE 1.1: Research background of this dissertation

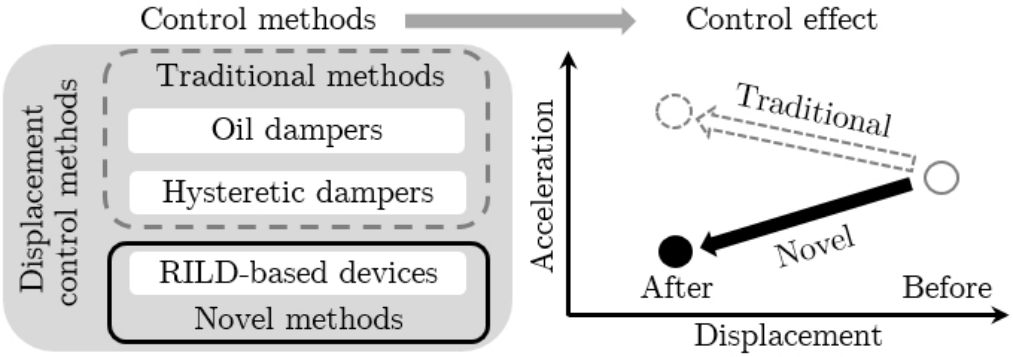

FIGURE 1.2: Application of RILD for seismic control of structural responses

1.1.2 The simulation of structural inherent damping

In structural dynamics, damping is an idealized concept to represent a process by which vibration steadily diminishes in amplitude [7]. Since its invention, damping has been one of the most popular research topics in many engineering fields and several thousands of publications on damping have appeared [8]. In many practical applications, damping effect is an unignorable and even critical factor, and thus should be carefully considered and properly simulated.

Several linear damping models are available to represent the damping effect for engineering applications. A linear viscous damping (LVD) model has been often used to represent damping since its use by Lord Rayleigh [9]. This may be partly because it provides great convenience to the mathematical analyses of structure in both the frequency and time domains. However, the energy dissipated by this model in one cycle of sinusoidal deformation is proportional to the vibration frequency, which violates the experimental results of many engineering solid materials.

Indeed, in the structural level, the damping mechanism becomes much more complicated than that in the level of material. The sources of the inherent damping of an actual building structure may include the internal friction in the structural material, connections, and nonstructural components, opening and closing of microcracks in concrete, and so on. When used in a single-degree-of-freedom (SDF) system, the LVD model may be thought to be appropriate for a general simulation of the structural inherent damping due to various sources, if an equivalent viscous damping coefficient is properly defined so that the dissipated energy is equal to that dissipated in a vibration cycle of the actual structure. However, such a method is difficult to be applied for simulating the structural damping in a multi-degree-of-freedom (MDF) system, especially in an actual multi-story or high-rise building structure. Unlike the stiffness characteristic, the damping characteristics of a structural element are poorly understood, and thus, in most applications, it is impractical to measure the damping coefficients of individual structural elements or calculate damping coefficients from the dimensions and other physical properties, and then assemble those coefficients for construction of the damping matrix, as one does for the stiffness matrix.

A more practical method of simulating the structural inherent damping in an MDF system is achieved by generally specifying the numerical values of modal damping ratios, which may be properly estimated from experimental data. Those modal damping ratios may be sufficient for dynamic analyses of those classically damped structures by using the modal superposition method. However, for those non-classically damped structures or for nonlinear simulation problems, the classical modal superposition method doesn't apply and in such cases, a properly constructed damping matrix is of fundamental necessity for step-by-step response history analyses.

Several methods are well established for construction of the damping matrix of an MDF structural system. The mass- and stiffness-proportional damping models are thought to be inappropriate for simulating the structural inherent damping, because the variations of the estimated modal damping ratios from the above models are not consistent with the experimental data that indicate roughly the same damping ratios for several vibration modes of structure [7]. Consisting of both mass- and stiffness-proportional parts, the Rayleigh damping provides entrances to specify the modal damping ratios at arbitrary two modes, which makes it possible to define the modal damping ratios somewhat consistent with the experimental data. If the frequency range, over which the nearly constant modal damping ratios are specified, is thought to be narrow, one may apply the Caughey damping to extend it by specifying the damping ratios at more modes, but this may result in a numerically ill conditioned problem and also significantly increase the computational burden due to the

resulting full damping matrix. Therefore, Rayleigh damping is often assumed in practical applications.

However, in the past decades, many papers [10–18] have been reported on the potential problems associated with the use of Rayleigh damping for simulation of structural inherent damping. For example, Bernal [10] warned that spurious damping forces may be yielded if Rayleigh damping is used for inelastic analyses of a structural system with massless degree-of-freedoms. Hall [11] pointed out that Rayleigh damping may result in an nonconservative analysis due to the unrealistically overestimated damping forces during inelastic response, and suggested a remedy to overcome this problem by imposing bounds on the damping forces. Recently, Chopra and McKenna [14] recommended a viscous damping matrix which is constructed by superposition of modal damping matrices for nonlinear response history analyses so that the spurious damping forces can be eliminated.

Alternatively, to comply with the experimental data that indicate roughly the same damping ratios for several vibration modes of structure [7], one may use RILD to construct the damping matrix for simulation of the structural inherent damping. Such a method is thought to be more straightforward than the above methods (i.e., Rayleigh damping, Caughey damping, or superposition of modal damping matrices), because RILD indeed originates from the simulation of the internal friction of solid materials, which is one of the main sources of the structural inherent damping. Moreover, the resulting damping matrix can be readily constructed because it only consists of a stiffness-proportional part, and more importantly, it is independent on the modal characteristics of the structure. Therefore, no effort is required to calculate the structural modal characteristics, which may be computationally expensive for large-scale structures.

In summary, Fig. 1.3 classifies different types models for the simulation of structural inherent damping. Except for the above mentioned damping models, some causal approximated models of RILD are also shown and to be introduced in the next section.

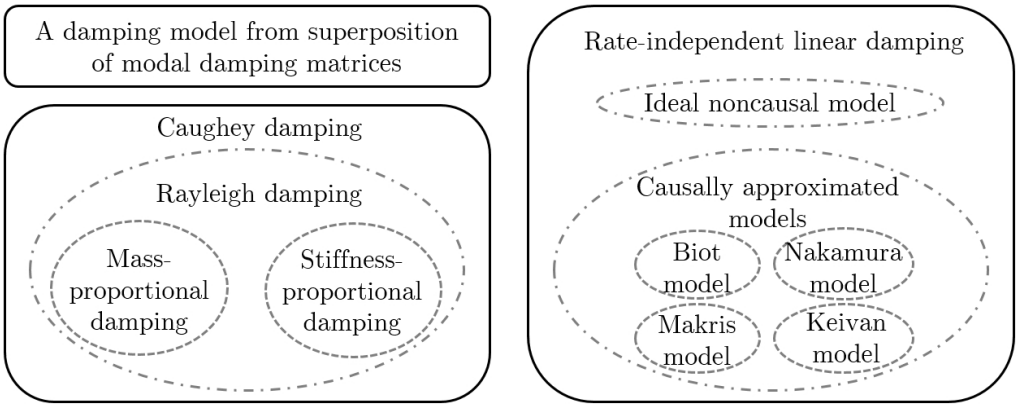

FIGURE 1.3: Different models for simulating structural inherent damping

1.2 State of the art of rate-independent linear damping

It is well known that RILD originated from the simulation of internal friction in engineering materials. Actually, it is dated back to the late of 1800s that the internal friction in solids has been treated the same as the LVD in viscous fluid. After his experiments on the torsional vibration of wires, Lord Kelvin [19] concluded that the internal friction in a vibrating elastic solid doesn't follow the law of viscosity of fluids, i.e., a simple vibrator experiences a resistance force simply proportional to the velocity of its motion. Similar observations were also later reported by Hopkinson and Williams [20], Rowett [21], Lindsay [22], and others.

In 1927, Kimball and Lovell [23] reported that, from tests on eighteen solids with different physical properties, the energy loss per sinusoidal strain cycle is proportional to the square of strain amplitude, but independent on the strain rate over a considerable frequency range. Similar observations were also reported and confirmed by Lazan [24]. These early observations led to the introduction of an idealized concept of rate-independent linear damping (RILD) to represent the internal friction in solids, also referred to as structural damping, complex stiffness, linear hysteretic damping, or ideal hysteretic damping [25–28]. In this dissertation, the terminology of "rate-independent linear damping" is preferred over the other candidates, because it can transfer the clear damping characteristics, and avoid unnecessary confusions with the existing damping models in the field of earthquake engineering (e.g., hysteretic damping is often interpreted as the energy dissipation behavior of a metal yielding damper). After the discovery of Kimball and Lovell, the concept of RILD was successfully applied to aircraft flutter problems for several decades [29, 30].

In the field of structural dynamics, a large number of publications have been reported on RILD in the past decades. Crandall [28] investigated the dynamic responses of structure incorporated with RILD under an impulse and a stationary random excitations, and found that a precursor response occurs before the application of the impulse, which implies that an ideal RILD model is noncausal. The first causal model which exhibits nearly rate-independent dissipation behavior was proposed by Biot [31]. Caughey [32] investigated the dynamic responses of structure with the Biot model, and suggested that this model can be constructed by arranging a spring element and an infinite number of Maxwell elements connected with each other in parallel, as shown in Fig. 1.4. Such a model is sometimes referred to as a Maxwell-Wiechert model [33, 34]. It should be noted that some attempts were also made to approximate the behavior of RILD by adopting the fractional derivative concept [35, 36].

Furthermore, an analytical expression of the impulse response function of an system with ideal RILD was derived by Milne [37]. On the basis of convergent calculations using the Hilbert transform, a time-domain iterative technique for response analyses of structures with ideal RILD was proposed by Inaudi and Kelly [38], and later by using analytical (complex-valued) signals, a less computationally demanding method was proposed by Inaudi and Makris [39]. However, in both methods, the explicit use of the Hilbert transform are necessary, and this may compromise their capabilities of dealing with those cases where residual displacements occur in nonlinear structural systems. More specifically, to apply the

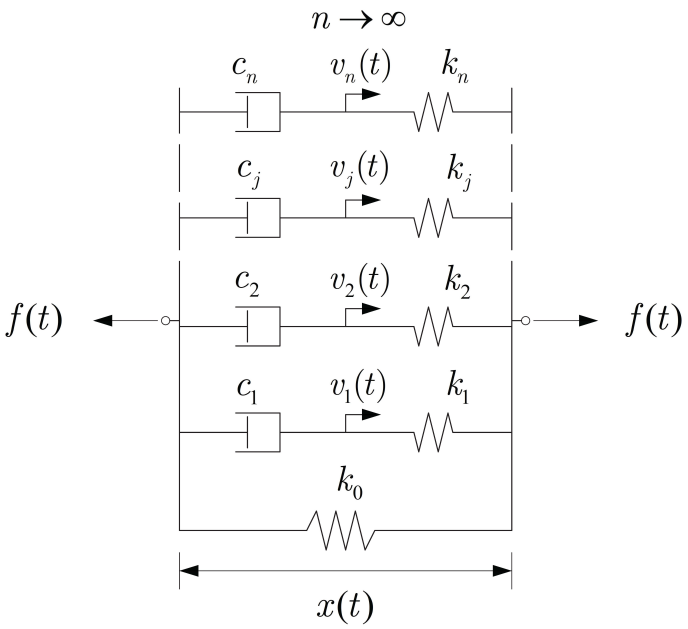

FIGURE 1.4: A physical representation of the Biot model

Hilbert transform to determine the RILD force, the whole deformation history from the past to the infinite future are required, and thus a residual deformation may lead to an infinitely large damping force, resulting in the failure of convergence. Makris [40] proposed a causal hysteretic model which yields exact rate-independent dissipation behavior and showed that this model is actually a high-frequency limiting case of the Biot model. Later, Makris and Zhang [41] claimed that the Biot model is the simplest, causal and physically realizable RILD model to approximate the nearly frequency-independent cyclic behavior of soil.

More recently, Spanos and Tsavachidis [42] developed two techniques for dynamic analyses of structure incorporated with the Biot model: a recursive one developed by applying the Prony method, and another aoto-regression-moving-average method developed by conducting nonlinear regression analyses. Muscolino et al. [43] applied the Laguerre polynomial approximation method to the prediction of the dynamic response of different RILD models under deterministic and random excitations. Nakamura [44, 45] suggested a method for transforming the complex stiffness with large hysteretic damping to the time domain by applying a linear regression technique and then proposed an approximated RILD model which satisfies the condition of causality. This model can be readily used and efficiently calculated in the time domain, but in the frequency domain, a closed-form analytical representation is not available, and numerical evaluation of the Hilbert transform is required instead to determine the dynamic stiffness at discrete frequency data points. Genta and Amati [33] proposed a method of tuned Maxwell-Wiechert (TMW) model with a finite number of Maxwell branches, so that it can approximate the loss modulus of the ideal RILD over a frequency range of interest. A similar concept was used by Makris and Zhang [41] with the Biot model as a reference model. Reggio et al. [46] proposed a methodology to identify modal and physical parameters of linear non-viscous damped MDF systems on the basis of

recorded time-histories of structural dynamic responses.

Ikago and Inoue [6] first pointed out the potential benefit of RILD in the seismic protection of low-frequency structures. Keivan et al. [47, 48] proposed semi-active methods to mimic the behavior of RILD by using a first-order all-pass filter, which is further passively realized by using a mechanical system consisting of a negative stiffness element and a Maxwell element connected with each other in parallel [49, 50]. Huang et al. [51] presented a damping algorithm which can realize frequency-insensitive energy dissipation over a frequency range of interest. Mastroddi et al. [52] extended the use of the Biot model to viscoelastic MDF systems for application to practical aerospace systems.

1.3 Structure of this dissertation

On the basis of the above background investigation, one can summarize that RILD has important applications in the following two aspects:

1) RILD is thought to provide a promising solution to simultaneously controlling both the response displacement and floor-response acceleration in a low-frequency structure subjected to strong ground motions.

2) RILD is expected to be a straightforward model of simulating the structural inherent damping without adopting the mathematically convenient assumption of Rayleigh damping, which has been doubted for a long time.

However, it is well known that an ideal RILD model is noncausal, which makes it impossible to be physically realized by using real-life devices, and also makes it challenging to be numerically analyzed in nonlinear simulation problems. *The purpose of this dissertation is to pursue causal models which can mimic the behavior of ideal RILD and facilitate their practical applications in the above two situations*.

Although some causal models have been proposed to approximate the behavior of RILD, and computationally efficient time-domain techniques are available for the dynamic response analysis of a structural model with RILD, the following issues yet remain to be considered and thus to be discussed in this dissertation:

1) *Lack of a simple and physically realizable model for utilizing the benefit of RILD in a base-isolated building structure subjected to strong ground motions*

   Motivation: The existing causal RILD models are thought to be relatively complex in the sense of their physical realization by using real-life devices for practical applications in low-frequency structures. For example, in order to physically realize the Biot model, an infinite number of Maxwell elements are required to be arranged in parallel [32]. Even though the number of Maxwell elements can be adequately reduced by using the TMW model, it may be no less than a certain number to control the approximation error below a threshold.

   Solution: In Chapter 2, following the illustration of the potential benefit of RILD for seismic protection of a low-frequency structure, a simple and physically realizable

model is to be proposed for utilizing this benefit. *This model requires only one Maxwell element connected in parallel with an ideal linear negative stiffness element (LNSE)* (referred to as Maxwell-negative-stiffness (MNS) model), which creates a physical implementation of the bilinear digital filter used by Keivan et al. [47] (hereafter referred to as Keivan model). For applications into a base-isolation system, one can readily connect an oil damper in series with a coil spring to realize the Maxwell element, and equivalently reduce the horizontal stiffnesses of isolators to create the ideal LNSE. Otherwise, a passive device which can create linear negative stiffness is to be designed for the same purpose. The effectiveness of the MNS model for seismic protection of a 5-story base-isolated benchmark building structure is also to be examined.

2) *Lack of a novel causal model to connect the existing models and enable the development of a unified framework of approximating the behavior of RILD*

Motivation: Although the mathematical relation between the Makris and Biot models has been established, more subtle connections between existing models remain to be unveiled for the development of a unified framework of causally approximated RILD models. For example, although both the Keivan and Biot models can be constructed by using Maxwell element(s), the potential relation between these two models is still poorly understood.

Solution: In Chapter 3, to achieve an improved approximation of the ideal RILD model in the sense of an extended frequency range, over which the rate-independent dissipation behavior may be mimicked, a novel fractional-order digital filter is generalized from the bilinear digital filter used by Keivan et al. [47]. The novel filter can be physically constructed by arranging a fractional Maxwell element [53, 54] and an LNSE coupled in parallel (hereafter referred to as fractional-Maxwell-negative-stiffness (FMNS) model). The subtle relations between the FMNS model with the existing causal models are to be discussed and mathematically proved. A *unified* framework of causally approximated RILD models is to be constructed. Furthermore, for the time-domain implementation of the FMNS model, a numerical analysis technique is to be developed by directly calculating the fractional derivative on the basis of so-called L1-algorithm [55], so that with little calculations associated with the coefficient estimation, it can be readily embedded into the established numerical integration schemes for nonlinear response history analyses of a structural model with RILD.

3) *Lack of a computationally efficient method of analyzing the fractional-order RILD model for simulating structural damping without adopting the assumption of Rayleigh damping*

Motivation: RILD is expected to be a straightforward model for simulating the structural inherent damping without adopting the mathematically convenient assumption of Rayleigh damping, but its noncausality hinders its application in a nonlinear simulation problem. Causal approximations of RILD may be used to overcome this shortcoming, but typically suffer heavy computational burden associated with their time-domain interpretations in terms of convolution integral. Some methods have been

suggested to accelerate the analysis of a structural model with RILD in the time domain, but still limited effort has been made to develop a computationally efficient method of analyzing the FMNS model, which is thought to be a unified causal RILD model.

Solution: In Chapter 4, a recursive method is to be developed by using a Prony series to approximate the Mittag-Leffler relaxation function, which is the damping kernel of the FMNS model. Both time- and frequency-domain methods are to be discussed for the parameter estimation of a Prony series. Compared with the L1-algorithm-based method developed in Chapter 3, the above recursive method can be more computationally efficient without significant loss of simulation accuracy. Comparison studies are to be made between the developed method with the existing methods, e.g., the Nakamura method [45], and a method of superposition of modal damping matrices [7] when they are separately applied to simulate the inherent damping of a ten-story benchmark building model with the nonlinearities of structural stiffness elements taken into account.

On the basis of the research work in the previous chapters, some conclusions are to be drawn, and more problems and further directions to be discussed in the future are to be pointed out in Chapter 5. The structure of this dissertation is summarized in Fig.1.5.

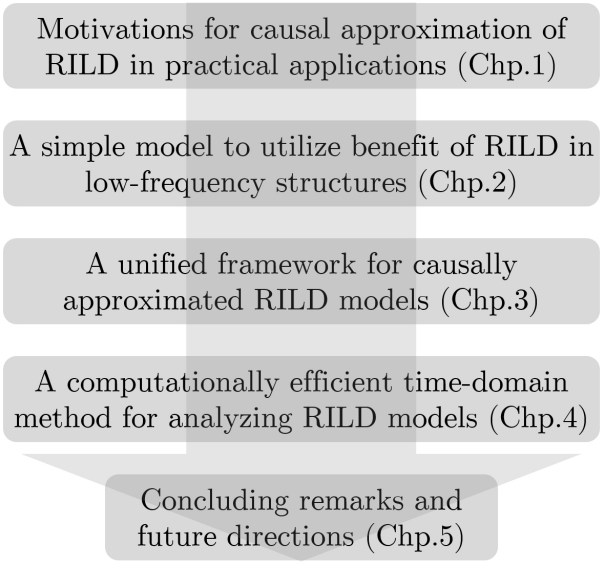

FIGURE 1.5: Structure of this dissertation

Chapter 2

A Simple Model to Utilize the Benefit of RILD in Low-frequency Structures

2.1 Introduction[‡]

It is well known that a rate-independent damping element improves the performance of a low-frequency structure by reducing the floor-response acceleration without increasing the displacement when subjected to strong ground motion. Indeed, Makris [56, 57] indicated that the presence of a friction-type damper in the isolation layer contributes to reducing the isolator displacement and the floor-response acceleration simultaneously when a seismic isolated structure is subjected to near-source ground motion containing a long-duration pulse. He et al. [58] proposed a semi-active friction damper to reduce both the peak drift and the peak acceleration of isolators by introducing a boundary layer around the switching of the controller. Inaudi [59] proposed a semi-active control law designated modulated homogeneous friction (MHF) in which the control force is operated such that it is proportional to the local peak deformation of the device. It can also be shown [59] that a linearized model of the MHF is rate-independent linear damping (RILD). For example, Fig. 2.1 compares the hysteresis loops of RILD and MHF, which are designed with the same amount of energy dissipated in a sinusoidal deformation cycle.

RILD represents the frequency-independent dissipation characteristics of structural elements (or materials). It is also referred to as structural damping, complex stiffness, linear hysteretic damping, or ideal hysteretic damping [25–27]. Ikago and Inoue [6] pointed out that RILD benefits low-frequency structures by generating a lower restoring force and acceleration response than other damping types with similar displacement reduction. However, owing to the non-causality of RILD [28], a linear elastic system equipped with RILD requires the entire time history of the input ground motion in the analysis, and is thus most conveniently calculated in the frequency domain [60].

Nevertheless, many attempts have been made to conduct time-domain analysis of RILD. Reid [26] proposed a time-domain representation for RILD to solve the free vibration of a single-degree-of-freedom (SDF) system. This model was later found to be nonlinear [61] and impractical, because of the difficulty in the frequency-domain analysis of non-linear models. The first successful viscoelastic model for RILD was presented by Biot [31]. In

[‡]Part of this chapter is reported in the publication (H. Luo et al., 2019)

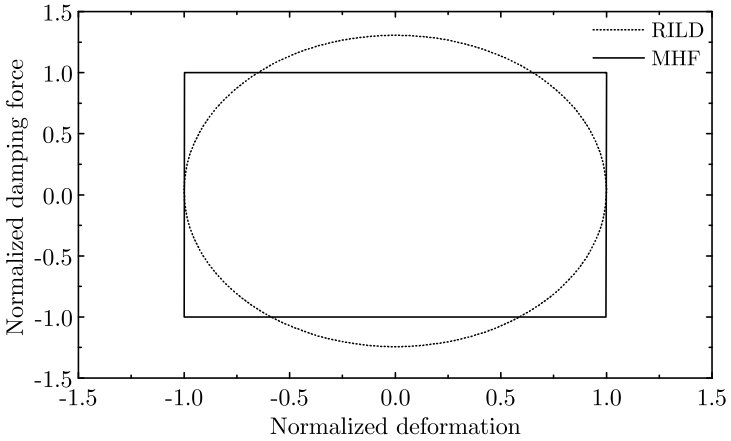

FIGURE 2.1: Hysteresis loops of RILD and MHF subjected to sinusoidal deformation

Biot's model, an infinite number of Maxwell elements are arranged in parallel with a linear spring. Time-domain analysis methods to solve the Biot model were pursued by Spanos and Tsavachidis [42] and Muscolino et al. [43].

Crandall [62] investigated the impulse responses of an ideal viscous damper, an ideal hysteretic damper (RILD), and a band-limited hysteretic damper, and concluded that a damper with frequency independent energy dissipation responds prior to the application of the impulsive excitation, violating causality requirements. Inaudi and Kelly [63] proposed a time-domain analysis method based on convergent calculations using the Hilbert transform in a repetitive manner. Inaudi and Makris [39] proposed a less computationally demanding time-domain analysis method using complex-valued signals. Makris [40] proposed adding an adjustable real term based on the Kramers–Kronig relations to the complex-value stiffness of an ideal RILD model to satisfy the causality requirements. The model was shown to be the high-frequency limiting case of the linear viscoelastic model proposed by Biot [31]. *However, these causal representations of RILD are considered to be relatively complex for practical applications. One of the major contributions in this work is the derivation of a simpler approximation of RILD and its realization through the active control method and as a passive mechanical model.*

The remainder of this chapter is organized as follows. In Section 2.2, the governing equation for a structure incorporated with RILD is given, followed by a description of the advantages of RILD over linear viscous damping (LVD) in low-frequency structures. To further illustrate the benefits of RILD in reducing floor-response acceleration without increasing the displacements, Section 2.3 presents a model of a five-story structure employed for comparison between different energy-dissipating devices by conducting incremental dynamic analysis and parametric studies. Furthermore, both active and passive models are proposed to approximate RILD for practical applications in Section 2.4. Finally, some conclusions are presented.

2.2 Equation of motion

First, one considers a single-degree-of-freedom (SDF) shear building structure containing an LVD element subjected to harmonic ground excitation $\ddot{x}_g(t) = Ae^{i\omega t}$, where i, ω, and A are the imaginary unit, excitation circular frequency, and ground acceleration amplitude, respectively. The equation of motion for the SDF model whose mass, stiffness, and damping coefficient are m, k, and c, respectively, is

$$m \cdot {}_1\ddot{x}(t) + c \cdot {}_1\dot{x}(t) + k \cdot {}_1x(t) = -m\ddot{x}_g(t) \tag{2.1}$$

where ${}_1x(t)$ is the response displacement of the mass relative to the ground, and the left subscript " 1 " indicates the response of the LVD system. The fundamental natural circular frequency and damping ratio for this system are $\omega_0 = \sqrt{k/m}$ and $h = c/(2m\omega_0)$, respectively. Substituting ${}_1x(t) = {}_1Xe^{i\omega t}$ into Eq. (2.1) yields

$$(-\omega^2 + 2hi\omega\omega_0 + \omega_0^2) \cdot {}_1Xe^{i\omega t} = -Ae^{i\omega t} \tag{2.2}$$

Second, the equation of motion for an SDF structure equipped with a RILD element having a loss factor 2β is considered as follows,

$$(-\omega^2 + 2\beta i\omega_0^2 \mathrm{sgn}(\omega) + \omega_0^2) \cdot {}_2Xe^{i\omega t} = -Ae^{i\omega t} \tag{2.3}$$

where the left subscript " 2 " indicates the response of the RILD system and $\mathrm{sgn}(\omega)$ is the signum function, i.e. $\mathrm{sgn}(\omega) = 1$ if $\omega > 0$; $\mathrm{sgn}(\omega) = 0$ if $\omega = 0$; otherwise, $\mathrm{sgn}(\omega) = -1$.

Let the damping forces of LVD and RILD in the frequency domain be ${}_1F_f(i\omega)$ and ${}_2F_f(i\omega)$, respectively.

$${}_1F_f(i\omega) = 2ih\frac{\omega}{\omega_0}k \cdot {}_1X \tag{2.4}$$

$${}_2F_f(i\omega) = 2i\beta k\mathrm{sgn}(\omega) \cdot {}_2X \tag{2.5}$$

Provided that $\beta = h$, and the difference between ${}_1X$ and ${}_2X$ is negligibly small and thereby ${}_1X = {}_2X = X$, then the following relationship between the damping forces of LVD and RILD holds:

$$H_T(i\omega) = \frac{{}_2F_f(i\omega)}{{}_1F_f(i\omega)} = \frac{\omega_0}{|\omega|} \tag{2.6}$$

which suggests that under the above mentioned assumption, the damping force of RILD is lower than that of LVD when the excitation frequency is higher than the fundamental natural frequency of the structural system.

2.2.1 Transfer functions of LVD and RILD systems

Solving Eqs.(2.2) and (2.3) with respect to the displacement amplification factor X/A yields the transfer functions for the linear viscous damped system ${}_1H(i\omega)$ and the rate-independent

linear damped system ${}_2H(i\omega)$, respectively:

$$ {}_1H(i\omega) = -\frac{1}{-\omega^2 + 2hi\omega\omega_0 + \omega_0^2} \tag{2.7} $$

$$ {}_2H(i\omega) = -\frac{1}{-\omega^2 + \{1 + 2\beta i\mathrm{sgn}(\omega)\}\omega_0^2} \tag{2.8} $$

The absolute acceleration transfer functions for the linear viscous damped system ${}_1H_a(i\omega)$ and the rate-independent linear damped system ${}_2H_a(i\omega)$ can be obtained, respectively:

$$ {}_1H_a(i\omega) = \frac{2hi\omega\omega_0 + \omega_0^2}{-\omega^2 + 2hi\omega\omega_0 + \omega_0^2} \tag{2.9} $$

$$ {}_2H_a(i\omega) = \frac{\{1 + 2\beta i\mathrm{sgn}(\omega)\}\omega_0^2}{-\omega^2 + \{1 + 2\beta i\mathrm{sgn}(\omega)\}\omega_0^2} \tag{2.10} $$

For the damping forces, the following quantities are defined as damping force coefficient transfer functions:

$$ {}_1H_f(i\omega) = -\frac{2hi\omega\omega_0}{(-\omega^2 + 2hi\omega\omega_0 + \omega_0^2)g} \tag{2.11} $$

$$ {}_2H_f(i\omega) = -\frac{2\beta i\omega_0^2\mathrm{sgn}(\omega)}{\left[-\omega^2 + \{1 + 2\beta i\mathrm{sgn}(\omega)\}\omega_0^2\right] g} \tag{2.12} $$

where g is the acceleration due to gravity.

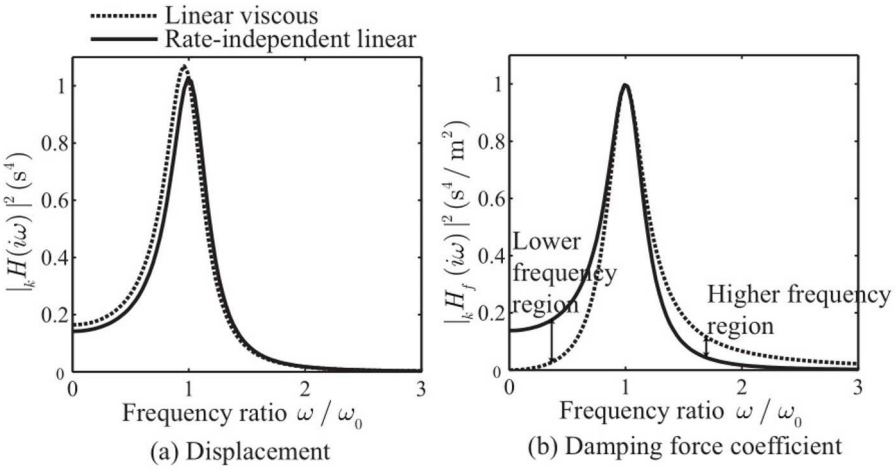

FIGURE 2.2: Squared resonance curves

As shown in Fig. 2.2, the squared displacement transfer functions for the two systems are similar at any frequency, whereas those for the damping forces are substantially different. In the frequency region higher than the fundamental natural frequency, the control force of the LVD is higher than that of RILD, while the opposite holds true in the frequency region lower than the fundamental natural frequency. This suggests that LVD in a low-frequency structure subjected to high-frequency ground motion may generate higher damping forces compared to RILD, which can result in higher floor-response accelerations.

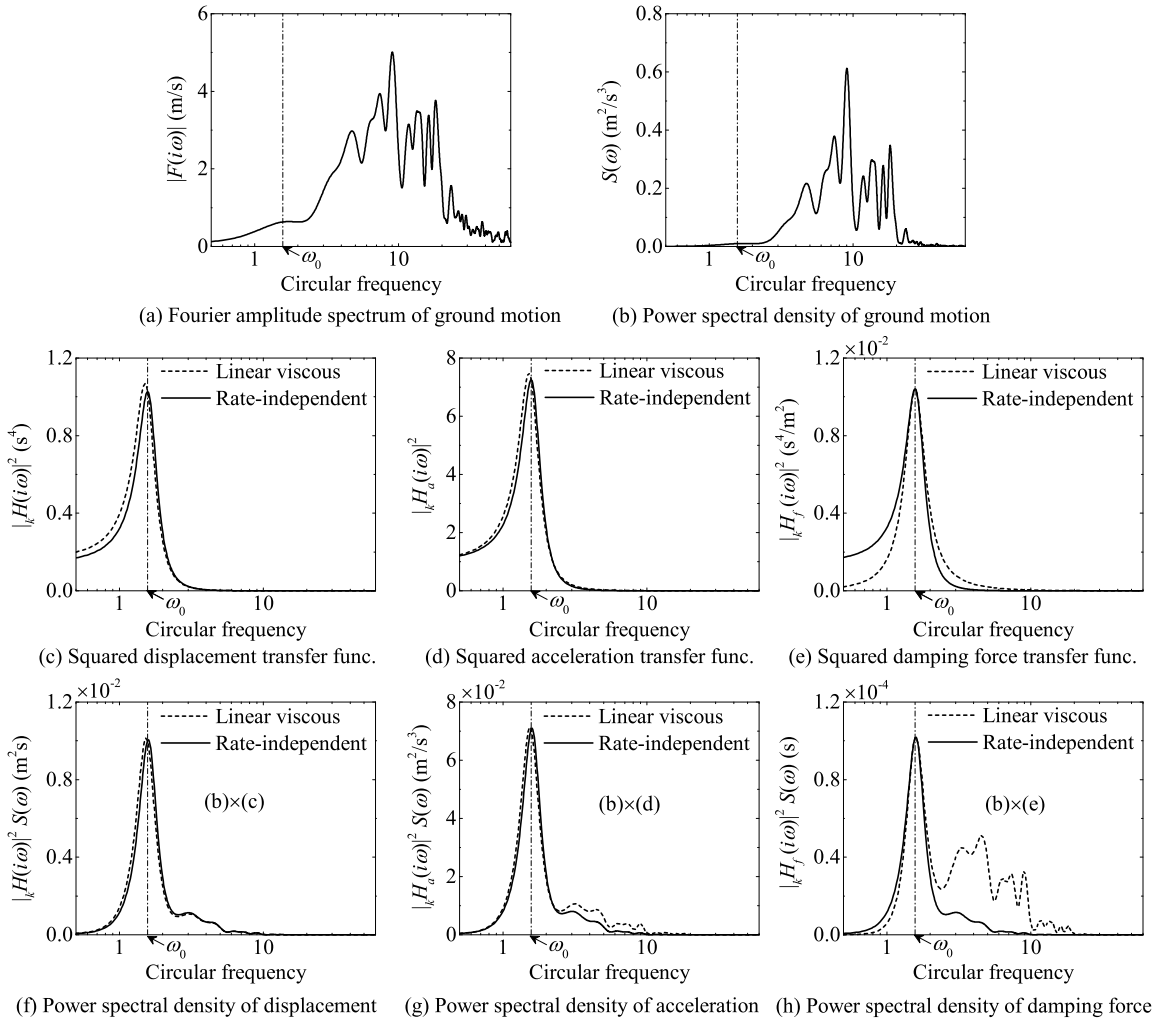

FIGURE 2.3: Power spectral density (JMA Kobe 1995 N–S)

For example, let the SDF structure be a long-period base-isolated structure with a fundamental natural period of 4 second and containing two different types of damping elements with the same damping ratio of 0.2: ${}_1\xi = h = 0.2$ and ${}_2\xi = \beta = 0.2$. Fig. 2.3 shows the analytical results of the two differently-damped structures. The north–south component of the ground motion recorded by the Japan Meteorological Agency (JMA) during the 1995 Kobe Earthquake was employed. Figs. 2.3(a) and 2.3(b) show the Fourier amplitude spectrum and power spectral density of the ground motion, respectively. Because the displacement transfer functions are equally similar for the two differently-damped structures (Fig. 2.3(c)), the displacement power spectral densities are similar (Fig. 2.3(f)). Although the absolute acceleration transfer functions of the two differently-damped systems are also similar (Fig. 2.3(d)), the differences between their power spectral densities for absolute accelerations (Fig. 2.3(g)) in the frequency region higher than the fundamental natural frequency become noticeable when excited by high-frequency components in the ground motion. In addition, the damping forces show substantial differences (Figs. 2.3(e) and (h)). In frequency regions higher than the fundamental natural frequency, the power spectral density of the

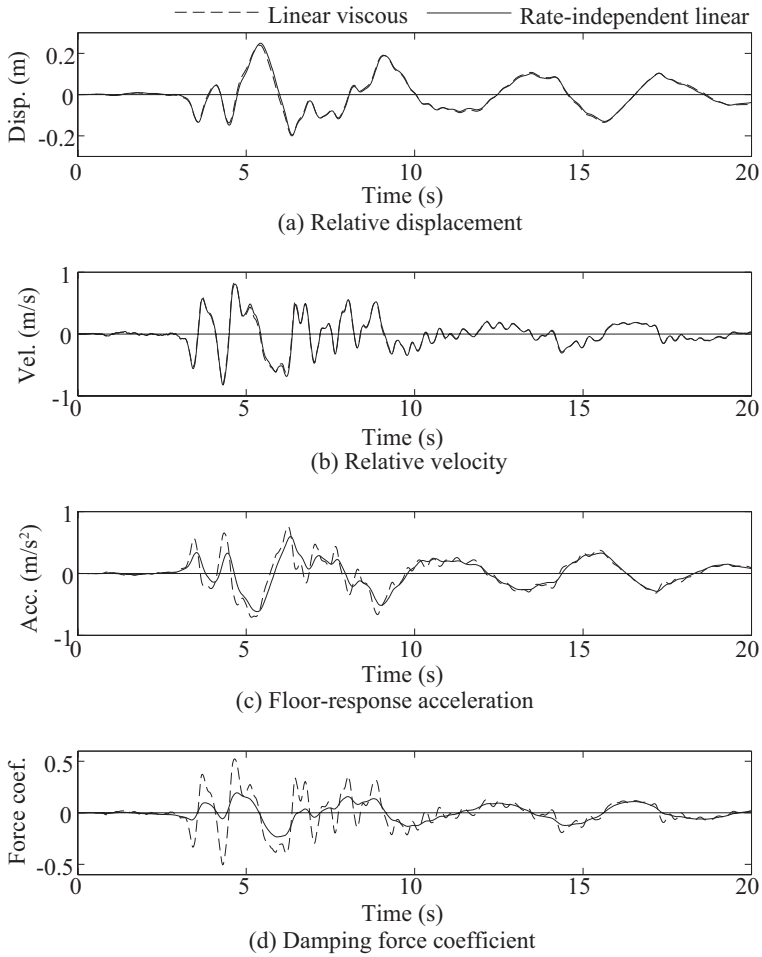

FIGURE 2.4: Responses of linear viscous damped and rate-independent linear damped systems(JMA Kobe 1995 N–S)

damping force for the LVD system contains higher frequency components (dashed line) than those of the RILD system (solid line).

Furthermore, Fig. 2.4 compares the time histories of the two differently-damped structures. It should be pointed out that due to the non-causality of the RILD model in the time domain, in this study, the time history analyses of structure incorporated with RILD are conducted in the frequency-domain with the entire time history of input ground motion provided. The two exhibit almost identical displacement and velocity time histories, whereas the maximum damping force yielded by RILD is roughly half that of LVD. In addition, there is a small reduction in the acceleration response for the system with RILD. Although one cannot fully explore the effect of higher modal responses in acceleration using an SDF system, the lower damping forces of RILD are expected to result in lower floor-response accelerations than those yielded by LVD. The effect of higher modes in a multi-degree-of-freedom system (MDF) is discussed in Section 2.3.

2.2.2 Fundamental circular frequency and response central circular frequency

Assume that the ground motion $x_g(t)$ is a stationary random process with a zero mean value and a one-sided power spectral density $S(\omega)$, the response ${}_kx(t)$ can also be assumed to be a stationary random process with power spectral densities described by the following equation:

$$ {}_kG(\omega) = |{}_kH(i\omega)|^2 S(\omega) \quad (k = 1, 2) \tag{2.13} $$

where $k = 1$ and $k = 2$ indicate LVD and RILD, respectively.

Here, the n-th spectral moments ${}_k\lambda_n$ and central frequencies ${}_k\omega_n$ are defined as follows:

$$ {}_k\lambda_n = \int_0^\infty \omega^n \cdot {}_kG(\omega) d\omega \quad (k = 1, 2;\ n = 0, 1, 2) \tag{2.14} $$

$$ {}_k\omega_n = \left(\frac{{}_k\lambda_n}{{}_k\lambda_0} \right)^{\frac{1}{n}} \quad (k = 1, 2;\ n = 1, 2) \tag{2.15} $$

According to Parseval's theorem, ${}_k\lambda_0$ and ${}_k\lambda_2$ are identical to the mean square values of the response displacements and velocities, respectively:

$$ {}_k\sigma_x^2 = \frac{1}{T} \int_0^T {}_kx(t)^2 dt = {}_k\lambda_0 \tag{2.16} $$

$$ {}_k\sigma_{\dot{x}}^2 = \frac{1}{T} \int_0^T {}_k\dot{x}(t)^2 dt = {}_k\lambda_2 \tag{2.17} $$

where ${}_1x(t)$ and ${}_2x(t)$ are the relative displacements of the LVD and RILD systems, respectively. Let ${}_k\omega_1$ denote the first central frequency of ${}_kG(\omega)$. Then, one has

$$ \int_0^\infty (\omega - {}_k\omega_1) \cdot {}_kG(\omega) d\omega = 0 \tag{2.18} $$

The second central moments ${}_kI$ are

$$ {}_kI = \int_0^\infty (\omega - {}_k\omega_1)^2 \cdot {}_kG(\omega) d\omega \tag{2.19} $$

Thus, the second spectral moments with respect to the frequency origin are

$$ \int_0^\infty \omega^2 \cdot {}_kG(\omega) d\omega = {}_k\omega_1^2 \cdot {}_k\lambda_0 + {}_kI \tag{2.20} $$

Because ${}_kG(\omega)$ are narrow-band processes, one can assume that the second central moments ${}_kI$ on the right-hand side of Eq. (2.20) are relatively small compared to those of the first term. Thus, one can substitute ${}_k\omega_2$ for the central frequency ${}_k\omega_1$ [64], neglecting the second term on the right-hand side of Eq. (2.20) to obtain

$$ {}_k\omega_2^2 = {}_k\omega_1^2 + \frac{{}_kI}{{}_k\lambda_0} \approx {}_k\omega_1^2 \tag{2.21} $$

If the ground excitation is the white noise with a constant power spectrum density $S(\omega) \equiv S_0$, then

$$ {}_1\sigma_x^2 = \frac{S_0}{4h\omega_0^3} \tag{2.22} $$

$$ {}_1\sigma_{\dot{x}}^2 = \frac{S_0}{4h\omega_0} \tag{2.23} $$

$$ {}_1\sigma_{\ddot{x}+\ddot{x}_g}^2 = \frac{S_0\omega_0(1+4h^2)}{4h} \tag{2.24} $$

$$ {}_2\sigma_x^2 = \sqrt{\frac{1+\sqrt{1+4\beta^2}}{2(1+4\beta^2)}}\frac{S_0}{4\beta\omega_0^3} \tag{2.25} $$

$$ {}_2\sigma_{\dot{x}}^2 = \sqrt{\frac{1+\sqrt{1+4\beta^2}}{2}}\frac{S_0}{4\beta\omega_0} \tag{2.26} $$

$$ {}_2\sigma_{\ddot{x}+\ddot{x}_g}^2 = \sqrt{\frac{(1+\sqrt{1+4\beta^2})(1+4\beta^2)}{2}}\frac{S_0\omega_0}{4\beta} \tag{2.27} $$

Provided that $h = \beta$, the following equations hold

$$ {}_k\sigma_{\ddot{x}+\ddot{x}_g} = \omega_0^2\sqrt{(1+4h^2)}\cdot {}_k\sigma_x \tag{2.28} $$

$$ \frac{{}_2\sigma_{\ddot{x}+\ddot{x}_g}}{{}_1\sigma_{\ddot{x}+\ddot{x}_g}} = \frac{{}_2\sigma_x}{{}_1\sigma_x} = \sqrt[4]{\frac{1+\sqrt{1+4h^2}}{2(1+4h^2)}} \tag{2.29} $$

It should also be noted that for $h > 0$,

$$ \sqrt[4]{\frac{1+\sqrt{1+4h^2}}{2(1+4h^2)}} < 1 \tag{2.30} $$

Therefore, one can conclude that with equal damping ratios $h = \beta > 0$, the displacement variance ${}_2\sigma_x^2$ and absolute acceleration variance ${}_2\sigma_{\ddot{x}+\ddot{x}_g}^2$ of the RILD system are lower than those of the LVD system, ${}_1\sigma_x^2$ and ${}_1\sigma_{\ddot{x}+\ddot{x}_g}^2$, respectively, when excited by the white noise with a constant power spectrum density.

Alternatively, when h and β are relatively small (< 0.05), the following approximations hold

$$ {}_k\sigma_{\ddot{x}+\ddot{x}_g} \approx \omega_0 \cdot {}_k\sigma_{\dot{x}} \approx \omega_0^2 \cdot {}_k\sigma_x \tag{2.31} $$

Let ${}_kS_D(\omega_0)$, ${}_kS_V(\omega_0)$, and ${}_{k,p}S_V(\omega_0)$ denote the maximum displacement spectra, maximum velocity spectra, and pseudo-velocity spectra, respectively:

$$ {}_kS_D(\omega_0) = \max_t\{|{}_kx(t)|\} \tag{2.32} $$

$$ {}_kS_V(\omega_0) = \max_t\{|{}_k\dot{x}(t)|\} \tag{2.33} $$

$$ {}_{k,p}S_V(\omega_0) = \omega_0 \cdot {}_kS_D(\omega_0) \tag{2.34} $$

If the fundamental circular frequency ω_0 is close to the dominant circular frequency of the ground motion and thus to the central frequency, the following relationship holds:

$$ {}_kS_V(\omega_0) \approx {}_{k,p}S_V(\omega_0) = \omega_0 \cdot {}_kS_D(\omega_0) \tag{2.35} $$

Eqs.(2.31) and (2.35) are especially useful for practicing structural engineers designing rate-dependent devices when they are exclusively provided with maximum displacement spectra. However, these hold in limited cases. Indeed, Pekcan, Mander, and Chen [65] pointed out that the pseudo-velocity spectrum underestimates the force generated by a rate-dependent device and proposed an alternative simple estimation procedure that incorporates equivalent linear damping based on actual velocities.

The root mean square (RMS) values of the damping force coefficients ${}_k\sigma_F$ defined as the ratios of the damping forces to the total weight of the structure mg are

$$ {}_1\sigma_F = \frac{2h\omega_0 \cdot {}_1\omega_2 \cdot {}_1\sigma_x}{g} \tag{2.36} $$

$$ {}_2\sigma_F = \frac{2\beta\omega_0^2 \cdot {}_2\sigma_x}{g} \tag{2.37} $$

Provided that $h = \beta$ and ${}_1\sigma_x \approx {}_2\sigma_x$,

$$ \frac{{}_1\sigma_F}{{}_2\sigma_F} \approx \frac{{}_1\omega_2}{\omega_0} \tag{2.38} $$

Similarly, the coefficients of the maximum damping forces ${}_kC_f$ defined as the ratios of the damping forces to the total weight of the structure are

$$ {}_1C_f = \frac{2h\omega_0 \cdot {}_kS_V(\omega_0)}{g} \tag{2.39} $$

$$ {}_2C_f = \frac{2\beta\omega_0 \cdot {}_{k,p}S_V(\omega_0)}{g} \tag{2.40} $$

Provided that $h = \beta$,

$$ \frac{{}_1C_f}{{}_2C_f} = \frac{{}_kS_V(\omega_0)}{{}_{k,p}S_V(\omega_0)} \tag{2.41} $$

Eqs. (2.38) and (2.41) explain the difference between the damping forces in the two differently-damped systems. Table 2.1 lists the ratios of RMS damping forces and maximum damping forces for the example structures subjected to the Kobe record; these demonstrate that the maximum rate-independent linear damping force is approximately half the value of the maximum linear viscous damping force.

TABLE 2.1: RMS and maximum damping force coefficients

${}_1\sigma_F$:	0.106	${}_1\omega_2$:	2.881	${}_1C_f$:	0.524
${}_2\sigma_F$:	0.058	${}_2\omega_2$:	1.571	${}_2C_f$:	0.234
${}_1\sigma_F/{}_2\sigma_F$:	1.82	${}_1\omega_2/{}_2\omega_2$:	1.83	${}_1C_f/{}_2C_f$:	2.24

2.3 Comparisons with other energy-dissipating devices

To further illustrate the benefit of RILD in reducing floor-response accelerations without increasing displacements, a base-isolated five-story shear building was employed as an analytical example. Fig. 2.5 depicts this analytical model while Table 3.4 lists its properties. The total horizontal stiffness of the isolators is designed such that the fundamental undamped natural period of the structure is 4.0 s. The inherent damping of the superstructure with its base fixed is 2% of the critical damping value for the first mode, and the inherent damping at the isolation level was ignored.

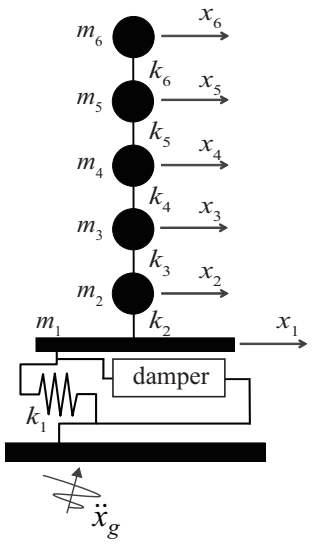

FIGURE 2.5: Benchmark structure

TABLE 2.2: Properties of the analytical model

Floor	Mass (t)	Stiffness (kN/m)	Damping coefficient (kN·s/m)
R	1 739	—	—
5	1 800	2 291 000	9 770
4	1 807	2 488 000	10 610
3	1 928	1 939 000	8 270
2	2 335	2 038 000	8 690
1	3 057	1 760 000	7 510
Isolation level	—	31 250	—

For comparison, four types of damping devices were incorporated into the isolation level: LVD, RILD, nonlinear viscous damping, and hysteretic damping. Each damping device is identified by a number, as denoted in Table 2.3.

Fig. 2.6 shows the characteristics of the nonlinear viscous and hysteretic dampers, where C_1 and C_2 respectively denote the initial damping coefficient and the slope of the damping

TABLE 2.3: Damper properties

Number	Type	Property
1	Linear viscous	$h = 0.25$
2	Rate-independent linear	$\beta = 0.28$
3	Nonlinear viscous	$C_1 = 12,590$ kN·s/m, $C_2 = 853.1$ kN·s/m
4	Hysteretic	$\alpha = 0.028$

force with respect to the velocity after the relief valve of the fluid damper is activated, and α is the yield load coefficient of the hysteretic damper.

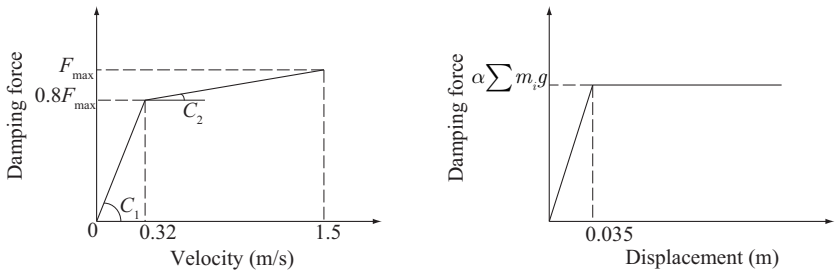

(a) Nonlinear viscous damper (b) Hysteretic damper

FIGURE 2.6: Properties of nonlinear dampers

Three types of recorded ground motion and three types of synthetic ground motion were employed as design earthquakes, in accordance with the practice in Japan. The three recorded ground motions were scaled such that their peak ground velocities (PGVs) were 0.5 m/s. Table 2.4 lists the details of the ground motion.

The spectral accelerations of the synthetic ground motions were compatible with the target spectrum, as shown in Fig. 2.7(b). The amplification properties of a typical surface subsoil were considered to determine the target spectrum in accordance with building design codes in Japan. The phase properties of the ground motion listed in Table 2.5 were used to synthesize the ground motion. Each ground motion is identified by a number, as shown in Tables 3 and 4. It should be mentioned that the time history analyses of the MDF structure with RILD were also conducted in the frequency-domain with the entire time history of input ground motion provided.

TABLE 2.4: Recorded ground motions

Number	Earthquake	Station	Component	PGV (m/s)
1	Imperial Valley, USA, 1940	El Centro	N–S	0.5
2	Kern County, USA, 1952	Taft	E–W	0.5
3	Tokachi-oki, Japan, 1968	Hachinohe Harbor	N–S	0.5

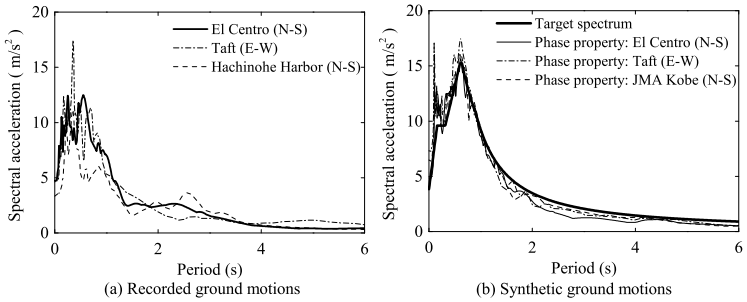

FIGURE 2.7: Target spectral acceleration

TABLE 2.5: Ground motions used to determine the phase properties

Number	Earthquake	Station	Component
4	Imperial Valley, USA, 1940	El Centro	N–S
5	Kern County, USA, 1952	Taft	E–W
6	Kobe, Japan, 1995	JMA Kobe	N–S

Let ${}_kx_j^s(t)$ denote the relative displacement at time t of the jth floor of the model containing the damping device k subjected to ground motion labeled by s. The four types of damping devices were designed such that the maximum isolator displacements $\max_{s,t}\{{}_kx_1^s(t); s = 1, 2, \ldots, 5, 6,\ 0 \leq t \leq T\}$, were 0.3 m. Table 2.3 lists the properties of the dampers that achieve this performance. For example, Figs. 2.8 and 2.9 show the time history seismic responses of the four differently-damped systems under synthetic ground motion with the Kobe record phase ($s = 6$). Fig. 2.10 shows the corresponding hysteresis loops for different dampers. In Figs. 2.8 and 2.9, it should be mentioned that although the nonlinear viscous and hysteretic damping systems generate relatively lower damping forces than that generated by linear viscous damping system, they generate larger maximum floor-response accelerations. This is partly because under the excitation of ground motion, the two nonlinearly damped systems experience phase transitions due to changes in the damping or stiffness parameters in the nonlinear damping devices. During transition from one phase to another, internal force redistributions may occur, along with an increase in the floor-response accelerations in the two systems. This can obviously be observed from the time history responses of the hysteretic damping system in Figs. 2.9(b) and (c). Fig. 2.11 shows the maximum seismic responses of the four differently-damped systems under each ground motion.

Furthermore, to understand the benefits of RILD incorporated into long-period structures, a number of incremental dynamic analyses (IDA) were performed. The six types of ground motion mentioned above were used as input ground motion in conducting the IDA, where the scale factor (SF) was varied from 0.5 to 1.5 at the interval of 0.05. All types of ground motion employed here were scaled such that their PGVs were 0.5 m/s when the scale factor $SF = 1.0$. In the design practice used in Japan, scale factors of $SF = 0.5$ and

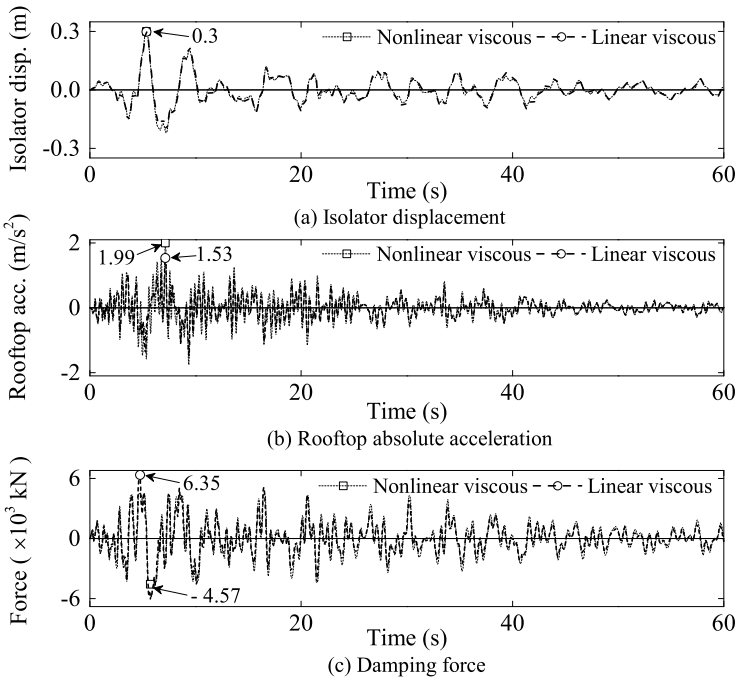

FIGURE 2.8: Time history responses of the nonlinear and linear viscous damping systems (synthetic ground motion(phase property: JMA Kobe 1995 NS))

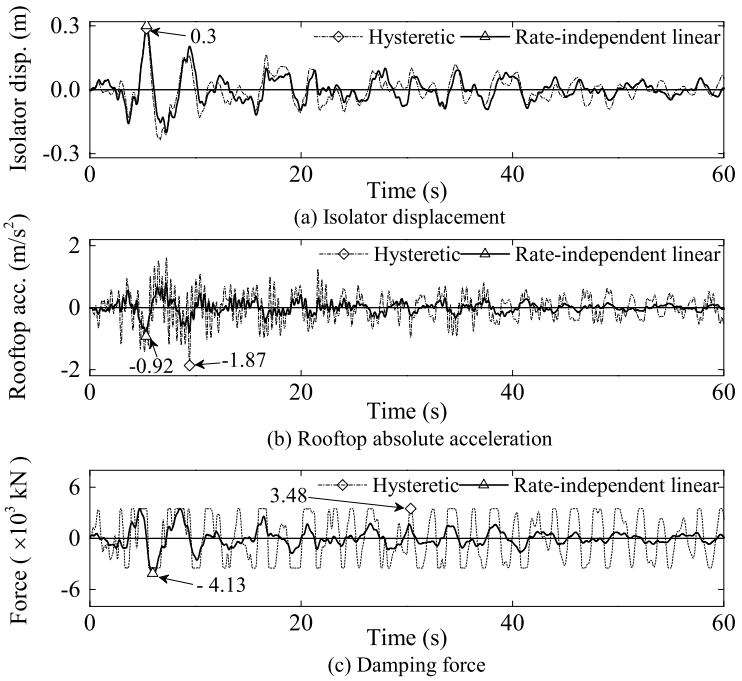

FIGURE 2.9: Time history responses of the hysteretic damping and RILD systems (synthetic ground motion(phase property: JMA Kobe 1995 NS))

$SF = 1.0$ correspond to design level and maximum considerable level earthquakes, respectively. If the performance of the structures against an excessive level earthquake beyond the maximum considerable level is to be examined, a scale factor of $SF = 1.5$ is commonly

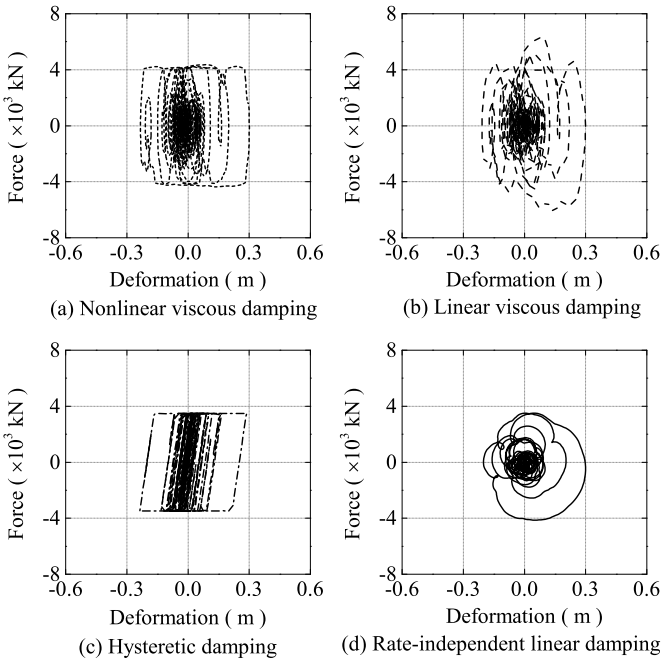

FIGURE 2.10: Hysteresis loops (synthetic ground motion(phase property: JMA Kobe 1995 NS))

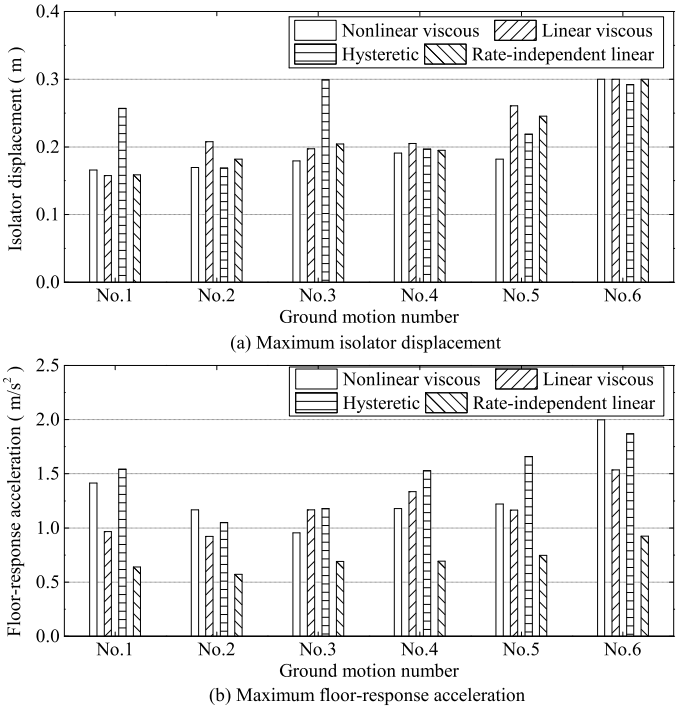

FIGURE 2.11: Maximum responses under each ground motion

used in Japanese practice. Fig. 2.12 plots the maximum floor-response accelerations for the differently-damped structures $\max_{j,t,s}\{{}_k\ddot{x}_j^s(t); j = 1,2,\ldots,5,\mathrm{R},\ s = 1,2,\ldots,6,\ 0 \le t \le T\}$ against the maximum isolator displacements $\max_{t,s}\{{}_kx_1^s(t); s = 1,2,\ldots,6,\ 0 \le t \le T\}$.

Among all of the scale factors, RILD showed the best performance. Nonlinearly damped systems ($k = 3, 4$) suffer large displacements as the scale factor increases, because the equivalent damping decreases as the response displacements increased in nonlinear damping devices.

Fig. 2.13 plots the maximum floor-response accelerations $\max_{s,j,t}\{{}_k\ddot{x}_j^s(t); s = 1, 2, \ldots, 6,\ j = 1, 2, \ldots, 5, \mathrm{R},\ 0 \le t \le T\}$ against the maximum isolator displacements $\max_{s,t}\{{}_kx_1^s(t); s = 1, 2, \ldots, 6,\ 0 \le t \le T\}$, where the damper parameter varies and the scale factor is fixed to $SF = 1$. In the case of nonlinear viscous damping device, the damping parameters C_1 and C_2 vary proportionally to each other. Fig. 2.13 shows the influence of damper parameter selections on the tradeoff between the isolator displacement and maximum floor-response acceleration (e.g., as achieved by varying an individual damper or a number of dampers). The figure reveals that there is an optimum damper parameter to minimize the maximum floor-response acceleration for each damping device. Adding more than the optimum damper parameter reduces the isolator displacements at the expense of increased floor-response accelerations. The reduction in floor-response acceleration of the structure with RILD becomes greater than that obtained from other damping devices as the damper parameters increase.

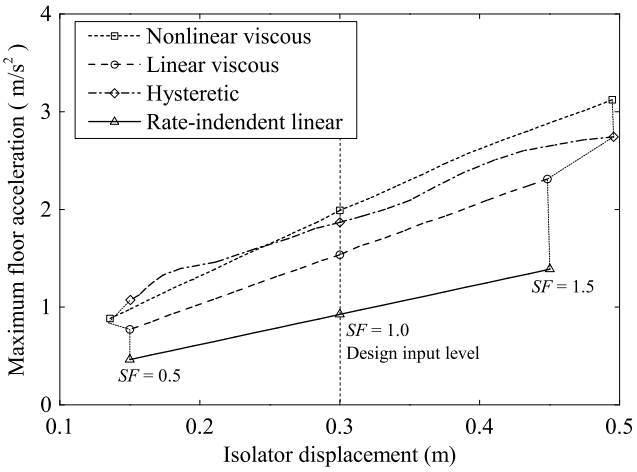

FIGURE 2.12: Incremental dynamic analysis

2.4 Proposed models of rate-independent linear damping

Although causal representations of RILD have been proposed by many researchers, they are considered to be relatively complex for practical applications. This section pursues a simpler and therefore more practical representations of RILD as active control and passive models.

2.4.1 Active control system

Here, we derive a first-order causal digital filter to determine the control force for a diagram of active control system [66–69]. Fig. 2.14 shows an active controlled base-isolated system. Multiplying the damping force of LVD ${}_1F_f(i\omega)$ by the target filter, as in Eq. (2.6), yields the

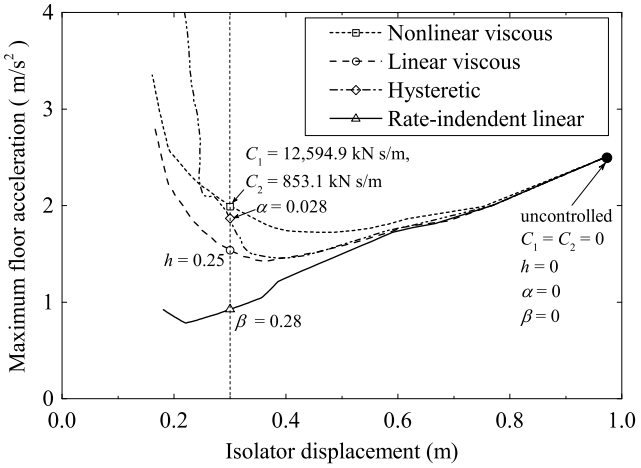

FIGURE 2.13: Performance curves

ideal desired control force to achieve rate-independent linear damping for the control device $F_c(i\omega)$:

$$F_c(i\omega) = {}_2F_f(i\omega) = H_T(i\omega) \cdot {}_1F_f(i\omega) \tag{2.42}$$

First-order Butterworth filter

Because the ideal target filter $H_T(i\omega)$ cannot be implemented owing to its noncausality, we employ a first-order Butterworth filter to approximate it, inspired by the insight that the amplitude of the Butterworth filter approaches the target amplitude as the excitation frequency increases in the frequency region beyond the cut-off frequency. A first-order Butterworth filter with a cutoff circular frequency of ω_0 is expressed as follows:

$$H_B(i\omega) = \frac{1}{1 + \dfrac{i\omega}{\omega_0}} \tag{2.43}$$

Fig. 2.15(b) depicts the Bode plot of the target filter and the Butterworth filter with a cut-off frequency of 0.25 Hz. As shown in Fig. 2.15(b), the phase lags throughout the entire frequency region. In particular, the phase delay at the cut-off frequency is 45 degrees ($\pi/4$ rad).

Phase compensating filter

Because the ideal control force should be in phase with the velocity, we can predict the unknown future velocity $\bar{t}$ seconds after the current time t_0 using an undamped SDF system with a fundamental circular frequency of ω_0.

If we assume that the future ground motion after time t_0 is a stationary random process with a zero mean, as we did in Section 2.2.2, the ensemble mean of the future unknown

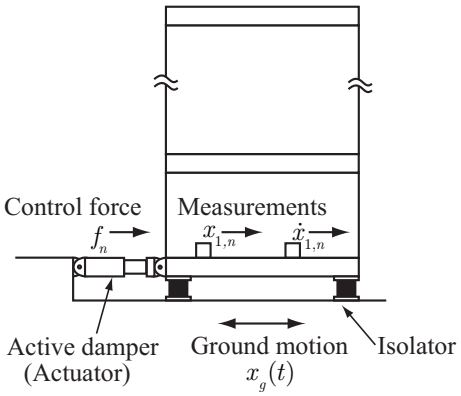

FIGURE 2.14: Diagram of active controlled base-isolation system

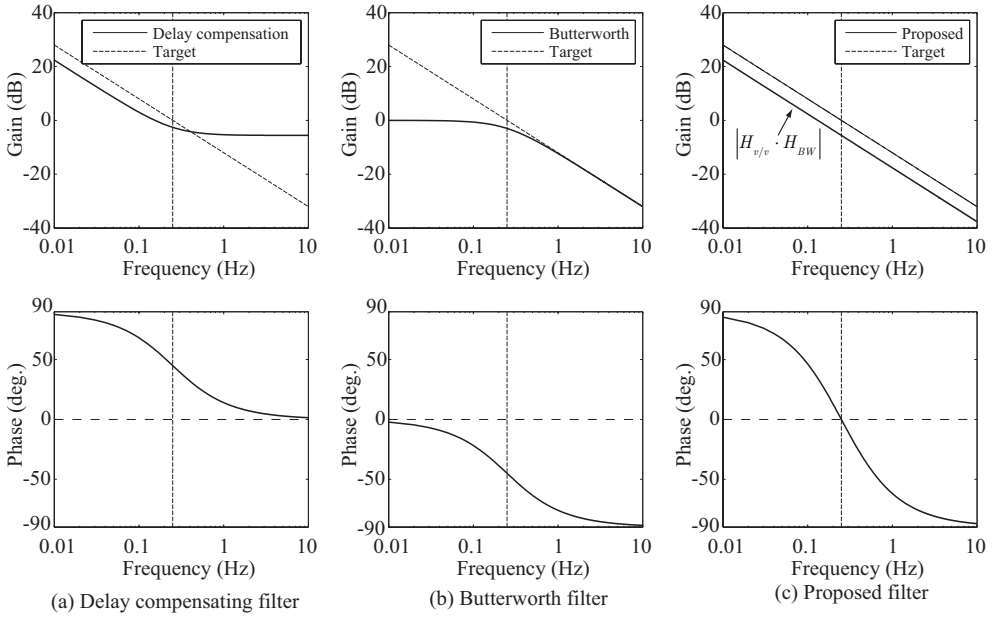

FIGURE 2.15: Bode plot of the proposed filter

ground excitation is

$$E[\ddot{x}_g(t)] = 0 \quad (t_0 < t) \tag{2.44}$$

The expected velocity at time $t = t_0 + \bar{t}$ is obtained as follows:

$$\begin{aligned} E[\dot{x}(t)] &= -\int_0^{t_0} \ddot{x}_g(\tau)\cos\omega_0(t-\tau)d\tau + E\left[-\int_{t_0}^{t} \ddot{x}_g(\tau)\cos\omega_0(t-\tau)d\tau\right] \\ &= -\int_0^{t_0} \ddot{x}_g(\tau)\cos\omega_0(t_0+\bar{t}-\tau)d\tau \\ &= \dot{x}(t_0)\cos\omega_0\bar{t} - \omega_0 x(t_0)\sin\omega_0\bar{t} \end{aligned} \tag{2.45}$$

To compensate for the phase lag of $\pi/4$ rad, the time difference $\bar{t}$ is

$$\bar{t} = \pi/(4\omega_0) \tag{2.46}$$

Therefore, Eq. (2.45) reduces to

$$E[\dot{x}(t)] = \frac{1}{\sqrt{2}}\{\dot{x}(t_0) - \omega_0 x(t_0)\} \tag{2.47}$$

Thus, the phase compensating filter is

$$H_{PC}(i\omega) = \frac{\mathscr{F}[E[\dot{x}(t)]]}{\mathscr{F}[\dot{x}(t_0)]} = \frac{1}{\sqrt{2}}(1 - \frac{\omega_0}{i\omega}) \tag{2.48}$$

where $\mathscr{F}[\,]$ is the Fourier transform.

As shown in Fig. 2.15(a), the phase of $H_{PC}(i\omega)$ at ω_0 is 45 degrees ($\pi/4$ rad), compensating for the phase lag of the Butterworth filter. Another benefit to this filter is that it raises the amplitude in an inversely proportional manner at low frequencies, compensating for the difference between the target filter and the Butterworth filter.

Proposed filter

As shown in Fig. 2.15(c), the amplitude of $H_B \cdot H_{PC}$ has the same form as the target filter, except for its scale. It can be observed that the phase is adjusted to zero at ω_0, as one intended. Thus, the proposed filter is obtained as follows:

$$H_v(i\omega) = c_F \cdot H_B(i\omega) \cdot H_{PC}(i\omega) \tag{2.49}$$

where c_F is a modulating factor. The modulating factor is determined such that the amplitude of the proposed filter is identical to that of the target filter at ω_0:

$$|H_v(i\omega_0)| = \frac{1}{\sqrt{2}}c_F = 1 \tag{2.50}$$

Hence, Eq. (2.49) reduces to

$$H_v(i\omega) = \frac{\omega_0}{i\omega}\frac{i\omega - \omega_0}{i\omega + \omega_0} \tag{2.51}$$

Because it is practical to determine the control force using the measured displacement obtained by a local sensor, one can further reduce Eq. (2.42) to the following expression, provided that $h = \beta$ and the measured displacement in the frequency domain $X_m = X = {}_1X = {}_2X$:

$$F_c(i\omega) = \frac{i\omega}{\omega_0}H_v(i\omega) \cdot 2hk\ {}_1X = \frac{i\omega - \omega_0}{i\omega + \omega_0}2\beta k X_m \tag{2.52}$$

The first-order all-pass filter $(i\omega - \omega_0)/(i\omega + \omega_0)$ in Eq. (2.52) is identical to that proposed by Keivan et al. [47], in which the performance of the filter against various types of ground motion was compared to the approaches proposed by Biot and Makris [31, 40]. The filter of Eq. (2.52) can be implemented as the control law for an active control system. Passive methods will be explored next.

2.4.2 Passive rate-independent model

Consider a Maxwell element [70] with a stiffness of k_M and a damping coefficient of c_M, as shown in Fig. 2.16. The transfer function from the measured displacement X_m to the control force F_M has one pole and one zero, as shown in Fig. 2.17(a):

$$\frac{F_M(i\omega)}{X_m(i\omega)} = \frac{i\omega}{i\omega + \frac{k_M}{c_M}} k_M \tag{2.53}$$

Adding ideal linear negative stiffness in parallel with the Maxwell element, as shown in Fig. 2.18, shifts the zero to a positive real value so as to passively implement the first-order all-pass filter, as shown in Fig. 2.17(b) and Eq. (2.52).

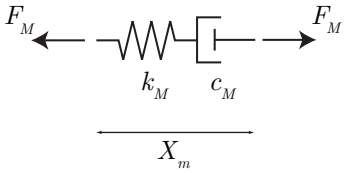

FIGURE 2.16: Maxwell element

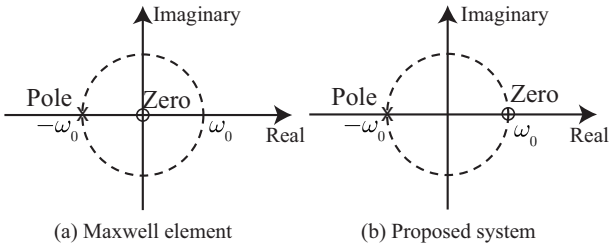

(a) Maxwell element (b) Proposed system

FIGURE 2.17: Pole zero map

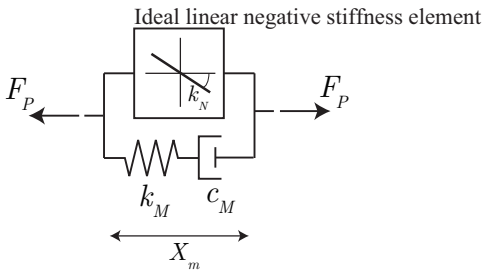

FIGURE 2.18: Conceptual model of passive RILD

The resultant force of the ideal linear negative stiffness and Maxwell elements, $F_P(i\omega)$, can be expressed in the frequency domain as follows,

$$F_P(i\omega) = \left(k_N + \frac{i\omega k_M}{i\omega + \frac{k_M}{c_M}}\right) X_m \tag{2.54}$$

where k_N is the stiffness of the negative stiffness element arranged in parallel with the Maxwell element. These parameters are determined as follows,

$$k_N = -2\beta k,\ k_M = 4\beta k,\ c_M = 4\beta m\omega_0, \tag{2.55}$$

and thus Eq. (2.54) reduces to

$$F_P(i\omega) = \frac{i\omega - \omega_0}{i\omega + \omega_0} 2\beta k X_m. \tag{2.56}$$

From Eq. (2.56), it can readily be seen that the control force provided by the proposed model is expressed exactly the same way as that in Eq. (2.52), implying that the first-order all-pass filter can be represented by an ideal linear physical model.

To investigate the performance of the passive RILD model proposed in this study, the seismic responses of the base-isolated five-story building (described in Section 3) incorporated with the proposed and LVD models were investigated by conducting time history analyses. For the RILD model, a passive rate-independent model with an ideal linear negative stiffness element was used because the damping force generated by the passive RILD model is identical to that of the active control model using the first-order all-pass filter. For this purpose, one employed the north–south component of the ground motion recorded at the JMA in the 1995 Kobe Earthquake and the east–west component of ground motion recorded at the CDAO site during the 2003 Tokachi-oki Earthquake. The damping ratios for the linear viscous damping and passive rate-independent damping models are determined such that they were the same: ${}_1\xi = h = 0.2$ and ${}_2\xi = \beta = 0.2$. The properties of the two damping models are listed in Table 2.6.

TABLE 2.6: Properties of LVD and passive RILD models

Property	Linear viscous	Passive rate-independent linear
Damping coefficient (kN·s/m)	8 036	16 072
Positive stiffness (kN/m)	—	25 004
Negative stiffness (kN/m)	—	-12 502

The time-history responses of the structure incorporated with the proposed RILD and LVD models are shown in Figs. 2.19 and 2.20, and the corresponding hysteresis loops for the two models under each type of ground motion are shown in Fig. 2.21.

From Fig. 2.19(a), it can be seen that under the ground motion induced by the Kobe Earthquake, the isolator displacements of the structure yielded by the two linear damping models are similar. Conversely, the rooftop response accelerations of the structure with the proposed model are lower than those of the structure with the LVD model. This is because the damping forces of the proposed model are lower than those of the latter, whereas the isolator displacements are similar, as shown in Fig. 2.21(a).

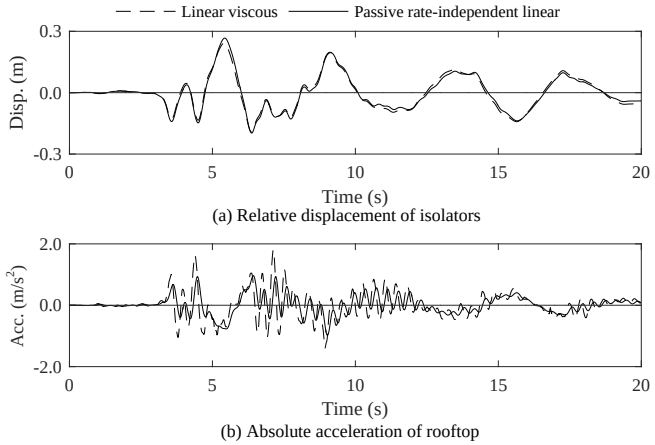

FIGURE 2.19: Response of the structures with different damping models (JMA Kobe 1995 NS)

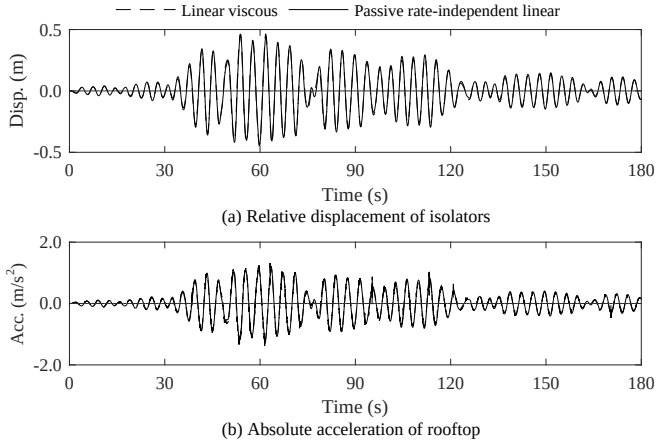

FIGURE 2.20: Response of the structures with different damping models (CDAO Tokachi-oki 2003 EW)

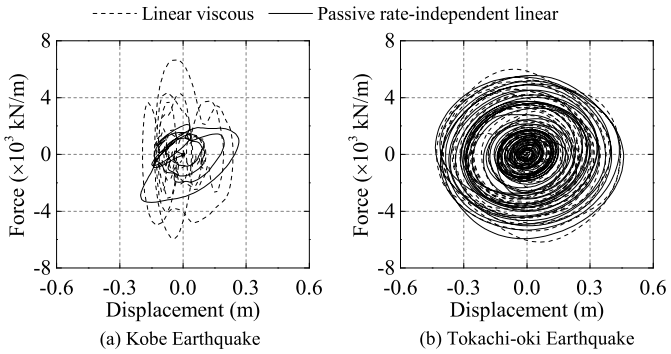

FIGURE 2.21: Hysteresis loops of different damping models

For the Tokachi-oki Earthquake, where the ground motion is dominated by low-frequency components, the two damping models exhibit similar energy dissipation behaviors, as shown

in Fig. 2.21(b). Thus, in Fig. 2.20, both the isolator displacements and rooftop response accelerations of the two differently-damped structures are similar, supporting the conclusions obtained in Section 2.2. This implies that the performance of the proposed model is not compromised, even when it is excited by ground motion containing low-frequency components. It should also be pointed out that in this case, because the ground motion contains dominant low-frequency components, whose frequencies are close to the isolation frequency, the seismic responses of the structures are dominated by these components. Thus, the damping devices show less dependency on the excitation frequency, resulting in ellipse-shaped hysteresis loops, as shown in Fig. 2.21(b).

2.4.3 Nonlinear effect of negative stiffness device

To realize the passive rate-independent model proposed in the above section, it is crucial to create a linear negative stiffness element. In this regard, the most straightforward way for creating effective linear negative stiffness is simply achieved by reducing the horizontal stiffness of the isolators. Alternatively, the use of the mechanical devices developed by Sarlis et al. [71] and Sun et al. [72] may be a suitable means for implementing negative stiffness. Proper design on these devices is required for use in the proposed rate-independent model because they can exhibit strong nonlinearity under large deformations.

Here, for example, a simple available NSD introduced in reference [71] is considered, as shown in Fig. 2.22.

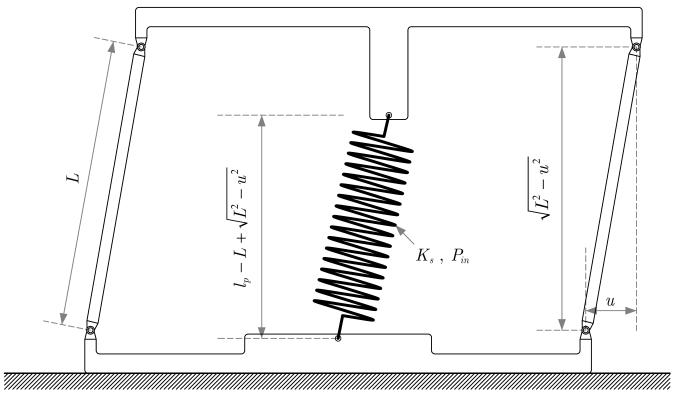

FIGURE 2.22: A simple negative stiffness device under large deformation

The NSD consists of a precompressed spring used to generate a horizontal force in the direction of displacement and thus create the negative stiffness, and a double chevron self-containing system to resist the preload in the spring and prevent the vertical component of the preload from transferring to the structure. Ignoring the height loss of the system due to the pendulum motion of the hinged column, the horizontal displacement-force relationship of the NSD can be expressed as follows [71],

$$F = -\left(\frac{P_{in} + K_s l_p}{\sqrt{l_p^2 + u^2}} - K_s\right)\frac{L - l_p}{L}u \tag{2.57}$$

where F and u are the horizontal force and lateral displacement of the device, respectively; P_{in} and K_s are the preload and spring rate of the compressed spring, respectively; l_p and L are the spring length and the height of the hinged column, respectively.

It should be pointed out that Eq. (2.57) holds when u is relatively small compared to the column height. However, when used in a base-isolation system, the NSD may suffer a large displacement, resulting in a relatively large rotation of the hinged column. In such cases, the height loss of the device should be considered. When the device is displaced by u at the top, the height of the hinged column becomes $\sqrt{L^2-u^2}$, and thus the spring length becomes $\sqrt{(l_p+\sqrt{L^2-u^2}-L)^2+u^2}$. After some calculations, the horizontal force provided by the NSD can be expressed as follows,

$$F=\left(\frac{P_{in}+K_s l_p}{\sqrt{(l_p+\sqrt{L^2-u^2}-L)^2+u^2}}-K_s\right)\frac{u(l_p-L)}{\sqrt{L^2-u^2}} \tag{2.58}$$

It should be noted that when u is small relative to the column height h, the above equation reduces to Eq. (2.57). To further illustrate the differences between the forces obtained by Eqs. (2.57) and (2.58), for example, an NSD is designed to generate a tangent stiffness at $u=0$ equal to the desired linear negative stiffness listed in Table 2.6. The properties of the designed NSD are listed in Table 2.7. Although the values of preload and compressed spring stiffness used here are much larger than those given in reference [71], it is still possible to realize the designed NSD because one can increase the number of NSDs and arrange them in parallel in the isolation layer so that the designed preload and compressed spring stiffness are achieved. A detailed method for designing the NSD for the implementation of the proposed rate-independent damping model is explored in reference [73].

TABLE 2.7: Properties of the designed NSD

Property	Symbol	Value
Preload	P_{in}	18 752 kN
Spring stiffness	K_s	37 505 kN/m
Spring length	l_p	0.75 m
Hinged column height	L	1.50 m

Figure 2.23(a) shows the displacement-force relations of the designed NSD obtained by Eqs. (2.57) and (2.58), respectively, as well as that of the desired linear negative stiffness listed in Table 2.6, while Figure 2.23(b) shows the normalized forces of the three NSDs divided by that of the linear NSD against the displacement. It should be noted that at $u=0$, the normalized force $F/(k_N u)$ equivalently represents the ratio of the tangent stiffness of the nonlinear NSD to the linear negative stiffness. Therefore, the values shown in Figure 2.23(b) is unity at $u=0$ even though the force provided by the NSDs are both equal to zero.

Comparing the forces obtained by Eqs. (2.57) and (2.58) in Figure 2.23, it can be seen

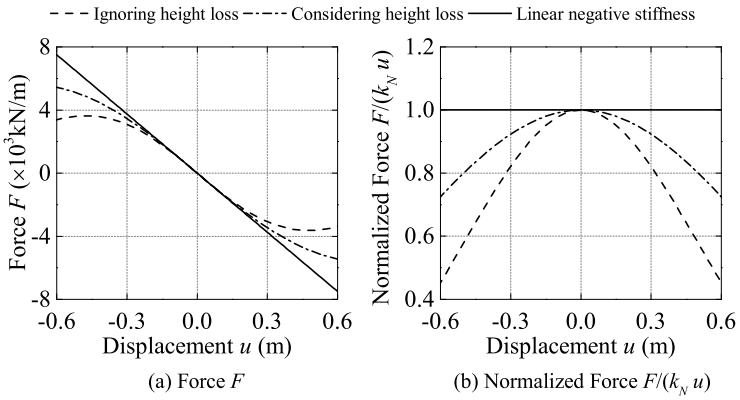

FIGURE 2.23: Deformation-force relations of different NSDs

that when the displacement u is small, the forces obtained by the two equations are similar, and are both close to the force provided by the desired linear NSD. However, given relatively large displacements, the forces obtained by Eq. (2.57) are obviously lower than those obtained using Eq. (2.58), implying that ignoring the height loss due to the pendulum motion of the hinged column may lead to underestimation of the forces provided by the nonlinear NSD under large deformations. Comparing the forces obtained by Eq. (2.58) and the ideal linear NSD, it can be seen that within the displacement range of interest (e.g. lower than 0.3 m), the nonlinear and linear NSDs behave similarly, and the relative differences between their forces are below 10% at a displacement of 0.3 m and below 20% at a displacement of 0.45 m, implying that using a linear negative stiffness element would provide a good approximation of the behavior of the designed nonlinear NSD when the displacement is within the displacement range of interest. To verify this observation, a passive nonlinear rate-independent model was designed by replacing the ideal linear negative stiffness element as the designed nonlinear NSD given in Table 2.7, while the seismic performance of the base-isolated five-story building (described in Section 3) incorporating a nonlinear rate-independent model was investigated by conducting nonlinear time history analyses. For this purpose, one employed the north–south component of the ground motion recorded at the JMA in the 1995 Kobe Earthquake and the east–west component of ground motion recorded at the CDAO site during the 2003 Tokachi-oki Earthquake. Figure 2.24 shows the hysteresis loops of the nonlinear rate-independent model represented by Eq. (2.58) and the ideal rate-independent linear model used in Section 2.4.2 under each type of ground motion.

In Figure 2.24, small differences can be observed between the hysteresis loops of the two types of rate-independent models under each type of ground motion, even though these two models experience a maximum displacement over 0.4 m under the Tokachi-oki Earthquake. This means that the ideal linear negative stiffness element provides a good approximation of the well designed nonlinear NSD, consistent with the observation on the displacement-force relations shown in Figure 2.23. Therefore, even though the designed NSD is indeed nonlinear, the nonlinear effect of the NSD can be neglected within the deformation of interest if properly designed. In this case, it can be approximated as a linear negative stiffness element

for realizing the proposed rate-independent damping model. The NSD design example given in this section provides a design alternative for creating a physical linear negative stiffness element within the displacement range of interest, making the proposed passive model more attractive for approximating the performance of RILD.

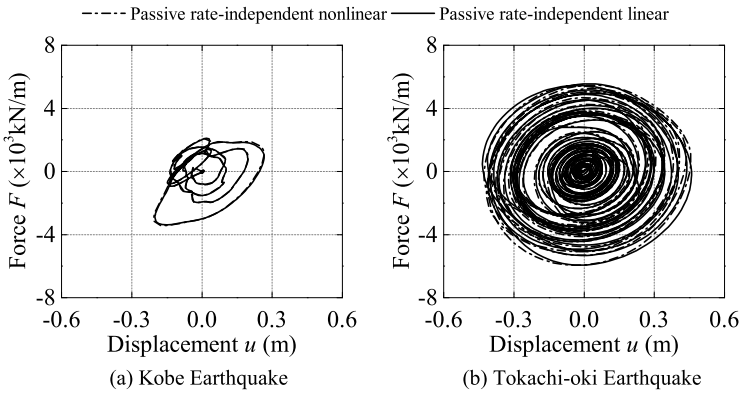

FIGURE 2.24: Hysteresis loops of different rate-independent models

2.5 Chapter conclusions

In this chapter, we discussed the behavior of RILD in long-period structures subjected to strong ground motion. RILD is known to yield almost identical response displacements and velocities to those of LVD, whereas the damping forces generated are substantially different, resulting in substantially different floor-response accelerations. This is because the values of the damping force transfer function for RILD in the frequency region higher than the fundamental natural frequency of the structure are lower than those of LVD, whereas the displacement and velocity transfer functions of the two linear damping elements are almost identical.

In particular, when a long-period structure is subjected to ground motion containing high-frequency components, RILD yields lower floor-response accelerations compared to other damping devices without increasing the response displacements. The results of the incremental dynamic analyses and performance curves obtained in Section 2.3 by using an example base-isolated MDF structure subjected to strong ground motion illustrated the benefits of RILD.

In terms of practical applications, both active and passive methods were proposed to implement the derived model for RILD. Comparisons between the seismic responses of structures incorporated with the proposed and LVD models show that when excited by high-frequency-dominated ground motion, the structure equipped with the proposed rate-independent model yielded lower damping forces than those with LVD model. However, the two structures exhibited similar isolator displacements. Furthermore, the performance of the proposed passive model was not compromised, even when excited by ground motion containing low-frequency components. Thus, this study exemplified the feasibility of

the proposed method to mimic RILD in reducing the floor-response acceleration without increasing the displacement. A design example of negative stiffness device given in this study provides an alternative for approximating a physical linear negative stiffness element within the displacement range of interest, making the proposed passive model more attractive for mimicking the performance of RILD. The passive rate-independent mechanical model proposed in this study is expected to be a viable option for improving the seismic performance of low-frequency structures subjected to strong ground motion.

Passive control does not rely on external power, requires less maintenance in general, and is more readily accepted by the design industry.

Chapter 3

A Unified Framework of Causal RILD Models

3.1 Introduction

In this chapter, some established RILD models are first reviewed in detail, and then a novel causal filter is generalized from the bilinear digital filter used by Keivan et al. [47], in order to achieve an improved approximation of ideal RILD in the sense of an extended frequency range, over which the rate-independent dissipation behavior can be mimicked. The novel filter is characterized by a real-valued tunable parameter (say α), which is confined to the range from zero to unity in this study. When interpreted from the frequency domain into the time domain, the novel filter is found to correspond to a mechanical model, whose constitutive law is mathematically described by using the concept of fractional derivative. Such a concept was introduced by Gemant [74] for describing the dynamic properties of viscoelastic bodies several decades ago. The main advantage of the fractional-order derivative over the conventional integer-order derivatives is that much reduced number of empirical parameters can be used to accurately describe the dynamic properties of many engineering materials [75, 76]. Indeed, some attempts have already been made to approximate RILD by virtue of similar concepts [35, 36], however, to the best knowledge of the author, there are still few discussions on the relationships between a fractional-order model with existing causal models for approximating the behavior of RILD (e.g., Biot, Makris, and tuned Maxwell-Wiechart (TMW) models). In this chapter, some subtle relationships between the proposed model with the existing models are to be revealed. This contributes to the development of a unified framework of causally approximated RILD models and facilitates the theoretical understanding of RILD from a more general viewpoint.

For numerical implementation of the proposed model, a time-domain technique is to be developed by directly calculating the fractional derivative on the basis of the so-called L1 algorithm [55]. Such a method is thought to be useful and convenient for application, because with little calculations associated with the coefficient estimation, it can be readily embedded into established numerical integration schemes, e.g., the Newmark's integration scheme, and thus used for response history analyses of structural systems incorporated with RILD elements. The computational efficiency of this technique can be largely improved without significant loss of simulation accuracy if the fixed memory principle is applied.

The remainder of this chapter is organized as follows. In Section 3.2, some representative existing models for RILD are to be reviewed in detail. The frequency- and time-domain representations of the proposed model are to be derived, and the relations between the proposed model with those existing causal models for RILD are to be discussed and mathematical proved in Section 3.3. Then, in Section 3.4, an L1-algorithm-based internal variable method is to be developed for nonlinear dynamic analyses of structural systems incorporated with RILD elements, and in Section 3.5, the effectiveness of the developed method is verified by using numerical examples. Finally, some conclusions are presented.

3.2 Some representative existing models of RILD

3.2.1 An ideal RILD model

A popular model for RILD is known as complex stiffness which consists of a linear spring and an ideal RILD element coupled in parallel, as shown in Fig. 3.1. It is usually represented in terms of dynamic stiffness, which is defined as a transfer function from deformation to resistive force, i.e.,

$$\mathscr{H}_{\mathrm{I}}(i\omega) = \frac{F(i\omega)}{X(i\omega)} = k_0\left[1 + \eta\mathcal{Z}_{\mathrm{I}}(i\omega)\right] \tag{3.1}$$

where k_0 is spring stiffness; η denotes loss factor; $\mathcal{Z}_{\mathrm{I}}(i\omega)$ denotes the normalized dynamic stiffness of the ideal RILD element, defined as a damping function as follows,

$$\mathcal{Z}_{\mathrm{I}}(i\omega) = 0 + i\,\mathrm{sgn}(\omega) \tag{3.2}$$

where $i = \sqrt{-1}$ and $\mathrm{sgn}(\cdot)$ denotes the signum function. Applying inverse Fourier transformation to Eq.(3.2) gives [77]

$$z_{\mathrm{I}}(t) = \mathscr{F}^{-1}[\mathcal{Z}_{\mathrm{I}}(i\omega)] = -\frac{1}{\pi t} \tag{3.3}$$

where $\mathscr{F}^{-1}[\cdot]$ denotes the inverse Fourier transform. The above equation implies that this model is noncausal because it yields a non-zero force prior to the application of an impulsive deformation, i.e., $z_{\mathrm{I}}(t<0) \neq 0$.

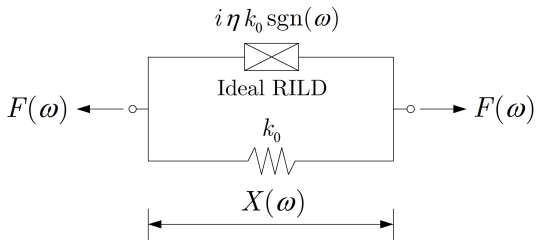

FIGURE 3.1: A noncausal RILD model

The damping kernel function of this model is obtained by applying inverse Fourier transform to the impedance function, which is defined as the transfer function from velocity to

damping force, as follows,

$$q_{\mathrm{I}}(t) = \mathscr{F}^{-1}\left[\frac{\mathscr{Z}_{\mathrm{I}}(i\omega)}{i\omega}\right] = -\frac{1}{\pi}\ln|t| \tag{3.4}$$

which can also be obtained by applying an infinite integration of $z_{\mathrm{I}}(t)$ in Eq.(3.3) with respect to t, because the property of Fourier transform suggests the relation $\dot{q}_{\mathrm{I}}(t) = z_{\mathrm{I}}(t)$, where the overdot denotes the derivative with respect to t.

The response force generated by this noncausal model from an input deformation $x(t)$ can be expressed as follows,

$$f_{\mathrm{I}}(t) = k_0 x(t) * [\delta(t) + \eta\, z_{\mathrm{I}}(t)] = k_0\,[x(t) + \eta\,\hat{x}(t)] \tag{3.5}$$

where the asterisk $*$ denotes a convolution integral; $\delta(t)$ denotes the Dirac's delta function, which is defined as the inverse Fourier transform of unity; the hat $'\hat{}'$ denotes Hilbert transform, which can be expressed as follows,

$$\hat{x}(t) = x(t) * z_{\mathrm{I}}(t) = -\frac{1}{\pi}\int_{-\infty}^{\infty}\frac{x(\tau)}{t-\tau}d\tau \tag{3.6}$$

which again implies that this model is noncausal because its response force depends on not only the past input deformations, but also those in the future. This noncausal model is impossible to be physically realized by using real-life devices and also challenging to be numerically implemented in a nonlinear simulation problem, therefore, causal models which can approximate ideal RILD in some sense were pursued for practical applications.

3.2.2 Biot model

The first viscoelastic model yielding approximated rate-independent dissipation behavior was proposed by Biot [31]. A mechanical representation of Biot model can be constructed by using an infinite number of Maxwell elements [32], which is thought to be a special case of the Maxwell-Wiechert model [33, 46] shown in Fig. 3.2, where c_j and k_j denote the damping coefficient and stiffness of the j-th Maxwell branch, respectively; v_j is an internal valuable, denoting the deformation of the j-th dashpot.

For a Maxwell-Wiechert model, the dynamic stiffness is written as follows,

$$\mathscr{H}(i\omega) = k_0 + \sum_{j=1}^{n} k_j \frac{i\omega}{i\omega + r_j} \tag{3.7}$$

where r_j denotes the ratio of the spring stiffness and damping coefficient of the j-th Maxwell element, i.e., $r_j = k_j/c_j$, which is also known as a relaxation frequency or the inverse of a relaxation time.

Provided that the damping coefficient c_j of each dashpot $(j = 1, 2, \ldots, n)$ is constant and two neighboring springs have stiffnesses of k_j and k_{j-1}, respectively, which are related with

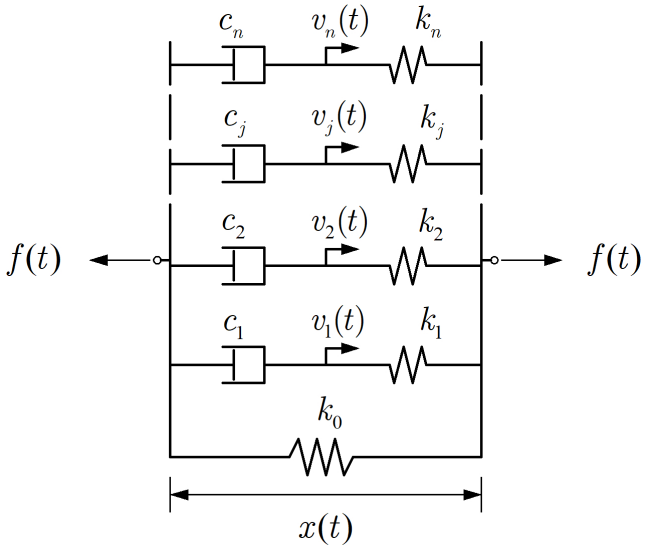

FIGURE 3.2: Maxwell-Wiechert model

each other by Eq.(3.8)

$$k_j = \frac{2\eta k_0}{\pi}\frac{k_j - k_{j-1}}{k_j} = k_1\frac{\Delta k_j}{k_j} = k_1\frac{\Delta r_j}{r_j} \tag{3.8}$$

with $j = 2, 3, \ldots, n$, and $k_1 = 2\eta k_0/\pi$, then one can rewrite Eq.(3.7) as follows,

$$\mathscr{H}(i\omega) = k_0\left(1 + \frac{2\eta}{\pi}\sum_{j=1}^{n}\frac{i\omega}{i\omega + r_j}\frac{\Delta r_j}{r_j}\right) \tag{3.9}$$

Letting $n \to \infty$ and r_j $(j = 1, 2, \ldots, n)$ continuously vary from ε to ∞, and replacing r_j as r, one can express the dynamic stiffness as follows,

$$\mathscr{H}(i\omega) = k_0\left[1 + \frac{2\eta}{\pi}\int_{\varepsilon}^{\infty}\left(\frac{\omega^2/r}{\omega^2 + r^2} + \frac{i\omega}{\omega^2 + r^2}\right)dr\right] \tag{3.10}$$

Performing the integral in Eq.(3.10) gives the dynamic stiffness of Biot model as follows,

$$\mathscr{H}_{\mathrm{B}}(i\omega) = k_0\left\{1 + \frac{2\eta}{\pi}\left[\ln\sqrt{1 + \left(\frac{\omega}{\varepsilon}\right)^2} + i\arctan\left(\frac{\omega}{\varepsilon}\right)\right]\right\} \tag{3.11}$$

where $\arctan(\cdot)$ is the inverse tangent function. By introducing the complex logarithm function $\ln(1 + i\omega/\varepsilon)$ *, defined over the principal branch $-\pi/2 \le \arctan(\omega/\varepsilon) \le \pi/2$ on the complex-plane, one can alternatively rewrite Eq.(3.11) in a more compact form as follows,

$$\mathscr{H}_{\mathrm{B}}(i\omega) = k_0\left[1 + \frac{2\eta}{\pi}\ln\left(1 + \frac{i\omega}{\varepsilon}\right)\right] \tag{3.12}$$

*Strictly speaking, the complex logarithm function is a multi-valued function, which is different from the single-valued natural logarithm function defined in the real axis. However, the same symbol of $\ln(\cdot)$ is used here for both the two cases for convenience.

Corresponding to Eq.(3.1), the above equation can be expressed as follows,

$$\mathscr{H}_{\mathrm{B}}(i\omega) = k_0 \left[1 + \eta \mathscr{Z}_{\mathrm{B}}(i\omega)\right] \tag{3.13}$$

where the damping function of Biot model is given as follows,

$$\mathscr{Z}_{\mathrm{B}}(i\omega) = \frac{2}{\pi}\left[\ln\sqrt{1+\left(\frac{\omega}{\varepsilon}\right)^2} + i\arctan\left(\frac{\omega}{\varepsilon}\right)\right] = \frac{2}{\pi}\ln\left(1 + i\,\frac{\omega}{\varepsilon}\right) \tag{3.14}$$

Applying inverse Fourier transform to Eq.(3.14) gives

$$z_{\mathrm{B}}(t) = \frac{2}{\pi}\int_{\varepsilon}^{\infty}\left(\frac{\dot{u}(t)}{r} - \frac{u(t)}{e^{rt}}\right)dr = -\frac{2}{\pi}\frac{d}{dt}\left[\mathrm{Ei}(-\varepsilon t)u(t)\right] \tag{3.15}$$

where $u(t)$ denotes Heaviside's unit step function (i.e., $u(t) = 0$, if $t \leq 0$; otherwise, $u(t) = 1$); $\mathrm{Ei}(-\varepsilon t)$ denotes the exponential integral, which can be expressed as follows [78],

$$\mathrm{Ei}(-\varepsilon t) = \int_{\varepsilon}^{\infty}\frac{-1}{e^{rt}}\frac{dr}{r} = \ln|\varepsilon t| + \gamma_0 + \sum_{n=1}^{\infty}\frac{(-1)^n(\varepsilon t)^n}{n\,n!} \tag{3.16}$$

where $\gamma_0 \doteq 0.577$ denotes the Euler constant. The damping kernel function of Biot model is defined as follows,

$$q_{\mathrm{B}}(t) = \mathscr{F}^{-1}\left[\frac{\mathscr{Z}_{\mathrm{B}}(\omega)}{i\omega}\right] = -\frac{2}{\pi}\mathrm{Ei}(-\varepsilon t)u(t) \tag{3.17}$$

Thus, the response force provided by Biot model can be obtained as follows,

$$f_{\mathrm{B}}(t) = k_0[x(t) + \eta\,\dot{x}(t) * q_{\mathrm{B}}(t)] \tag{3.18}$$

Substituting Eq.(3.17) into the above equation gives

$$f_{\mathrm{B}}(t) = k_0\left\{x(t) - \frac{2\eta}{\pi}\dot{x}(t) * \left[\mathrm{Ei}(-\varepsilon t)u(t)\right]\right\} \tag{3.19}$$

which coincides with the time-domain representation of Biot model given in reference [32].

3.2.3 Makris model

An alternative explanation for the noncausality of the ideal RILD model is that the real and imaginary parts of its dynamic stiffness fail to relate with each other by Hilbert transform. Such relations, often referred to as Kramers-Kronig relations, are known as the sufficient and necessary conditions for a strictly proper transfer function to ensure the causality in the strict sense [79]. By modifying the real part of Eq.(3.2) into the Hilbert transform of its imaginary part, Makris [40] constructed a causal RILD model having a dynamic stiffness as follows,

$$\mathscr{H}_{\mathrm{M}}(i\omega) = k_0\left[1 + \eta\,\mathscr{Z}_{\mathrm{M}}(i\omega)\right] \tag{3.20}$$

where the damping function of the Makris model is given as follows,

$$\mathcal{Z}_{\mathrm{M}}(i\omega) = \frac{2}{\pi} \ln \left| \frac{\omega}{\varepsilon} \right| + i \operatorname{sgn} \left(\frac{\omega}{\varepsilon} \right) \tag{3.21}$$

It may be noticed that Eq.(3.14) approaches to Eq.(3.21) when $\omega \gg \varepsilon$, which means that Makris model is a high-frequency limiting case of Biot model. Applying inverse Fourier transform to Eq.(3.21) gives

$$z_{\mathrm{M}}(t) = \mathscr{F}^{-1} \left[\mathcal{Z}_{\mathrm{M}}(i\omega) \right] = -\frac{2u(t)}{\pi t} \tag{3.22}$$

A damping kernel function of this model is given as follows [40],

$$q_{\mathrm{M}}(t) = \mathscr{F}^{-1} \left[\frac{\mathcal{Z}_{\mathrm{M}}(i\omega)}{i\omega} \right] = -\frac{2}{\pi} \left(\ln |\varepsilon t| + \gamma_0 \right) u(t) \tag{3.23}$$

It may be noted that Eq.(3.17) reduces to the above equation as εt tends to zero (so that the last term in Eq.(3.16) vanishes). The response force provided by the Makris model from an input deformation $x(t)$ can be obtained as follows,

$$f_{\mathrm{M}}(t) = k_0 \left[x(t) + \eta \, \dot{x}(t) * q_{\mathrm{M}}(t) \right] \tag{3.24}$$

Substituting Eq.(3.23) into the above equation gives

$$f_{\mathrm{M}}(t) = k_0 \left\{ \left(1 - \frac{2\eta}{\pi} \gamma_0 \right) x(t) - \frac{2\eta}{\pi} \dot{x}(t) * [\ln |\varepsilon t| u(t)] \right\} \tag{3.25}$$

which includes a negative constant term in the displacement-dependent part. This suggests a negative stiffness element may be used for physical approximation of RILD [49, 73].

3.2.4 Nakamura model

The above approximated causal RILD models can be simply expressed in the frequency domain, but their time-domain representations are thought to be relatively complex, because they are involved with calculations of convolution integrals, which may compromise their computational efficiencies for some practical applications. To reduce the computational burden for analyzing the RILD system involved with the transformation from the frequency domain into the time domain, Nakamura [45] proposed a causal approximation of RILD having dynamic stiffness as follows,

$$\mathscr{H}_{\mathrm{N}}(i\omega) = k_0 \left[1 + \eta \, \mathcal{Z}_{\mathrm{N}}(i\omega) \right] \tag{3.26}$$

where the damping function of the Nakamura model is given as follows,

$$\mathcal{Z}_{\mathrm{N}}(i\omega) = \hat{Z}'(\omega) + iZ'(\omega) + i\frac{2\omega}{\omega_m} \tag{3.27}$$

with the auxiliary function $Z'(\omega)$ defined as follows,

$$Z'(\omega) = (2n-1) - \frac{2\omega}{\omega_m} \tag{3.28}$$

for $n = 1(0 \leq \omega < \omega_m)$, $n = 2(\omega_m \leq \omega < 2\omega_m)$, $n = 3(2\omega_m \leq \omega < 3\omega_m)$, ..., where ω_m denotes the length of each subinterval over the positive frequency axis. This model is thought to be causal because the first two terms in the r.h.s of Eq.(3.27) are the Hilbert transform pairs, i.e., satisfying the Kramers-Kronig relations, whereas the remaining irregular term corresponds to the derivative of the Dirac's delta function in the time domain, which is thought to be causal.

Different from the other approximations of RILD, the dynamic stiffness of Nakamura model is discontinuous with respect to the frequency. Thus, an analytical expression of further simplifying Eq.(3.27) is not available in a general case, and numerical algorithms for conducting the Hilbert transform are necessary to determine the dynamic stiffness at discrete frequency points. The obtained discrete data are then used for regression analyses in order to determine the coefficients used for the following approximation [44]:

$$\mathscr{H}_{\mathrm{N}}(i\omega) \approx \bar{\mathscr{H}}_{\mathrm{N}}(i\omega) = -\omega^2 m_0 + i\omega c_0 + k_0 + \left(i\omega \sum_{j=1}^{N-2} c_j e^{-i\omega T_j} + \sum_{j=1}^{N-1} k_j e^{-i\omega T_j} \right) \tag{3.29}$$

where a bar denotes the approximated value to distinguish from the exact one; m_0, c_j, and k_j $(j = 0, 1, 2, ...)$ denote the coefficients to be estimated; N denotes the number of sample data; T_j denotes the delayed time. Then, the response force provided by the Nakamura model can be approximated in the time domain as follows,

$$f_{\mathrm{N}}(t) \approx \bar{f}_{\mathrm{N}}(t) = m_0 \ddot{x}(t) + c_0 \dot{x}(t) + k_0 x(t) + \left[\sum_{j=1}^{N-2} c_j \dot{x}(t - T_j) + \sum_{j=1}^{N-1} k_j x(t - T_j) \right] \tag{3.30}$$

The above method is thought to reduce the computational burden involved with the convolution integral, when time-domain analysis techniques are preferred to conduct dynamic analyses for structural systems incorporated with RILD, as to be discussed in Chapter 4. However, it is still challenging to find a mechanical representation of the Nakamura model, so that it may be realized by using real-life devices, which can be installed in an actual building structure for seismic protection purposes.

3.2.5 Tuned Maxwell-Wiechert model

For numerical implementation, a Prony series with a finite and limited number of relaxation functions was used by Makris and Zhang [41] to approximate the behavior of Biot model. Such a series is also known as the relaxation modulus of a Maxwell-Wiechert model, as shown in Fig. 3.2. Furthermore, a Prony series was used by Spanos and Tsavachidis [42] to develop a recursive procedure for dynamic analysis of structural systems incorporated with Biot model. To the best knowledge of the author, it was Genta and Amati [33] who first proposed the concept of tuned Maxwell-Wiechert (TMW) model so that its loss moduli can

fit those of the reference noncausal RILD over a frequency range of interest. Similar concept was later used by Reggio et al. [34, 46] for system identification and used by Huang et al. [51] for nonlinear analysis of rate-independently damped structures.

The dynamic stiffness of a TMW model is given as follows,

$$\mathscr{H}_{\mathrm{T}}(i\omega) = k_0\left(1 + \eta\mathcal{Z}_{\mathrm{T}}(i\omega)\right) \tag{3.31}$$

where the damping function of the TMW model is given as follows,

$$\mathcal{Z}_{\mathrm{T}}(i\omega) = \sum_{j=1}^{n} \phi_j \frac{i\omega}{i\omega + r_j} \tag{3.32}$$

where ϕ_j is a tunable parameter with respect to a discrete frequency point $\omega = r_j$, or physically represents the normalized stiffness of the j th Maxwell element with a relaxation frequency of r_j. The damping kernel function of a TMW model is written as follows,

$$q_{\mathrm{T}}(t) = \sum_{j=1}^{n} \phi_j e^{-r_j t} u(t) \tag{3.33}$$

With sufficient terms, Eq.(3.33) can be used to approximate any physical relaxation process. To let the imaginary part of Eq.(3.31) approach the reference ideal RILD over a frequency range, Huang et al. [51] suggested an analysis algorithm to determine the parameters ϕ_j, r_j, and value of n. With Eq.(3.33), the response force generated by a TMW model can be expressed as follows,

$$f_{\mathrm{T}}(t) = k_0\left[x(t) + \eta\dot{x}(t) * \sum_{j=1}^{n} \phi_j e^{-r_j t} u(t)\right] \tag{3.34}$$

The above model is thought to be suitable for numerical implementation of a structural model with RILD, because available commercial softwares, like ABAQUS, provide entrances to setting the parameters ϕ_j and r_j ($j = 1, 2, \ldots, n$), and also state-space formulations are available for numerically analyzing the dynamic behavior of a structural system incorporated with the TMW model.

3.3 A unified causal RILD model

3.3.1 The proposed model for RILD

To approximate the ideal RILD element defined in Eq.(3.2), an alternative way is to use a first-order all-pass filter [47] as follows

$$\mathcal{Z}_1(i\omega) = \frac{i\omega - \varepsilon}{i\omega + \varepsilon} \tag{3.35}$$

which can provide an amplitude of unity all over the frequency and also a phase advanced to the deformation by $\pi/2$ rad at $\omega = \varepsilon$. Such a filter was found to be a viable option to

mimic the behavior of ideal RILD for seismic protection of low-frequency structures [48, 50]. However, the above filter is thought to suffer a strongly rate-dependent loss modulus, which may compromise its capability to simulate the structural inherent damping.

Here, the first-order all-pass filter is generalized and extended to a fractional-order filter defined in the following form,

$$\mathcal{Z}_\alpha(i\omega) = \beta_\alpha \frac{(i\omega)^\alpha - \varepsilon^\alpha}{(i\omega)^\alpha + \varepsilon^\alpha} \tag{3.36}$$

where the real variable α is defined as a tunable parameter of the proposed filter ($0 \leq \alpha \leq 1$); $(i\omega)^\alpha$ is uniquely defined as $(i\omega)^\alpha = |\omega|^\alpha \exp[i\,\alpha\,\mathrm{sgn}(\omega)\,\pi/2]$; β_α is a real-valued modulating function with respect to α. Letting the amplitude of the filter be modulated as unity (i.e. the same as the ideal RILD) at $\omega = \varepsilon$ gives

$$\beta_\alpha = \cot(\alpha\pi/4) \tag{3.37}$$

where $\cot(\cdot)$ denotes the cotangent function. Then, a fractional-order filter for approximation of RILD is proposed as follows,

$$\mathcal{Z}_\alpha(i\omega) = \cot\left(\frac{\alpha\pi}{4}\right) \frac{(i\omega)^\alpha - \varepsilon^\alpha}{(i\omega)^\alpha + \varepsilon^\alpha} \tag{3.38}$$

which reduces to Eq.(3.35) as α tends to unity. Corresponding to Eq.(3.1), one can construct a fractional-order RILD model having a dynamic stiffness as follows,

$$\mathcal{H}_\alpha(i\omega) = k_0[1 + \eta\ \mathcal{Z}_\alpha(i\omega)] \tag{3.39}$$

which reduces to Keivan model [47] in the case of $\alpha = 1$.

Compared with the first-order all-pass filter, the proposed filter can provide a less rate-dependent loss modulus, as shown in Fig. 3.3, where the real and imaginary parts of the proposed filter (e.g., $\alpha = 0.1$), the first-order all-pass filter, and ideal RILD are compared. It is shown that the proposed filter (e.g., $\alpha = 0.1$) provides an improved approximation of ideal RILD in terms of loss modulus, while yielding similar storage moduli as those of a first-order all-pass filter over a frequency range near $\omega = \varepsilon$.

3.3.2 Causality of the proposed model

Here, the causality of the proposed model is first investigated. To this end, letting $0 < \alpha < 1$, the damping function of the proposed RILD model is expressed as follows,

$$\mathcal{Z}_\alpha(i\omega) = \beta_\alpha \frac{(i\omega)^\alpha - \varepsilon^\alpha}{(i\omega)^\alpha + \varepsilon^\alpha} = \beta_\alpha\,[2i\omega\mathcal{G}(i\omega) - 1] \tag{3.40}$$

where an auxiliary function $\mathcal{G}(i\omega) = (i\omega)^{\alpha-1}/[(i\omega)^\alpha + \varepsilon^\alpha]$ is introduced.

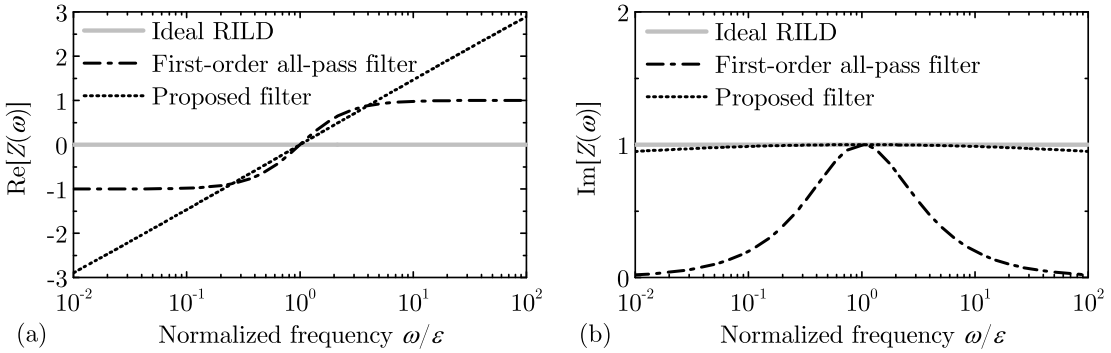

FIGURE 3.3: Comparison between the damping functions of different RILD elements: (a) real and (b) imaginary parts.

Applying inverse Fourier transform to Eq.(3.40) gives

$$z_\alpha(t) = \mathscr{F}^{-1}[\mathcal{Z}_\alpha(i\omega)] = \beta_\alpha\left[2\dot{g}(t) - \dot{u}(t)\right] \tag{3.41}$$

where $g(t)$ denotes the inverse Fourier transform of $\mathscr{G}(i\omega)$, i.e.

$$g(t) = \mathscr{F}^{-1}[\mathscr{G}(i\omega)] = \frac{1}{2\pi}\int_{-\infty}^{\infty}\frac{(i\omega)^{\alpha-1}}{(i\omega)^\alpha + \varepsilon^\alpha}e^{i\omega t}d\omega \tag{3.42}$$

Note that, for $0 < \alpha < 1$, the complex term $(i\omega)^\alpha + \varepsilon^\alpha = |\omega|^\alpha \exp[i\alpha\,\mathrm{sgn}(\omega)\pi/2] + \varepsilon^\alpha$ has positive real and imaginary parts, i.e., $(i\omega)^\alpha + \varepsilon^\alpha \neq 0$ for any ω. Therefore, the integrand $\mathscr{G}(i\omega)$ has no pole, and thus the residual terms vanish when Cauchy integration theorem is applied to evaluate the integral in Eq.(3.42).

In the case of $t < 0$, one can readily verify $g(t < 0)$ vanishes by virtue of the Jordan's lemma [80], and thus one has $z_\alpha(t < 0) \equiv 0$. This means that the proposed model is indeed causal, and can be realized by using physical systems.

Next, for $t > 0$, the damping kernel function of the proposed model is pursued by deriving the analytical expression of $g(t)$. To this end, letting $i\omega = \lim\limits_{\gamma\to 0^+}(\gamma + i\omega) = \lim\limits_{\gamma\to 0^+} s$, by applying the Cauchy integration theorem, one has

$$\begin{aligned} g(t>0) &= \lim_{\gamma\to 0^+}\frac{1}{2\pi i}\int_{\gamma-i\infty}^{\gamma+i\infty}\frac{s^{\alpha-1}}{s^\alpha+\varepsilon^\alpha}e^{st}ds \\ &= -\frac{1}{2\pi i}\lim_{\gamma\to 0^+}\int_{C_{R1}+l_1+C_\rho+l_2+C_{R2}}\frac{s^{\alpha-1}}{s^\alpha+\varepsilon^\alpha}e^{st}ds \end{aligned} \tag{3.43}$$

where C_{R1} and C_{R2} denote the two large circle arcs with a radius of R, respectively; C_ρ denotes the small circle arc with a radius of ρ; l_1 and l_2 denote the two lips parallel to the negative real axis, as shown in Fig. 3.4.

The integration along the large circle arc vanishes as $R \to \infty$ (by virtue of the Jordan's lemma [80]), and it can also be readily verified that the integration along the small circle arc

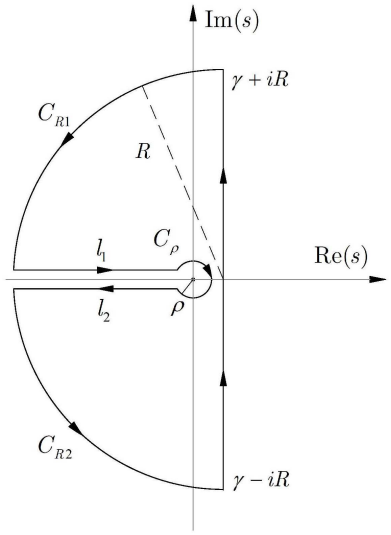

FIGURE 3.4: Integration contour ($t > 0$)

vanishes as $\rho \to 0$. Then, as $\gamma \to 0^+$, calculating the integrations along l_1 and l_2 gives

$$g(t) = \frac{1}{\pi}\int_0^\infty \frac{r^{\alpha-1}\varepsilon^\alpha \sin(\alpha\pi)}{r^{2\alpha} + 2r^\alpha\varepsilon^\alpha\cos(\alpha\pi) + \varepsilon^{2\alpha}} e^{-rt} dr = E_\alpha(-\varepsilon^\alpha t^\alpha) \tag{3.44}$$

for $t > 0$. In the above equation, the latter equality holds because the second term is known as an alternative representation of the Mittag-Leffler relaxation function $E_\alpha(-\varepsilon^\alpha t^\alpha)$ [81]. Therefore, for arbitrary t, one can obtain

$$g(t) = E_\alpha(-\varepsilon^\alpha t^\alpha)u(t) \tag{3.45}$$

Substituting Eq.(3.45) into Eq.(3.41) gives the inverse Fourier transform of the damping function of the proposed model as follows,

$$z_\alpha(t) = \mathscr{F}^{-1}\left[\mathcal{Z}_\alpha(i\omega)\right] = \beta_\alpha \frac{d}{dt}\left\{\left[2E_\alpha(-\varepsilon^\alpha t^\alpha) - 1\right]u(t)\right\} \tag{3.46}$$

Corresponding to Eq.(3.17), the damping kernel function of the proposed model can be obtained as follows,

$$q_\alpha(t) = \mathscr{F}^{-1}\left[\frac{\mathcal{Z}_\alpha(i\omega)}{i\omega}\right] = \beta_\alpha u(t)\left[2E_\alpha(-\varepsilon^\alpha t^\alpha) - 1\right] \tag{3.47}$$

The response force $f_\alpha(t)$ provided by the proposed model is obtained as follows,

$$f_\alpha(t) = k_0\left[x(t) + \eta\, \dot{x}(t) * q_\alpha(t)\right] \tag{3.48}$$

Substituting Eq.(3.47) into the above equation gives

$$f_\alpha(t) = k_0\{(1-\eta\beta_\alpha)x(t) + 2\eta\beta_\alpha \dot{x}(t) * [E_\alpha(-\varepsilon^\alpha t^\alpha)u(t)]\} \tag{3.49}$$

As $\alpha \to 1$, one has $E_\alpha(-\varepsilon^\alpha t^\alpha) = e^{-\varepsilon t}$ and $\beta_\alpha = 1$, thus it follows that

$$f_\alpha(t) = k_0 \left\{(1-\eta)x(t) + 2\eta\dot{x}(t) * \left[e^{-\varepsilon t}u(t)\right]\right\} \tag{3.50}$$

which coincides with the response force provided by the Keivan model. It is worth noting that the negative constant term $-\eta$ in the displacement dependent part correspond to a negative stiffness element used in the physical realization of RILD discussed in Chapter 2.

3.3.3 A mechanical representation

Here, it is assumed there is a physical device that can be modeled by using a fractional order element [53, 54, 82]. Then, a physical realization is derived for the proposed model. To this end, a mechanical system is constructed by arranging a linear spring, negative stiffness, and fractional-order Maxwell elements coupled in parallel, as shown in Fig. 3.5, where k_N and k_α denote the stiffness of the negative stiffness element and that of fractional-order Maxwell element, respectively; $v(t)$ is an internal valuable, denoting the deformation of the fractional-order dashpot. It is worth noting that the damping model consisting of the fractional-order Maxwell element coupled in parallel with a negative stiffness element (thereafter referred to as factional-Maxwell-negative-stiffness (FMNS) model) is a generalization of the MNS model, proposed in Chapter 2.

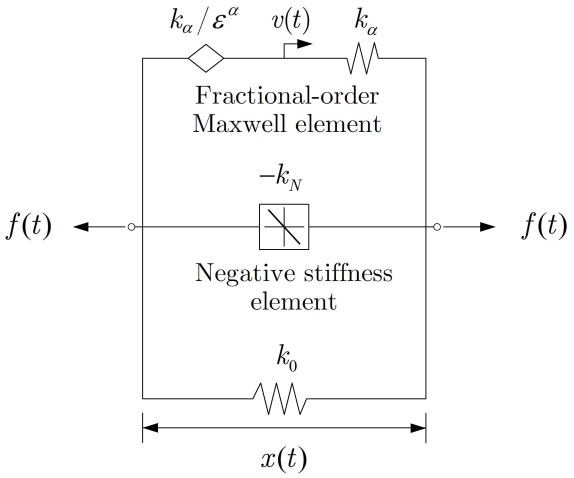

FIGURE 3.5: The proposed RILD model

The fractional-order Maxwell element is represented by a linear spring in series with a fractional-order dashpot. The equation of motion of such a fractional-order element can be expressed as follows,

$$D^\alpha_{0+}v(t) + \varepsilon^\alpha v(t) = \varepsilon^\alpha x(t) \tag{3.51}$$

where $D^\alpha_{0+}v(t)$ denotes an α-order derivative of $v(t)$ with respect to t. Here, the Riemann-Liouville's definition [83] of the fractional derivative is used and defined as follows,

$$D^\alpha_{0+}v(t) := \frac{1}{\Gamma(1-\alpha)}\frac{d}{dt}\int_0^t \frac{v(\tau)}{(t-\tau)^\alpha}d\tau \tag{3.52}$$

where $\Gamma(\cdot)$ is Euler's Gamma function. By using the property of fractional derivative [83], one has

$$\mathscr{F}[D_{0+}^{\alpha} v(t)] = (i\omega)^{\alpha} \mathscr{F}[v(t)] = (i\omega)^{\alpha} V(i\omega) \tag{3.53}$$

Thus, applying Fourier transform to Eq.(3.51) gives

$$V(i\omega) = \frac{\varepsilon^{\alpha}}{(i\omega)^{\alpha} + \varepsilon^{\alpha}} X(i\omega) \tag{3.54}$$

The total response force provided by this mechanical system is written as follows,

$$f(t) = (k_0 - k_N)x(t) + k_{\alpha}[x(t) - v(t)] \tag{3.55}$$

Applying Fourier transform to Eq.(3.55) gives

$$F(i\omega) = (k_0 - k_N)X(i\omega) + k_{\alpha}[X(i\omega) - V(i\omega)] \tag{3.56}$$

With $k_N = \eta\beta_{\alpha}k_0$ and $k_{\alpha} = 2\eta\beta_{\alpha}k_0$, substituting Eq.(3.54) into Eq.(3.56) gives its dynamic stiffness as follows,

$$\mathscr{H}(i\omega) = k_0 \left[1 + \eta\ \beta_{\alpha} \frac{(i\omega)^{\alpha} - \varepsilon^{\alpha}}{(i\omega)^{\alpha} + \varepsilon^{\alpha}}\right] \tag{3.57}$$

which coincides with the dynamic stiffness of the proposed model expressed in Eq.(3.39). This verifies that the proposed model can be represented by this mechanical system, and equivalently, the fractional-order filter can be represented by the FMNS model.

In terms of physical realization of the FMNS model, the negative stiffness element can be conceptually created by equivalently reducing the horizontal stiffness of the primary structure (or of isolators), or physically realized by using some passive negative stiffness devices, as discussed in Chapter 2. With respect to the fractional-order Maxwell element, many engineering solid materials [75, 76] and some damping devices [53, 82] have been reported to be accurately simulated by using fractional-order damping elements. Therefore, a straightforward method of passively realizing the fractional-order Maxwell element is achieved by directly using those damping devices or developing novel damping devices on the basis of the experiments on those solid materials. However, challenges still remains to be overcome in the future in order to develop real-life damping devices designed with desired damping characteristics and apply them in practical engineering projects.

Except for the above method, at present, two types of alternative methods are thought to be promising to physically realize the FMNS model: (i) one may develop a passive system consisting of multiple damping devices, which can be equivalent to the FMNS model in some sense (as to be discussed in next subsection, a modified TMW model is thought to be a viable option), or (ii) one can employ semi-active devices, which can generate the desired damping force by the FMNS model. For this latter, an efficient time-domain analysis technique is required to numerically implement the FMNS model.

3.3.4 Comparison with existing models

For comparison, Table 3.1 summarizes the damping functions and kernel functions of different RILD models introduced above. In the following subsections, the relationships between the proposed and those existing causal RILD models are to be discussed.

TABLE 3.1: Comparison of different RILD elements

Model	Damping function $\mathcal{Z}(i\omega)$	Damping kernel $\mathscr{F}^{-1}[\mathcal{Z}(i\omega)/(i\omega)]$	Causality
Ideal RILD	$i\,\mathrm{sgn}\,(\omega)$	$-\frac{1}{\pi}\ln\lvert t\rvert$	Noncausal
Biot	$\frac{2}{\pi}\ln\left(1+i\frac{\omega}{\varepsilon}\right)$	$-\frac{2u(t)}{\pi}\mathrm{Ei}(-\varepsilon t)$	Causal
Makris	$\frac{2}{\pi}\ln\left\lvert\frac{\omega}{\varepsilon}\right\rvert+i\,\mathrm{sgn}\left(\frac{\omega}{\varepsilon}\right)$	$-\frac{2u(t)}{\pi}\left(\ln\lvert\varepsilon t\rvert+\gamma_0\right)$	Causal
TMW	$\sum_{j=1}^{n}\phi_j\frac{i\omega}{i\omega+r_j}$	$\sum_{j=1}^{n}u(t)\phi_j e^{-r_j t}$	Causal
Keivan	$\frac{i\omega-\varepsilon}{i\omega+\varepsilon}$	$u(t)\left[2e^{-\varepsilon t}-1\right]$	Causal
Proposed	$\beta_\alpha\frac{(i\omega)^\alpha-\varepsilon^\alpha}{(i\omega)^\alpha+\varepsilon^\alpha}$	$\beta_\alpha u(t)\left[2E_\alpha(-\varepsilon^\alpha t^\alpha)-1\right]$	Causal

Generalization of the Makris model

Here, it is proved that the proposed model can include the Makris model as a special case of $\alpha=0$. Recall that $(i\omega)^\alpha=|\omega|^\alpha\left[\cos(\alpha\pi/2)+i\,\mathrm{sgn}(\omega)\sin(\alpha\pi/2)\right]$ and let $\lambda=\omega/\varepsilon$, one can respectively obtain the real and imaginary parts of Eq.(3.38) as follows,

$$\begin{aligned}\mathscr{R}[\mathcal{Z}_\alpha(i\lambda)]&=\cot(\frac{\alpha\pi}{4})\frac{\lambda^{2\alpha}-1}{1+\lambda^{2\alpha}+2|\lambda|^\alpha\cos(\alpha\pi/2)}\\ \mathscr{I}[\mathcal{Z}_\alpha(i\lambda)]&=\cot(\frac{\alpha\pi}{4})\frac{2\mathrm{sgn}(\lambda)|\lambda|^\alpha\sin(\alpha\pi/2)}{1+\lambda^{2\alpha}+2|\lambda|^\alpha\cos(\alpha\pi/2)}\end{aligned}\tag{3.58}$$

which suggest that the real and imaginary parts are even and odd functions with respect to λ (and ω), respectively.

Note that as $\alpha\to0$, one has $1+\lambda^{2\alpha}+2|\lambda|^\alpha\cos(\alpha\pi/2)\to4$, and then it follows that the limit of the real part is

$$\lim_{\alpha\to0}\mathscr{R}[\mathcal{Z}_\alpha(i\lambda)]=\lim_{\alpha\to0}\frac{\lambda^{2\alpha}-1}{4\,\tan(\alpha\pi/4)}=\lim_{\alpha\to0}\frac{\lambda^{2\alpha}-1}{4\,\sin(\alpha\pi/4)}=\lim_{\alpha\to0}\frac{2\ln|\lambda|\lambda^{2\alpha}}{\pi\cos(\alpha\pi/4)}=\frac{2}{\pi}\ln|\lambda|\tag{3.59}$$

where the l'Hôpital's rule is used for the derivation.

With respect to the imaginary part, one has

$$\lim_{\alpha\to0}\mathscr{I}[\mathcal{Z}_\alpha(i\lambda)]=\mathrm{sgn}(\lambda)\lim_{\alpha\to0}\frac{2|\lambda|^\alpha\sin(\alpha\pi/2)}{4\,\tan(\alpha\pi/4)}=\mathrm{sgn}(\lambda)\lim_{\alpha\to0}|\lambda|^\alpha\cos^2(\alpha\pi/4)=\mathrm{sgn}(\lambda)\tag{3.60}$$

Thus, recall that $\lambda = \omega/\varepsilon$, as $\alpha \to 0$, one can obtain

$$\mathcal{Z}_\alpha(i\omega) = \frac{2}{\pi} \ln \left| \frac{\omega}{\varepsilon} \right| + i \operatorname{sgn} \left(\frac{\omega}{\varepsilon} \right) \tag{3.61}$$

which coincides with the damping function of the Makris model, defined in Eq.(3.21). The coincidence between the damping function of the two models in the frequency domain also suggests that the damping kernel function of the proposed model in the case of $\alpha = 0$ can be expressed as Eq.(3.23). Furthermore, because the dynamic stiffness and damping kernel function of the proposed model vary continuously with the value of α, it can also be predicted that the proposed model with a small tunable parameter α (e.g., $\alpha = 0.1$) can provide a good approximation of the Makris model, as least over a frequency range of interest.

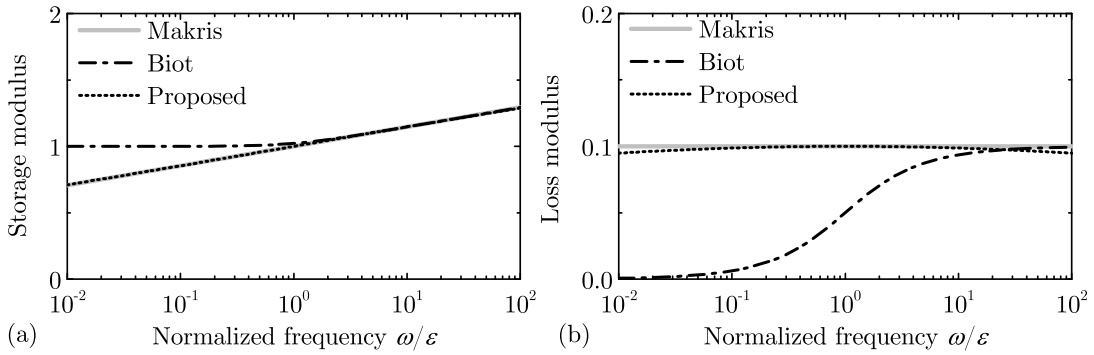

FIGURE 3.6: Comparison between the normalized dynamic stiffnesses of different models for RILD ($\eta = 0.1$)

For example, letting $\eta = 0.1$, Fig. 3.6 compares the normalized dynamic stiffness of the proposed model (e.g., $\alpha = 0.1$) with those of the Makris, and Biot models. It is shown in Fig. 3.6 that the differences between the dynamic stiffness of the proposed model with $\alpha = 0.1$ and that of Makris model are negligible over a frequency range of interest. This means that the proposed model with a small tunable parameter α can be used to approximate the Makris model without significant loss of accuracy. It should be mentioned that in some cases, such an approximation seems to be necessary and useful.

For example, when a mechanical system to physically represent the Makris model is of interest, the one shown in Fig. 3.5 may be alternatively considered by letting $\alpha \to 0$. However, to this end, one needs to let the parameters $k_N = \eta k_0 \cot(\alpha\pi/4)$ and $k_\alpha = 2k_N$ be infinitely large, which may be impossible to be realized in practical applications and also hard to be used for numerical implementations. Instead, the proposed model with a small tunable parameter may be used for approximation, so that those parameters can be designed within a reasonable range. This suggests that compared with the Makris model, the proposed model having an additional tuning parameter α may be more flexible for practical applications.

Relationship with the Biot model

Here, it is first shown that the proposed model is equivalent to a first-order approximation of the Biot model in terms of dynamic stiffness as the tunable parameter α tends to unity (i.e., reducing to the Keivan model). To this end, one can rewrite Eq.(3.14) as follows,

$$\mathcal{Z}_{\mathrm{B}}(i\omega)=\frac{2}{\pi}\ln\left(1+\frac{i\omega}{\varepsilon}\right)=\frac{2}{\pi}\left[\ln 2-\ln\left(1-\frac{i\omega-\varepsilon}{i\omega+\varepsilon}\right)\right] \tag{3.62}$$

By using the Mercator series to expand the last term of the above equation, one can obtain the following expansion

$$\mathcal{Z}_{\mathrm{B}}(i\omega)=\frac{2}{\pi}\left[\ln 2+\sum_{n=1}^{\infty}\frac{1}{n}\left(\frac{i\omega-\varepsilon}{i\omega+\varepsilon}\right)^{n}\right] \tag{3.63}$$

Then, substituting Eq.(3.63) into Eq.(3.13) gives a novel expansion for the dynamic stiffness of the Biot model as follows,

$$\mathscr{H}_{\mathrm{B}}(i\omega)=k_0\left[1+\frac{2\eta}{\pi}\ln 2+\frac{2\eta}{\pi}\sum_{n=1}^{\infty}\frac{1}{n}\left(\frac{i\omega-\varepsilon}{i\omega+\varepsilon}\right)^{n}\right] \tag{3.64}$$

Let $\bar{k}_0=k_0[1+(2\eta\ln 2)/\pi]$ and $\bar{\eta}=2\eta/(\pi+2\eta\ln 2)$, one can rewrite Eq.(3.64) as follows,

$$\mathscr{H}_{\mathrm{B}}(i\omega)=\mathscr{H}_{\mathrm{B}}^{(N)}(i\omega)+\bar{\eta}\,\bar{k}_0\sum_{n=N+1}^{\infty}\frac{1}{n}\left(\frac{i\omega-\varepsilon}{i\omega+\varepsilon}\right)^{n} \tag{3.65}$$

where $\mathscr{H}_{\mathrm{B}}^{(N)}(i\omega)$ is defined as the Nth-order truncated approximation of $\mathscr{H}_{\mathrm{B}}(i\omega)$,

$$\mathscr{H}_{\mathrm{B}}^{(N)}(i\omega)=\bar{k}_0\left[1+\bar{\eta}\sum_{n=1}^{N}\frac{1}{n}\left(\frac{i\omega-\varepsilon}{i\omega+\varepsilon}\right)^{n}\right] \tag{3.66}$$

Letting $N=1$, one has

$$\mathscr{H}_{\mathrm{B}}^{(1)}(i\omega)=\bar{k}_0\left(1+\bar{\eta}\,\frac{i\omega-\varepsilon}{i\omega+\varepsilon}\right) \tag{3.67}$$

which has the same form as the dynamic stiffness of the proposed model expressed in Eq.(3.39) with $\alpha=1$ (i.e., the Keivan model). This means that the Keivan model is actually equivalent to a first-order approximation of the Biot model.

To further investigate the effect of N on the accuracy to approximate the dynamic stiffness of the Biot model, for example, let $\eta=0.1$, Fig. 3.7 compares the Nth-order approximation $\mathscr{H}_{\mathrm{B}}^{(N)}(i\omega)/\bar{k}_0$ with $N=1,10,100$, and ∞, respectively. It is shown in Fig. 3.7 that a first-order approximation exhibits similar characteristics of the dynamic stiffness of Biot model at small values of ω/ε; in order to capture the high-frequency characteristics of the Biot model, a much higher-order approximation is required. Alternatively, the proposed model with a small tunable parameter (e.g., $\alpha=0.1$) may be used, at the expense of distorted low-frequency characteristics.

As mentioned in Section 2, the dynamic stiffness of the Biot model approaches to that of

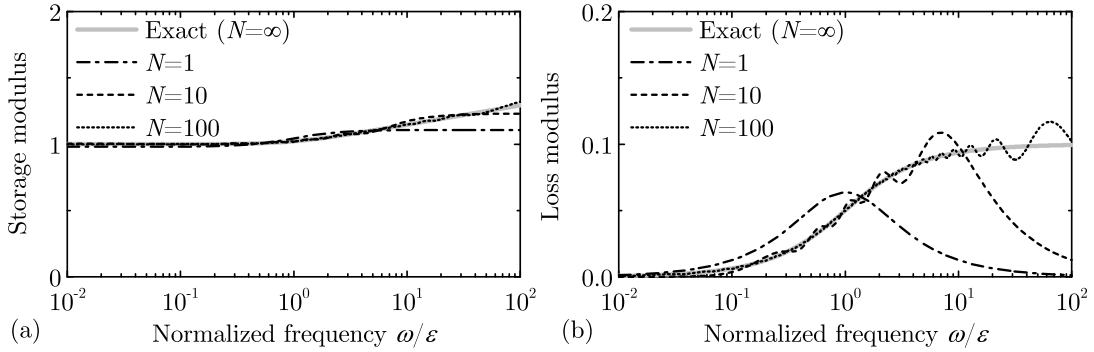

FIGURE 3.7: Approximation of the dynamic stiffness of Biot model by using Mercator series ($\eta = 0.1$)

the Makris model when $\omega \gg \varepsilon$. Thus, from the revealed relation between the proposed and the Makris models, it is implied that the proposed model with a small tunable parameter (e.g., $\alpha = 0.1$) can also be used to approximate the high-frequency characteristics of the Biot model. As shown in Fig. 3.6, the dynamic stiffness of the proposed model approaches to that of the Biot model at large values of ω/ε.

Equivalence to a modified TMW model

Here, it is shown that the proposed model can be equivalent to a TMW model with its storage modulus modified by a rate-independent term, over a frequency range of interest. To this end, quantified comparisons between the TMW and proposed models are made, and the analysis algorithm suggested by Huang et al. [51] is used to determine the tuning parameters of TMW model, ϕ_j, with respect to a given set of $r_j, j = 1, 2, ..., n$, logarithmically spaced over a frequency range from 0.01ε to 100ε. Two values of n are considered: $n = 5$, and $n = 7$, respectively, and the results are shown in Table 3.2.

TABLE 3.2: Characteristic parameters of TMW models

j	$n = 5$		$n = 7$	
	ϕ_j	r_j/ε	ϕ_j	r_j/ε
1	1.676	0.010	1.468	0.010
2	1.473	0.100	0.828	0.046
3	1.449	1.000	1.081	0.215
4	1.473	10.000	0.880	1.000
5	1.676	100.000	1.081	4.642
6	—	—	0.828	21.544
7	—	—	1.468	100.000

In order to approximate the noncausal model represented by Eq.(3.1) at a specified frequency $\omega = \varepsilon$, here, the dynamic stiffness of TMW model is modified as follows,

$$\mathscr{H}'_{\mathrm{T}}(i\omega) = k_0 \left[1 - \eta \mathscr{Z}_{\mathrm{Mod}}(\varepsilon) + \eta \mathscr{Z}_{\mathrm{T}}(i\omega)\right] \tag{3.68}$$

where $Z_{\text{Mod}}(\varepsilon)$ is a rate-independent modification term, i.e.,

$$\mathcal{Z}_{\text{Mod}}(\varepsilon) = \mathscr{R}\left[\mathcal{Z}_{\text{T}}(i\omega)|_{\omega=\varepsilon}\right] = \sum_{j=1}^{n} \frac{\phi_j \varepsilon^2}{\varepsilon^2 + r_j^2} \tag{3.69}$$

The above modification is physically interpreted as connecting the TMW model with a negative stiffness element having a stiffness (absolute value) of $\eta k_0 Z_{\text{Mod}}(\varepsilon)$ in parallel. It should be mentioned that such a modification by adding a rate-independent term to the real part does not affect the causality of the original model. e.g., see [45].

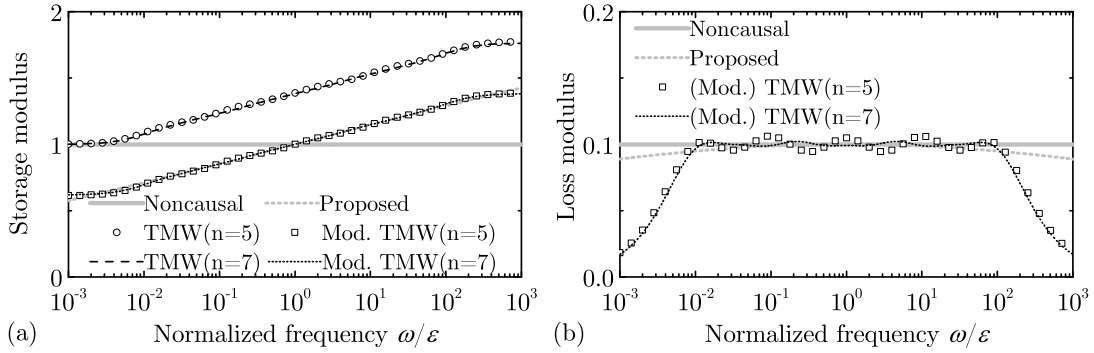

FIGURE 3.8: Comparison between the TMW and proposed models ($\eta = 0.1$)

For example, let $\eta = 0.1$, Fig. 3.8 depicts the dynamic stiffnesses of the original and modified TMW models, as well as those of the noncausal model and proposed model ($\alpha = 0.1$) for comparison. It is shown that as the number n increases, the accuracy of TMW model for approximating the loss modulus of noncausal model increases at the frequency range of investigation. Furthermore, modifying the storage modulus of TMW model to fit the noncausal model at $\omega = \varepsilon$ leads to a good fit to the proposed model all over the frequency range of investigation.

On the one hand, for approximating the behavior of the noncausal model, the modified TMW model can be equivalently represented by the proposed model. Such kind of approximation may be preferable in some applications because much reduced empirical parameters are used for simulations. In this example, for the proposed model, only one additional tuning parameter α is used, whereas $n = 7$ tuning parameters $\phi_j, j = 1, 2, ..., 7$ are used for the (modified) TMW model so that the dynamic stiffness of the TMW is equivalent to that of the proposed model over the frequency range of investigation. This is actually the advantage of a fractional-order operator over integer-order operators used in a constitutive law [75, 76].

On the other hand, it is also suggested that if necessary, one can modify the storage modulus of a TMW model with a rate-independent term of $-\eta k_0 Z_{\text{Mod}}(\varepsilon)$ (i.e., equivalently realized by supplementing a linear negative stiffness element), so that the proposed model can be approximated by using the modified TMW model without compromising the performance. As mentioned in Sub-subsection 3.3.3, in terms of physical implementation of the FMNS model, it may be still challenging to directly develop real-life damping devices, which exhibit exactly the same damping characteristics as the FMNS model does. However,

one may alternatively construct a passive system consisting of multiple available damping devices, which can be equivalent to the FMNS model in some sense. In this regard, the above equivalence suggests that the TMW model can be considered to be a viable option to achieve this goal. A Maxwell element can be readily realized by connecting an oil damper in series with a coil spring, as discussed in Chapter 2. Thus, multiple Maxwell elements can also be readily realized in a similar manner, and then they can be used to construct a TMW model for passively realizing the FMNS model in an equivalent way. Furthermore, this method also enables the development of an efficient analysis algorithm for dynamic analyses of a structural model with RILD, as to be discussed in Chapter 4.

In summary, the relationships between different causal models for RILD are shown in Fig. 3.9. The proposed model can include both the Keivan and Makris models as its special cases with $\alpha = 1$ and $\alpha = 0$, respectively, and the proposed model with a fractional order (e.g., $\alpha = 0.1$) can be equivalent to a (modified) TMW model, which is able to approximate the Biot model for practical applications. In this regard, the proposed model can be considered as a unified causal RILD model. Furthermore, the Keivan model is found to be equivalent to a first-order approximation of the Biot model. These newly revealed relationships between different models, along with the established ones, enable the development of a unified framework of causal RILD models, as shown in Fig. 3.9.

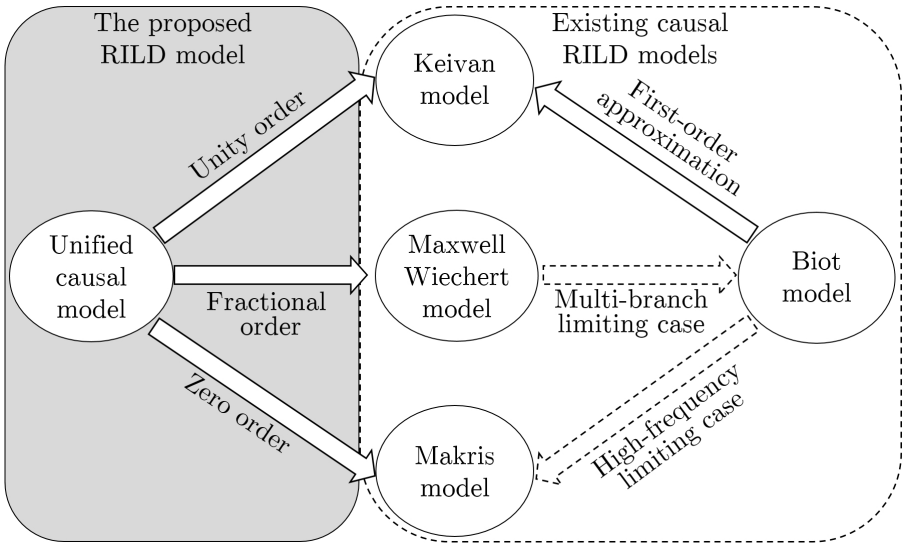

FIGURE 3.9: A unified framework of causal RILD models (dashed arrows indicate the established relations, solid ones indicate those revealed here)

3.4 An L1-algorithm-based internal variable method

In this section, for numerical implementation of the proposed RILD element (i.e., the FMNS model) in the time domain, a dynamic analysis method is developed by directly calculating the fractional derivative on the basis of the so-called L1-algorithm [55].

3.4.1 Governing equation of motion

First, one considers a linear single-degree-of-freedom (SDF) system incorporated with the FMNS model, as shown in Fig. 3.10, where $p(t)$ denotes the exciting force. The governing equation of motion of such a system is expressed as follows,

$$m\ddot{x}(t)+(k_0+k_\alpha-k_N)x(t)-k_\alpha v(t)=p(t) \tag{3.70}$$

where $v(t)$ denotes the deformation of the fractional-order dashpot, which is coupled with the displacement of the mass $x(t)$ by the following equation:

$$D^\alpha_{0+}v(t)+\varepsilon^\alpha v(t)=\varepsilon^\alpha x(t) \tag{3.71}$$

For the above system, one can carry out dynamic analysis by using frequency-domain response analysis method by virtue of fast Fourier transform (FFT) algorithm. However, time-domain methods may be preferred in some cases, e.g., where nonlinearities of the structural components and/or supplemental energy dissipation devices are involved.

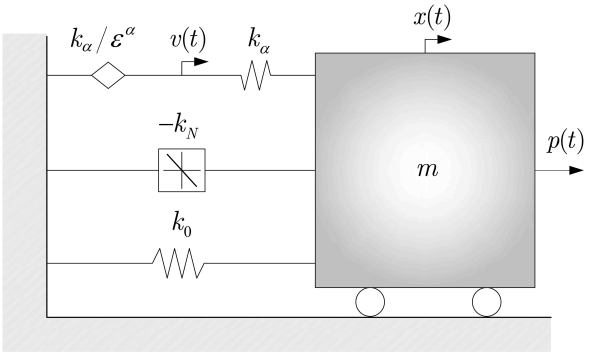

FIGURE 3.10: A linear SDF system incorporated with the FMNS model

Here, a time-domain technique for dynamic analysis of the above system is developed by directly evaluating Riemann-Liouville's type of fractional derivative on the basis of the so-called L1-algorithm [55]. To this end, the definition given in Eq.(3.52) is equivalently expressed as follows [55],

$$D^\alpha_{0+}v(t)=\frac{1}{\Gamma(1-\alpha)}\left[\frac{v(0)}{t^\alpha}+\int_0^t\frac{1}{\tau^\alpha}\frac{dv(t-\tau)}{d\tau}d\tau\right] \tag{3.72}$$

Letting the time axis be divided into N subintervals with equal length $h=t/n$ and $t=t_n=nh$ $(1\le n\le N=t_{\max}/h)$, the above equation can be expressed as follows,

$$D^\alpha_{0+}v(t_n)\approx\frac{1}{\Gamma(1-\alpha)}\left[\frac{v(0)}{(nh)^\alpha}+\sum_{j=1}^{n}\int_{(j-1)h}^{jh}\frac{dv(t-\tau)}{\tau^\alpha d\tau}d\tau\right] \tag{3.73}$$

Approximating the integral over the j-th subinterval as follows,

$$\int_{(j-1)h}^{jh} \frac{dv(t-\tau)}{\tau^{\alpha} d\tau} d\tau \approx \frac{v(t_{n-j+1}) - v(t_{n-j})}{h^{\alpha}(1-\alpha)} \left[j^{1-\alpha} - (j-1)^{1-\alpha} \right] \tag{3.74}$$

With $\Gamma(2-\alpha) = (1-\alpha)\Gamma(1-\alpha)$, one can numerically evaluate the fractional derivative as follows,

$$D_{0+}^{\alpha} v(t_n) \approx \frac{1}{\Gamma(2-\alpha)h^{\alpha}} \sum_{j=0}^{n} \bar{w}_j v(t_{n-j}) \tag{3.75}$$

where $\bar{w}_j$ is a weighting factor independent on the function $v(t)$, with $\bar{w}_0 = 1$ and

$$\bar{w}_j = \begin{cases} (j+1)^{1-\alpha} - 2j^{1-\alpha} + (j-1)^{1-\alpha}, & j = 1, 2, ..., n-1; \\ (1-\alpha)j^{-\alpha} - j^{1-\alpha} + (j-1)^{1-\alpha}, & j = n. \end{cases}$$

Recall that $k_N = \eta\beta_{\alpha}k_0$ and $k_{\alpha} = 2\eta\beta_{\alpha}k_0$, letting $x(t_n) = x(t)$, and then substituting Eq.(3.75) into Eq.(3.71) gives the relationship between $v(t_n)$ and $x(t_n)$ as follows,

$$v(t_n) = \frac{\psi}{1+\psi} x(t_n) - \frac{1}{1+\psi} q(t_{n-1}) \tag{3.76}$$

where $\psi = \varepsilon^{\alpha} h^{\alpha} \Gamma(2-\alpha)$ and $q(t_{n-1}) = \sum_{j=1}^{n} \bar{w}_j v(t_{n-j})$. Assuming the values of $v(t)$ at the past $(n-1)$ steps are known so that $q(t_{n-1})$ is given, and $v(t_n)$ is explicitly related with $x(t_n)$ by Eq.(3.76). Substituting Eq.(3.76) into Eq.(3.75) gives

$$D_{0+}^{\alpha} v(t_n) \approx \frac{\varepsilon^{\alpha}}{1+\psi} \left[x(t_n) + q(t_{n-1}) \right] \tag{3.77}$$

By using Eq.(3.76), Eq.(3.70) is rewritten as follows,

$$m\ddot{x}(t_n) + (k_0 + k'_{\alpha} - k_N) x(t_n) = p(t_n) - k'_{\alpha} q(t_{n-1}) \tag{3.78}$$

where $k'_{\alpha} = k_{\alpha}/(1+\psi)$. The above equation can be readily solved by using established numerical integration schemes, e.g., the Newmark integration scheme.

It should be mentioned that time-domain techniques are available for dynamic analyses of structural systems incorporated with fractional-order elements [53, 54, 82]. In the pioneering work done by Koh and Kelly [82], the L1-algorithm is employed for dynamic analysis of an oscillator consisting of a mass and a fractional-order Kelvin element, which is used to simulate elastomeric bearings for base isolation systems. In references [53, 54], a Gl-algorithm is used for dynamic analyzing a structure equipped with a fractional-order Maxwell element.

3.4.2 Acceleration of the computation

Generally speaking, both the L1- and G1-algorithms result in a computational complex of $O(N^2)$ for dynamic analyses of fractional-order systems. However, the computational complex can be reduced to $O(N)$ if the fixed memory principle [84] is employed for the evaluation of fractional derivative, i.e.,

$$D_{0+}^{\alpha} v(n) \approx \frac{1}{\Gamma(2-\alpha)h^{\alpha}} \sum_{j=0}^{N_0} \bar{w}_j v(n-j) \tag{3.79}$$

where $v(n) = 0$ is assumed for $n = -N_0, -N_0 - 1, ..., -1$, due to the causality; N_0 is a cutoff number, indicating the length of a fixed memory. This principle is used because of the fading memory property of the kernel of the fractional convolution integral. For its application, one can simply update $q(t_{n-1})$ in Eq.(3.78) as $\bar{q}(t_{n-1}) = \sum_{j=1}^{N_0} \bar{w}_j v(t_{n-j})$.

It is also useful to realize the approximation in Eq.(3.79) by constructing a length-N_0 finite-duration impulse response (FIR) filter as follows,

$$Z^{1}(i\omega) = \frac{1}{\Gamma(2-\alpha)h^{\alpha}} \sum_{j=0}^{N_0} \bar{w}_j e^{-i\omega \cdot jh} \tag{3.80}$$

which is used to approximate a fractional derivative operator in the frequency domain

$$Z^{1}(i\omega) \approx \frac{\mathscr{F}[D_{0+}^{\alpha} v(t)]}{\mathscr{F}[v(t)]} = (i\omega)^{\alpha} \tag{3.81}$$

By using the designed FIR filter, one can recover the damping function of the FMNS model as follows,

$$Z_{\alpha}^{1}(i\omega) \approx \beta_{\alpha} \frac{Z^{1}(i\omega) - \varepsilon^{\alpha}}{Z^{1}(i\omega) + \varepsilon^{\alpha}} \tag{3.82}$$

where the superscript '1' denotes the damping function recovered from the approximation of the L1 algorithm.

For example, letting $\alpha = 0.1$, Fig. 3.11 compares the recovered damping function from the above approximation with the exact damping function of the FMNS model. It is shown that a high-order FIR filter can be used to improve the approximation of the damping function in low frequency range (e.g., $\omega/\varepsilon \leq 1$), whereas has limited effect in the high frequency range (e.g., $\omega/\varepsilon \geq 10$). Moreover, with $N_0 = 0.1N$, the recovered damping function from the FIR filter well approximates that of the exact one over the frequency range $0.1 \leq \omega/\varepsilon \leq 100$ (provided that ε = structural fundamental frequency, such a frequency range may cover the dominant frequency ranges of most ground motions). This suggests that for the time-domain implementation of the FMNS model, one can use an FIR filter with a length of $N_0 = 0.1N$ to approximate the fractional derivative operator so that the computational complexity can be reduced from $O(N^2)$ to $O(N)$ without significantly compromising the simulation accuracy.

Indeed, some attempts [85–87] have been made to permit the variation of the step length.

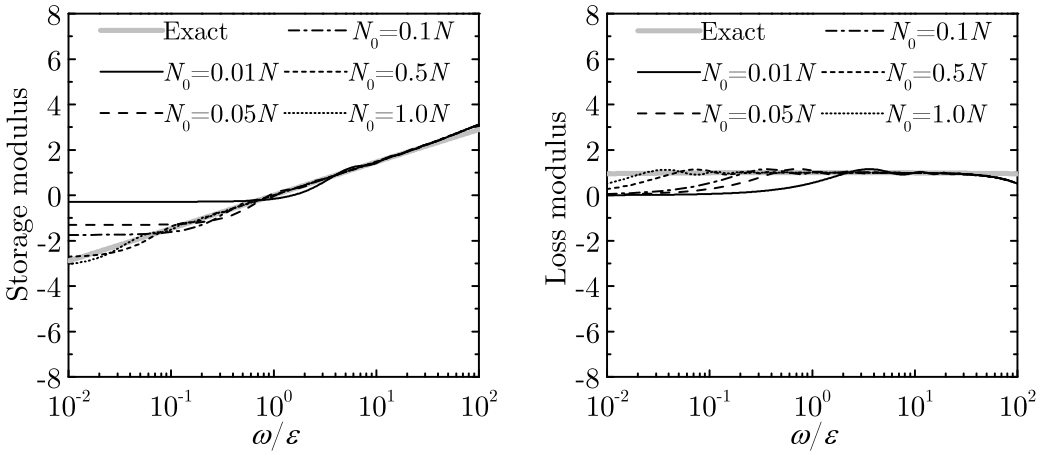

FIGURE 3.11: Recovered damping function in terms of (left) storage modulus and (right) loss modulus.

For example, instead of the fixed memory principle, Ford and Simpson [86] suggested a logarithmic memory principle to acceleration the calculation of fractional derivative, so that the order in accuracy of the quadrature method can be preserved at a reasonable computational cost. More recently, it is worth noting that some spectral methods [88–91] have been suggested to numerically solve the fractional derivative equation, so that computationally efficient and spectrally convergent algorithms can be developed. However, these methods are thought to be relatively complicated for applications in structural dynamic simulation problems. Study on how to embed these computationally efficient and high-order (in accuracy) methods into the established numerical integration schemes (e.g., Newmark integration scheme) is one of the future topics.

3.4.3 Computational speed and accuracy

Here, the applicability of the L1-algorithm-based internal method for the structural dynamic analysis is discussed in terms of both computational speed and accuracy. For this purpose, an SDF system ($T_0 = 4.0$ s, and $\eta = 0.1$) is first considered as an analytical example. Time history analyses are conducted by using the El Centro wave recorded in the 1940 Imperial Valley Earthquake with a fixed step length of 0.002 second.

Fig. 3.12 compares the recorded times of central processing unit (CPU) taken by the developed method with respect to different cutoff numbers (left) and tunable parameters (right), respectively. It is shown that a small cutoff number (e.g., $N_0/N \leq 0.1$) results in significant reduction on the computational cost, whereas the tunable parameter α has limited effect on the computational cost.

Fig. 3.13 compares the percentage errors of the developed method in terms of the displacement peak values (left) and root-mean-square (RMS) values (right), compared to the case of $N_0 = N$ (full memory principle). It is shown that the percentage errors in terms of displacement peak value and RMS value can both be reduced to negligible levels if

$N_0/N \geq 0.1$. This is in good agreement with the prediction from the comparison studies made in the frequency domain, as shown in Fig. 3.11.

Furthermore, letting $\alpha = 0.1$, Fig. 3.14 compares the percentage errors of the fixed memory principle with respect to the variation of structural period T_0 in terms of the displacement peak values (left) and RMS values (right), compared to the case of $N_0 = N$. It is shown that in all cases, the percentage errors in terms of displacement peak value and RMS value can both be reduced to negligible levels if $N_0/N \geq 0.1$. Therefore, in the following comparison studies, $N_0 = 0.1N$ is used to apply the above method for structural dynamic analyses if no specification is given.

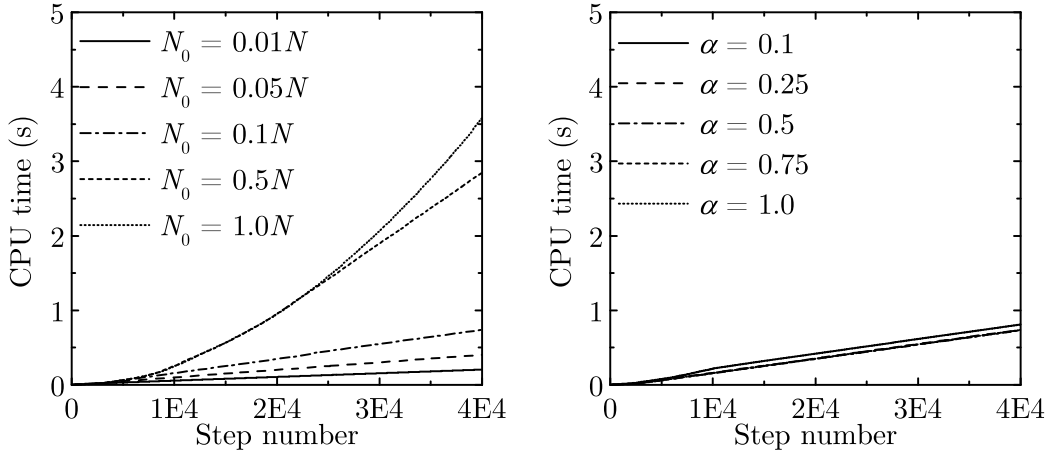

FIGURE 3.12: Computational cost with respect to the variations of (left) cutoff number ($\alpha = 0.1$) and (right) tunable parameter ($N_0 = 0.1N$).

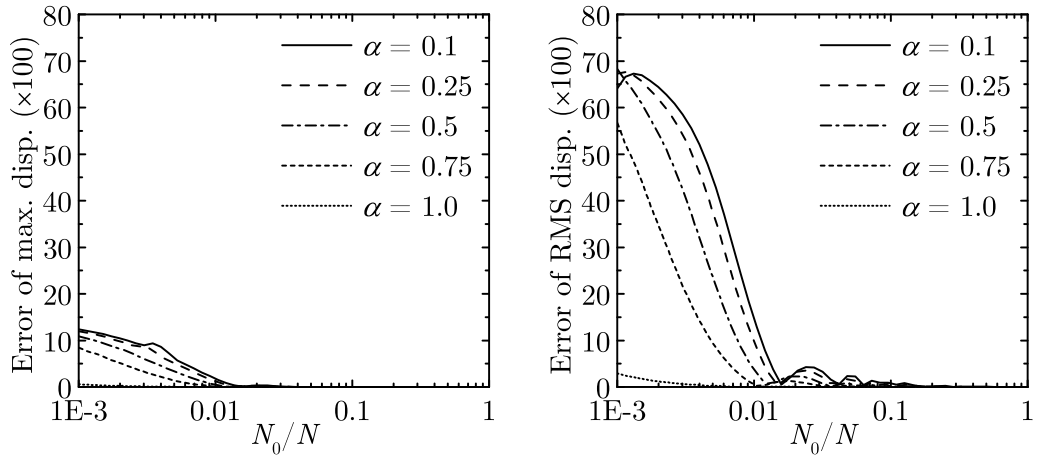

FIGURE 3.13: Percentage error in terms of displacement (left) peak value and (right) RMS value with respect to the variation of the tunable parameter.

The above parametric studies suggest that although the conventional L1-algorithm-based internal variable method has a computational complex of order $O(N^2)$, the fixed memory

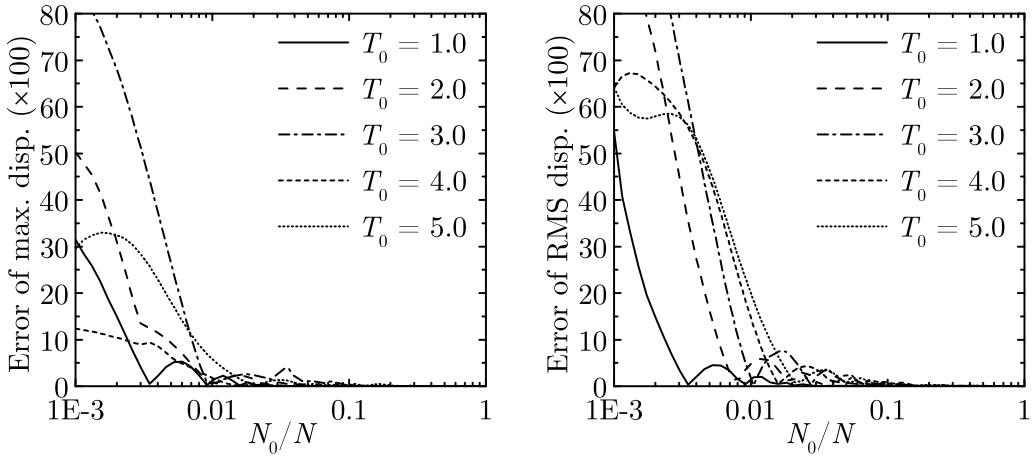

FIGURE 3.14: Percentage error in terms of displacement (left) peak value and (right) RMS value with respect to the variation of structural period T_0.

principle can be used to significantly reduce the computational cost (resulting in a computational complex of order $O(N)$) without compromising the simulation accuracy, and consequently it can be used as a computationally efficient tool for the dynamic analysis of structure with RILD.

3.4.4 Extension to MDF structural systems

Here, the developed time-domain analysis method is extended to an MDF structural model incorporated with the FMNS model. Here, for brevity, a two-degree-of-freedom structural model is considered, and the governing equation of motion is expressed in matrix as follows,

$$\mathbf{m}\ddot{\mathbf{x}}(t_n) + (\mathbf{k} + \mathbf{k}'_\alpha - \mathbf{k}_N)\mathbf{x}(t_n) = \mathbf{p}(t_n) - \mathbf{k}_q\bar{\mathbf{q}}(t_{n-1}) \tag{3.83}$$

where $\mathbf{m}$ and $\mathbf{k}$ denote the mass and primary stiffness matrices, respectively; $\mathbf{k}'_\alpha$ and $\mathbf{k}_N$ denote additional stiffness matrices from the fractional-order Maxwell and negative stiffness elements, respectively; $\mathbf{x}(t_n)$ and $\mathbf{p}(t_n)$ denote the response displacement and exciting force vectors at the n-th time step, respectively; $\bar{\mathbf{q}}(t_{n-1}) = \sum_{j=1}^{N_0} \bar{w}_j \mathbf{v}(t_{n-j})$, where $\mathbf{v}(t_n)$ denote the deformation vector of the dashpots at the n-th time step. Those matrices and vectors are respectively expressed as follows,

$$\mathbf{m} = \begin{bmatrix} m_1 & \\ & m_2 \end{bmatrix}, \mathbf{k} = \begin{bmatrix} k_1 + k_2 & -k_2 \\ -k_2 & k_2 \end{bmatrix}, \mathbf{k}'_\alpha = \begin{bmatrix} {}_1k'_\alpha + {}_2k'_\alpha & -{}_2k'_\alpha \\ -{}_2k'_\alpha & {}_2k'_\alpha \end{bmatrix},$$

$$\mathbf{k}_q = \begin{bmatrix} {}_1k'_\alpha & -{}_2k'_\alpha \\ & {}_2k'_\alpha \end{bmatrix}, \mathbf{k}_N = \begin{bmatrix} {}_1k_N + {}_2k_N & -{}_2k_N \\ -{}_2k_N & {}_2k_N \end{bmatrix}, \mathbf{x} = \begin{Bmatrix} x_1 \\ x_2 \end{Bmatrix}, \mathbf{p} = \begin{Bmatrix} p_1 \\ p_2 \end{Bmatrix}.$$

Alternatively, Eq.(3.83) can also be expressed in the following form

$$\mathbf{m}\ddot{\mathbf{x}}(t_n) + \mathbf{k}\mathbf{x}(t_n) + \mathbf{f}_f(t_n) = \mathbf{p}(t_n) \tag{3.84}$$

where $\mathbf{f}_f(t_n)$ denotes the damping force provided by the FMNS models at the n-th time step, which can be expressed as follows,

$$\mathbf{f}_f(t_n) = (\mathbf{k}'_\alpha - \mathbf{k}_N)\mathbf{x}(t_n) + \mathbf{k}_q\bar{\mathbf{q}}(t_{n-1}) \tag{3.85}$$

Assume that the relaxation parameter, the tunable parameter, and loss factor of the FMNS model for each degree of freedom are fixed, respectively, i.e. $\varepsilon_j = \varepsilon$, $\alpha_j = \alpha$, and $\eta_j = \eta$, $j = 1, 2$, so that the auxiliary quantities $\psi_j = \psi = \varepsilon^\alpha h^\alpha \Gamma(2-\alpha)$, $j = 1, 2$, for each degree of freedom are equal. By letting ${}_jk_N = \eta\beta_\alpha \cdot k_j$ and ${}_jk'_\alpha = 2 \cdot {}_jk_N/(1+\psi)$, one can simplify Eq.(3.83) as follows,

$$\mathbf{m}\ddot{\mathbf{x}}(t_n) + (1+\eta_e)\mathbf{k}\mathbf{x}(t_n) = \mathbf{p}(t_n) - \mathbf{k}_q\mathbf{q}(t_{n-1}) \tag{3.86}$$

where $\eta_e = \eta\beta_\alpha(1-\psi)/(1+\psi)$.

It should be noted that Eq.(3.83) can be readily solved by using established numerical integration schemes. For example, the established Newmark's method [7] can be readily used to solve Eq.(3.83), and thus response history analysis of such an MDF structural system can be carried out with minor modification on the conventional procedures. For convenience of application, Table 3.3 summarizes the main procedures for response history analyses of a linear MDF structural system incorporated with the FMNS models. When nonlinearities of structural components or supplemental energy dissipation devices are involved, one can readily combine the Newton-Raphson iterative method with the developed method for nonlinear response history analyses.

3.5 Application into a base-isolated structure

Here, the application of the FMNS model for mimicking the behavior of ideal RILD is discussed when it is supplemented into a base-isolated structure for providing additional damping to constraint the isolator displacement.

To this end, a benchmark base-isolated five-story shear building model is used as an analytical example for response history analyses, as shown in Fig. 3.15. Table 3.4 lists the structural specifications. The fundamental natural period and the inherent damping ratio of the first mode of the upper structure with a fixed base are approximately 0.67 s and 2%, respectively. The damping matrix of the upper structure is assumed to be proportional to the stiffness matrix. The natural rubber bearings are designed to have the isolation period of 4.0 s. However, the inherent damping of the isolators is neglected (i.e., $c_0 = 0$).

For providing supplemental damping to constraint the isolator displacement, a hysteretic damper (HD) and a RILD element are simultaneously incorporated into the isolation layer, as shown in Fig. 3.15. Letting the yielding deformation be assumed as 0.035 m, and μ denote the ratio of yielding force to the total weight of the structural system (including the base weight).

TABLE 3.3: Newmark's method modified for an MDF structure incorporated with the FMNS model

1.0 *Initial calculations*

1.1 Assume ε_j, α_j, and η_j, $j = 1, 2, ..., l$.

1.2 Select h and N_0.

1.3 Determine $\psi_j = \varepsilon_j^{\alpha_j} \cdot h^{\alpha_j} \cdot \Gamma(2-\alpha_j)$; ${}_jk_N = \eta_j \cdot \beta_{\alpha_j} \cdot k_j$; ${}_jk_\alpha = 2 \cdot {}_jk_N$; and ${}_jk'_\alpha = \dfrac{{}_jk_\alpha}{1+\psi_j}$, $j = 1, 2, ..., l$.

1.4 Assemble matrices $\mathbf{m}$, $\mathbf{k}$, $\mathbf{k}_\alpha$, $\mathbf{k}_N$, $\mathbf{k}_q$.

1.5 Solve $\mathbf{p}_0 - \mathbf{k}_q\bar{\mathbf{q}}_0 - (\mathbf{k} + \mathbf{k}'_\alpha - \mathbf{k}_N)\mathbf{x}_0 = \mathbf{m}\ddot{\mathbf{x}}_0 \Rightarrow \ddot{\mathbf{x}}_0$.

1.6 $\mathbf{a}_1 = \dfrac{1}{\beta h^2}\mathbf{m}$; $\mathbf{a}_2 = \dfrac{1}{\beta h}\mathbf{m}$; and $\mathbf{a}_3 = (\dfrac{1}{2\beta} - 1)\mathbf{m}$.

1.7 $\bar{\mathbf{k}} = \mathbf{a}_1 + \mathbf{k} + \mathbf{k}'_\alpha - \mathbf{k}_N$.

2.0 *Calculations for each time step*, $n = 0, 1, 2, ...$

2.1 $\bar{w}_j = (j+1)^{1-\alpha} - 2j^{1-\alpha} + (j-1)^{1-\alpha}$, if $j = 1, 2, ..., n$; $\bar{w}_j = (1-\alpha)(n+1)^{-\alpha} - (n+1)^{1-\alpha} + n^{1-\alpha}$, if $j = n+1$.

2.2 $\bar{\mathbf{q}}_n = \sum_{j=1}^{N_0} \bar{w}_j \mathbf{v}_{n+1-j}$.

2.3 $\bar{\mathbf{p}}_{n+1} = \mathbf{p}_{n+1} + \mathbf{a}_1\mathbf{x}_n + \mathbf{a}_2\dot{\mathbf{x}}_n + \mathbf{a}_3\ddot{\mathbf{x}}_n - \mathbf{k}'_\alpha\bar{\mathbf{q}}_n$.

2.4 Solve $\bar{\mathbf{k}}\,\mathbf{x}_{n+1} = \bar{\mathbf{p}}_{n+1} \Rightarrow \mathbf{x}_{n+1}$.

2.5 $\dot{\mathbf{x}}_{n+1} = \dfrac{\gamma}{\beta h}(\mathbf{x}_{n+1} - \mathbf{x}_n) + \left(1 - \dfrac{\gamma}{\beta}\right)\dot{\mathbf{x}}_n + \left(1 - \dfrac{\gamma}{2\beta}\right)h\ddot{\mathbf{x}}_n$.

2.6 $\ddot{\mathbf{x}}_{n+1} = \dfrac{1}{\beta h^2}(\mathbf{x}_{n+1} - \mathbf{x}_n) - \dfrac{1}{\beta h}\dot{\mathbf{x}}_n + \left(1 - \dfrac{1}{2\beta}\right)\ddot{\mathbf{x}}_n$.

2.7 $\mathbf{v}_{n+1} = \dfrac{\psi}{1+\psi}\mathbf{x}_{n+1} - \dfrac{1}{1+\psi}\bar{\mathbf{q}}_n$.

3.0 *Repetition for the next time step.* Replace n by $n+1$ and implement steps 2.1 to 2.7 for the next time step.

3.5.1 Linear response history analyses

In order to verify the applicability of the FMNS model to causally approximate the behavior of ideal RILD, three different types of elements are considered for comparison, as shown in Table 3.5. Letting $\mu = 0$ (so that the structural system remains linearly elastic), the response history analysis of the base-isolated structure incorporated with RILD can be readily conducted by using frequency response analysis method with the entire time history of input ground motion provided. For the modified TMW element, available formulations for time-domain dynamic analyses can be found in references [33, 46]. For the FMNS model, letting $\alpha = 0.1$, the time-domain technique developed in the above section is employed for response history analyses.

For example, Fig. 3.16 compares the response histories of the example structure separately incorporated with different models when the system is subjected to the ground motion recorded at the El Centro station in the 1940 Imperial Valley earthquake (Peak ground acceleration (PGA) = 3.417 m/s^2, N–S component). Furthermore, Fig. 3.17 compares the hysteresis loops of different damping models. This example verifies that the FMNS model

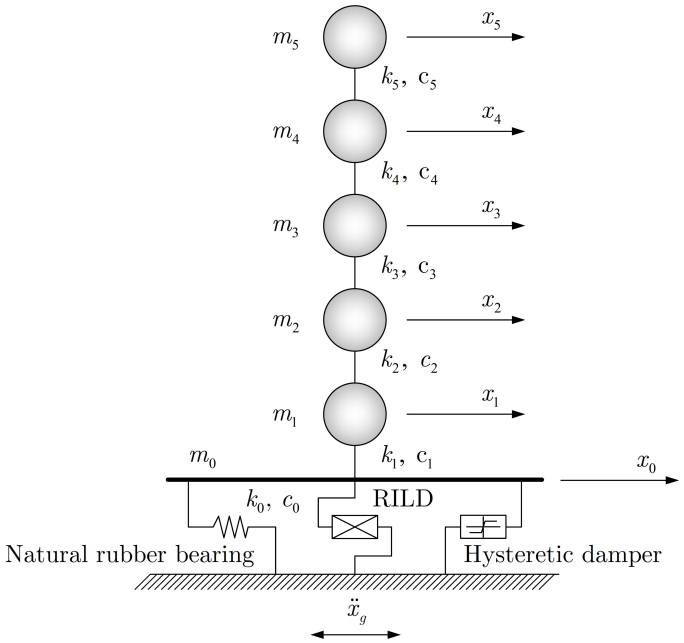

FIGURE 3.15: A base-isolated structure incorporated with RILD

TABLE 3.4: Structural properties of the analytical model

j	Mass m_j (ton)	Stiffness k_j (kN/m)	Damping c_j (kN·s/m)	Height (m)
5	1 739	2 291 000	9 770	3.8
4	1 800	2 488 000	10 610	3.8
3	1 807	1 939 000	8 270	4.4
2	1 928	2 038 000	8 690	4.4
1	2 335	1 760 000	7 510	5.45
0	3 057	31 250	—	2.73

TABLE 3.5: Different rate-independently damping elements

No.	Damping	Loss factor	Parameters
1	Ideal RILD	$\eta = 0.4$	$k_c = i\,\eta\,k_0 \mathrm{sgn}(\omega)$
2	Modified TMW	$\eta = 0.4$	$k'_{c,\mathrm{TMW}} = \eta\,k_0 \sum_{n=1}^{7} \phi_n \left(\frac{i\omega}{i\omega + r_n} - \frac{\varepsilon^2}{\varepsilon^2 + r_n^2} \right)$
3	FMNS	$\eta = 0.4$	$k_{c,\mathrm{P}} = \eta\,k_0 \cdot \beta_\alpha \frac{(i\omega)^\alpha - \varepsilon^\alpha}{(i\omega)^\alpha + \varepsilon^\alpha}$

(with $\alpha = 0.1$) performs similarly to the modified TMW model, in consistence with the prediction from the frequency-domain comparison in Fig. 3.8, and and both of the two models can be used to causally approximate ideal RILD without significant loss of accuracy.

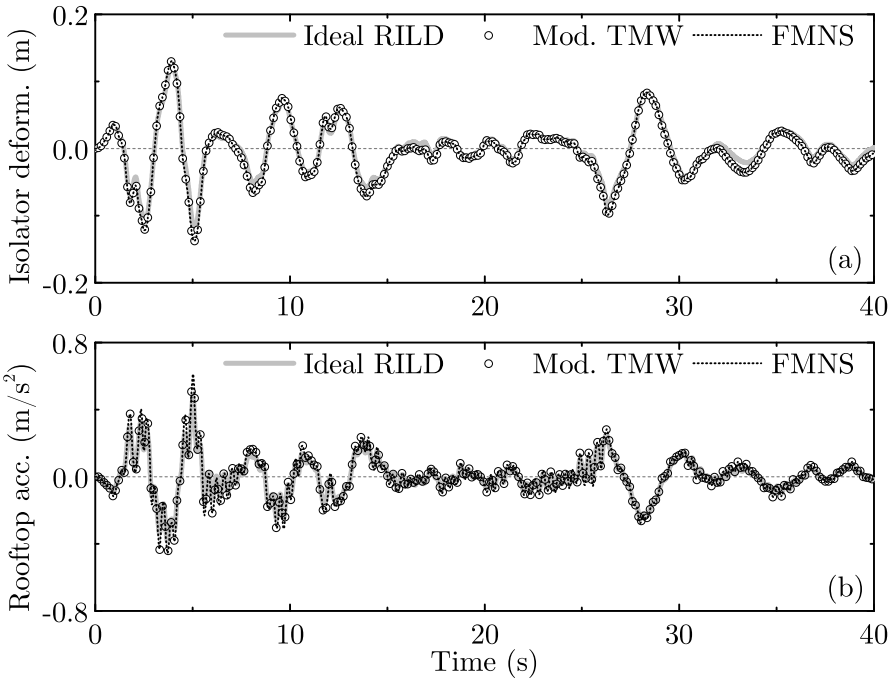

FIGURE 3.16: Response histories of linear base-isolated structural systems incorporated with different models (1940 El Centro)

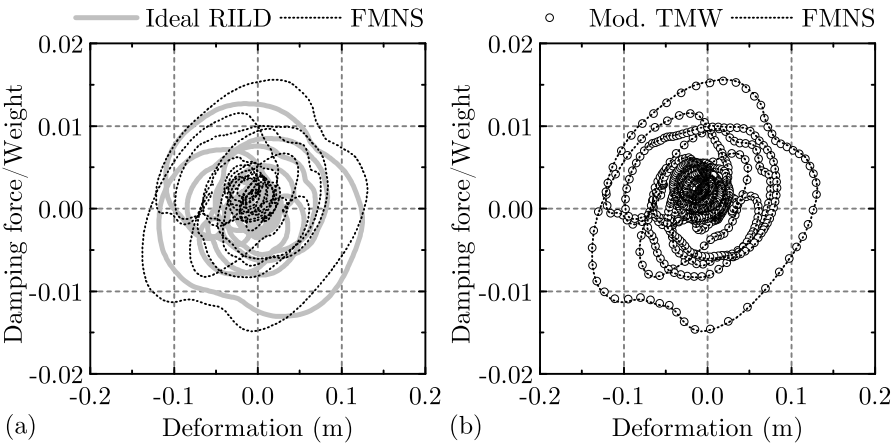

FIGURE 3.17: Hysteresis loops of different RILD elements (1940 El Centro)

3.5.2 Nonlinear response history analyses

It is established that due to its noncausality, the ideal RILD element is difficult to be used for dynamic analyses when structural components and/or supplemental energy dissipation devices yield and exhibit strong nonlinear behavior. In such cases, the FMNS model may be used instead to provide a causal approximation.

In order to verify the effectiveness of the developed time-domain method for nonlinear dynamic analyses, the base-isolated structure simultaneously incorporated with the FMNS model and an HD is used as an analytical example. Besides its dissipation capability, an HD is also used in base-isolated structures to provide sufficient initial stiffness to resist wind

loads. Following the standard practice in Japan, the HD should be designed not to yield against the wind load of a 500-years return period. For satisfying this demand, the HD is designed with a yielding force of 4 011 kN, and the ratio of HD yielding force to the total weight is $\mu = 3.2\%$.

Two different cases are considered for nonlinear time history analyses, as shown in Table 3.6. In case 1, the FMNS model with $\alpha = 1.0$ is used to represent Keivan RILD element (MNS model), whereas in case II, the FMNS model with $\alpha = 0.1$ is used to approximate a causal RILD element in the Makris model (or the modified TMW model). Such a combined damping system consisting of a RILD element and an HD may be used to constraint the excessive isolator deformations induced by those ground motion records with large amplitudes. For example, Fig. 3.18 shows the response histories of the example structure subjected to a ground motion recorded at the Sylmar County Hospital station in the 1994 Northridge earthquake (PGA = 8.26 m/s^2, N–S component).

TABLE 3.6: Two cases for nonlinear time history analyses

Case	Tuning parameter	Loss factor	HD yielding force/total weight
I	$\alpha = 1.0$	$\eta = 0.4$	$\mu = 3.2\%$
II	$\alpha = 0.1$	$\eta = 0.4$	$\mu = 3.2\%$

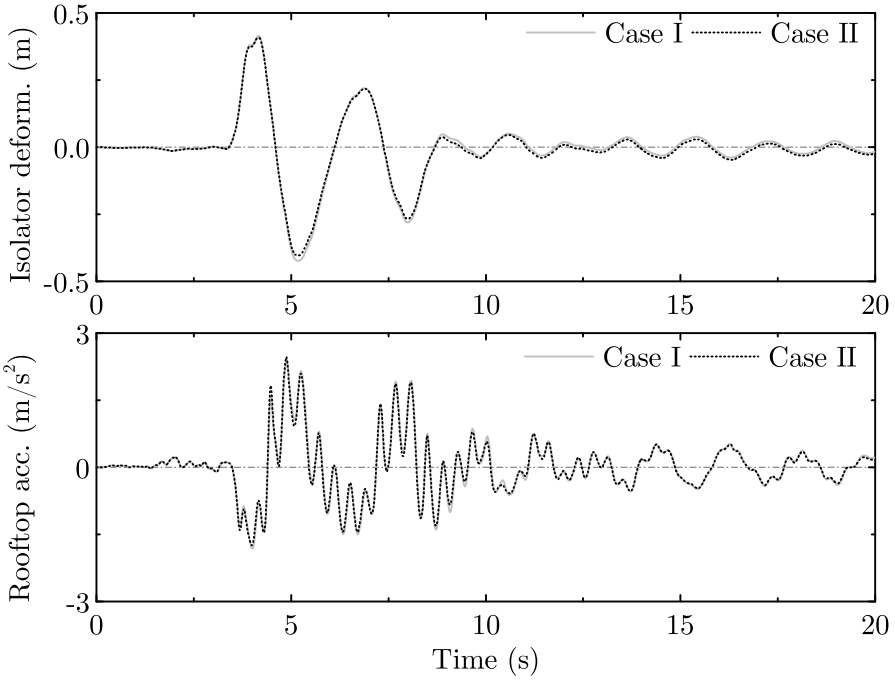

FIGURE 3.18: Seismic responses of a base-isolated structure incorporated with the FMNS model and hysteretic damper (1995 Sylmar County Hospital)

It is observed from Fig. 3.18 that the differences between the seismic responses of the example structure in the two cases are negligible. This occurs because the hysteresis loops of

the damping elements are similar in the two cases, as shown in Fig. 3.19. This example verifies that by using the developed time-domain method, the FMNS model can be numerically implemented in nonlinear dynamic analyses, which is hard for the ideal RILD element. Furthermore, it is shown in Fig. 3.19(a) that when incorporated into a base-isolated structure, the MNS model can behave similarly to the FMNS model with a fractional tunable parameter, whereas the former is much simpler in the senses of both numerical implementation and physical realization. This quantitative comparison suggests that the MNS model can be used as a simple option to causally approximate the behavior of RILD for application into a nonlinear base-isolation system without significantly compromising the structural seismic performance, when compared with other more complicated models for RILD.

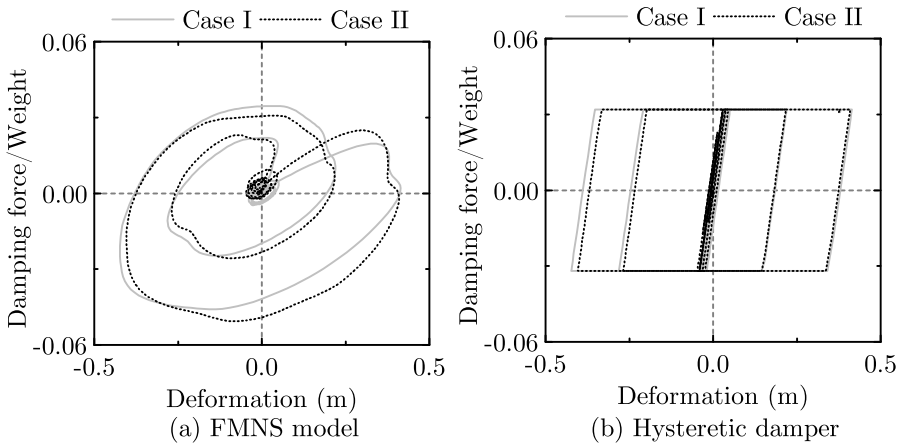

FIGURE 3.19: Hysteresis loops of different damping elements (1995 Sylmar County Hospital)

3.6 Chapter conclusions

In this chapter, a novel model is proposed to approximate the behavior of RILD by extending and generalizing a first-order all-pass filter into a fractional-order filter. The causality of the proposed model is confirmed and its time-domain representation is derived and expressed in terms of the Mittag-Leffler relaxation function. For physical representation of the proposed model, a mechanical system consisting of a fractional-order Maxwell and a negative stiffness elements coupled in parallel is constructed (referred to as fractional-Maxwell-negative-stiffness (FMNS) model), which is a generalization of the MNS model proposed in Chapter 2. Both passive and semi-active methods are suggested to physically realize the FMNS model for practical engineering applications.

The relationships between the proposed model with existing causal RILD models (e.g., Biot, Makris, TMW, and Keivan models) are discussed in detail. It is shown that the proposed model can include both Makris and Keivan models as its special cases with $\alpha = 0$ and $\alpha = 1$, respectively, and the proposed model with a fractional order (e.g., $\alpha = 0.1$) can be equivalent to a TMW model, which is able to approximate the Biot model for practical applications. Therefore, the proposed model can be considered as a unified causal RILD model.

Furthermore, the Keivan model is found to be equivalent to a first-order approximation of the Biot model if the dynamic stiffness of the latter is expanded by using a Mercator series. These newly revealed relationships between different models, along with the established ones, enable the development of a unified framework of causal RILD models.

A time-domain analysis method is developed by directly calculating the fractional derivative on the basis of the so-called L1 algorithm, which can serve as a useful tool for numerical implementation of the FMNS model in a structural response analysis problem. Such a method can be readily embedded into established numerical integration schemes, and thus can be readily used for nonlinear response analyses of a structural system incorporated with the FMNS model. By applying the fixed memory principle, the computational efficiency of the developed method can be largely improved and consequently, the computational complexity can be reduced from $O(N^2)$ to $O(N)$ without significant loss of accuracy.

To verify its effectiveness, a base-isolated five-story structural model is used as an analytical example, and response history analyses are conducted for the structure incorporated with the FMNS model. Furthermore, the seismic performances of the structure separately incorporated with different causal RILD elements are compared. It is suggested that the FMNS model with a unity tunable parameter (i.e., the MNS model) can be used as a simpler option to approximate the behavior of ideal RILD in a nonlinear base-isolation system without significantly compromising the structural seismic performance, when compared to other more complicated RILD models in the unified framework.

Compared with the MNS model, the FMNS model can provide an improved approximation of RILD in the sense of an extended frequency range, over which the rate-independent dissipation behavior can be mimicked. This feature may be important to approximate the behavior of RILD over multiple modal frequencies of a structural system, especially for evaluating the floor-response acceleration response. However, one cannot fully explore the importance of this feature by incorporating the FMNS model in a base-isolation system. For approximating the behavior of multiple ideal RILD elements distributed in an MDF structure, a causal model which can exhibit rate-independent dissipation behavior over an extended frequency range is preferred, as to be discussed in Chapter 4.

Chapter 4

An Efficient Method for a Structural Model Incorporated with RILD

4.1 Introduction

As a purely dynamic property of a structure (or material), damping can only be measured by conducting dynamic testing. To this end, harmonic vibration testing is conducted in most cases because of its simplicity. In this way, the characteristic parameters to describe the damping behavior of a structure (or material) are estimated by varying the deformation (force) amplitude and/or the excitation frequency. Consequently, a candidate damping model which can fit the experimental data in an acceptable degree is usually developed in the frequency domain. Such a damping model may be conveniently used in a structural system and readily analyzed in the frequency domain by virtue of fast Fourier transform (FFT) algorithm, provided that certain conditions (e.g., linearity and stability) are satisfied. However, in many applications, it is preferred to interpret the damping model from the frequency domain to the time domain. For example, in order to use existing commercial softwares for building structural design, a time-domain description of the damping model is required because most of the softwares can only support time-domain algorithms for dynamic analyses in a digital computer. Moreover, time-domain methods are necessary when the nonlinear behaviors of structural or supplemental damping elements should be taken into account in dynamic analyses, e.g., when the structure is subjected to extreme earthquake events.

Among many candidate models for describing damping behavior of materials, RILD is thought to be one of the most promising models which can comply well with the experimental data of many solid materials in a considerable frequency range [23]. RILD is indeed an idealized outcome from the dynamic experimental studies, and it is naturally convenient to be used and analyzed in the frequency domain. However, when transferred to the time domain, the ideal RILD model fails to satisfy the requirement of causality [28], which not only makes it impossible to be physically realized by using real-world devices, but also makes it challenging to be applied and numerically implemented in a nonlinear simulation problem.

In the past decades, some attempts have been made to enable time-domain simulation of the ideal RILD element. For example, Inaudi and Kelly [38] suggested an iterative calculation method for dynamic analyses of RILD systems in the time domain, and later Inaudi and Makris [39] proposed a more computationally efficient method by using analytical

(complex-valued) signals. The above methods may be extended to multi-degree-of-freedom systems, and used for dynamic analyses of different types of structural systems incorporated with RILD, e.g., geotechnical, mechanical, or space structures [41, 52, 92]. However, they are thought to have limited capabilities for nonlinear response history analysis of a structural model with RILD, when the nonlinearities of structural or supplemental damping devices are taken into account. For example, as discussed in reference [50], RILD elements can be supplemented to improve the seismic performance of low-frequency structures. Moreover, RILD may be used as a straightforward model of simulating the structural inherent damping without adopting the assumption of Rayleigh damping. In both cases, the nonlinear behaviors of structural components and/or supplemented energy dissipation devices (e.g., hysteretic dampers) should be properly considered for the performance evaluation of the structural system in extreme earthquake environments. Therefore, a time-domain analysis method for nonlinear simulations is of fundamental necessity.

To meet this necessity, a causal RILD element may be used instead of the ideal one. In the time domain, the damping force of a causal RILD element is typically expressed in the form of a convolution integral, resulting in an integro-differential equation which governs the motion of the structural system. Solving such an equation by using conventional methods results in an overall computational complexity of $O(N^2)$, where N denotes the number of time steps in an analysis. Consequently, it becomes a computationally expensive problem to conduct a dynamic analysis of a structural model with causal RILD, and an efficient method is required to accelerate the analysis, especially when a large number of iterative calculations are required, e.g., for nonlinear simulation or numerical optimization design problems. Indeed, some attempts [41, 42, 45] have been made to reduce the computational burden for the dynamic analysis of a structural model with causal RILD. However, limited researches have been reported on computationally efficient methods for the dynamic analysis of a structural model with the FMNS model, which is thought to be a unified causal RILD element, as discussed in Chapter 3.

In this chapter, a time-domain computationally efficient method is developed for dynamic analyses of a structural model incorporated with the FMNS model. In the time domain, the resulting damping force is expressed in the form of a convolution integral with the Mittag-Leffler relaxation function as a damping kernel. In order to reduce the computational burden associated with the convolution integral, a recursive method is developed by approximating the Mittag-Leffler relaxation function as a series of exponential relaxation processes, which are also known as Prony series [93]. The recursive method is readily embedded into established numerical integration schemes, and consequently, the structural system incorporated with the FMNS model can be efficiently analyzed without directly calculating the fractional derivative, as one does on the basis of L1-algorithm in Chapter 3. The effectiveness of the developed method is verified by using numerical examples, and comparisons between the developed methods with available methods are made. It is suggested the developed method can be used as an computationally efficient tool for the dynamic analysis of a structural model with RILD.

4.2 Governing equation of motion

4.2.1 Ideal noncausal RILD system

First, one considers a single-degree-of-freedom (SDF) structural system incorporated with ideal RILD, as shown in Fig. 4.1(a), where m and k denote the structural mass and primary stiffness, respectively, and $k_c(i\omega)$ denotes the damping function of the ideal RILD. The governing equation of motion of such a system can be expressed in the frequency domain as follows,

$$-m\omega^2 X(\omega) + [k + k_c(i\omega)]X(\omega) = F(\omega) \tag{4.1}$$

where $k_c(i\omega) = i\eta k \,\mathrm{sgn}(\omega)$ is assumed; η denotes the loss factor; $i = \sqrt{-1}$; $\mathrm{sgn}(\cdot)$ denotes the signum function; $F(\omega)$ denotes the external exciting force. Assuming that the above system is stable and absolutely integrable, the above equation can be inverse Fourier transformed into the time domain as follows,

$$m\ddot{x}(t) + k[x(t) + \eta\hat{x}(t)] = f(t) \tag{4.2}$$

where $\hat{x}(t)$ denotes the Hilbert transform of $x(t)$, which is defined as follows,

$$\hat{x}(t) = \mathscr{F}^{-1}[i\,\mathrm{sgn}(\omega)X(\omega)] = -\frac{1}{\pi t} * x(t) = -\frac{1}{\pi}\int_{-\infty}^{\infty}\frac{x(\tau)}{t-\tau}d\tau \tag{4.3}$$

where $\mathscr{F}^{-1}(\cdot)$ denotes the inverse Fourier transform, and $*$ denotes the operation of convolution integral. Therefore, Eq.(4.2) is actually an integro-differential equation. It may be noticed that the damping force $\eta k\hat{x}(t)$ depends on not only the past known information of $x(t)$, but also that in the future, which is unknown and to be determined, i.e., the ideal RILD is noncausal. This property makes it challenging to solve Eq.(4.2) by using conventional integration methods. Some methods [38, 39] have been developed to overcome this challenge, however, they are thought to have limited capabilities for nonlinear dynamic analyses of structural systems incorporated with RILD.

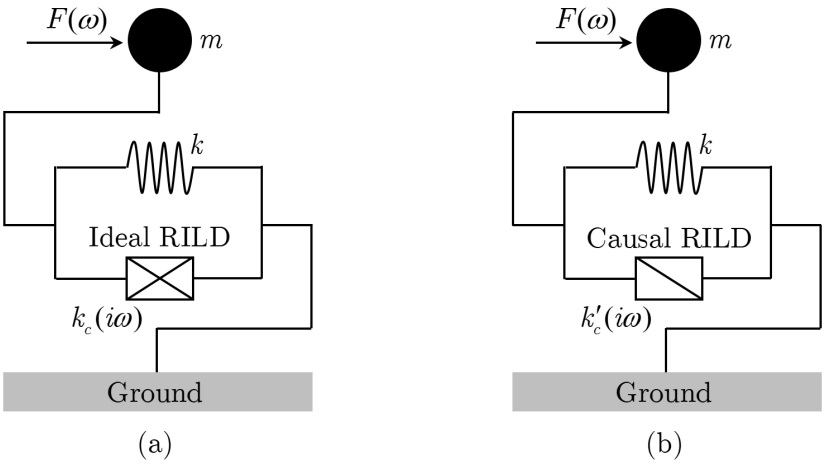

FIGURE 4.1: SDF systems with (a) ideal noncausal RILD and (b) causal RILD

4.2.2 Approximated causal RILD systems

In order to overcome the challenge of time-domain simulation of RILD, one can alternatively use a causal RILD element instead of the ideal noncausal one for dynamic analyses, as shown in Fig. 4.1(b), where $k_c'(i\omega)$ is the damping function of a causal RILD element. For such a system, the governing equation of motion can be expressed in the frequency domain as follows,

$$-m\omega^2 X(\omega) + [k + k_c'(i\omega)]X(\omega) = F(\omega) \tag{4.4}$$

where $k_c'(i\omega) = \eta k Z(i\omega)$ is assumed, i.e., $Z(i\omega)$ denotes a normalized damping function. For a causal RILD element, $Z(i\omega)$ can provide a good approximation of the unit imaginary function $i\mathrm{sgn}(\omega)$ in some sense.

In this chapter, the FMNS model is used because it is thought to be a unified causal RILD model that can encompass existing causal models. Then, the governing equation of motion of such a system is specified in the frequency domain as follows,

$$-m\omega^2 X(\omega) + k\left[1 + \eta\, Z_\alpha(i\omega)\right] X(\omega) = F(\omega) \tag{4.5}$$

where the normalized damping function $Z_\alpha(i\omega)$ is given as follows,

$$Z_\alpha(i\omega) = \beta_\alpha \frac{(i\omega)^\alpha - \varepsilon^\alpha}{(i\omega)^\alpha + \varepsilon^\alpha} \tag{4.6}$$

with $\beta_\alpha = \cot(\alpha\pi/4)$. Eq.(4.5) can be inverse Fourier transformed into the time domain as follows,

$$m\ddot{x}(t) + k\left[x(t) + \eta\, q_\alpha(t) * \dot{x}(t)\right] = f(t) \tag{4.7}$$

where $q_\alpha(t)$ denotes the damping kernel or relaxation function of the FMNS model

$$q_\alpha(t) = \mathscr{F}^{-1}\left[\frac{\mathcal{Z}_\alpha(i\omega)}{i\omega}\right] = \beta_\alpha u(t)\left[2E_\alpha(-\varepsilon^\alpha t^\alpha) - 1\right] \tag{4.8}$$

where $u(t)$ denotes the Heaviside's step function; $E_\alpha(z)$ denotes the Mittag-Leffler relaxation function defined as follows,

$$E_\alpha(z) = \sum_{n=1}^{\infty} \frac{z^n}{\Gamma(\alpha n + 1)} \tag{4.9}$$

Substituting Eq.(4.8) into Eq.(4.7) gives

$$m\ddot{x}(t) + (k - k_N)x(t) + k_\alpha\left[E_\alpha(-\varepsilon^\alpha t^\alpha)u(t)\right] * \dot{x}(t) = f(t) \tag{4.10}$$

with $k_N = \eta\beta_\alpha k$ and $k_\alpha = 2\eta\beta_\alpha k$, respectively. Letting $\bar{I}_\alpha(t)$ denote the convolution integral in Eq.(4.10), one may evaluate it by using a conventional quadrature rule as follows,

$$\bar{I}_\alpha(t) = \int_0^t E_\alpha(-\varepsilon^\alpha \tau^\alpha)\dot{x}(t-\tau)d\tau \approx \sum_{j=0}^{N} w_j \dot{x}(t_j) \tag{4.11}$$

where w_j and $\dot{x}(t_j)$ denote the quadrature weight and node, respectively. In many applications, the external excitation $f(t)$ are discrete data specified at equally-spaced time nodes $t_j = jh$ (h is the step length), and one may pursue the solution of Eq.(4.10) at these time nodes. For this purpose, the trapezoidal or Simpson rule may be readily used. However, this results in a computational complexity of $O(N^2)$ to solve Eq.(4.10), and the quadrature weights w_j are determined by evaluating the Mittag-Leffler function, which causes additional computational burden.

4.3 A Prony-series-based recursive method

4.3.1 The basic formulation

Here, in order to reduce the computational burden to solve Eq.(4.10) in the time domain, the Mittag-Leffler relaxation function is approximated as a superposition of different exponential relaxation processes as follows,

$$E_\alpha(-\varepsilon^\alpha t^\alpha) \approx \sum_{j=1}^{p} b_j e^{-a_j \varepsilon t} \tag{4.12}$$

which are known as the Prony series [41]. In the above equation, p is the number of relaxation processes, and is also referred to as the order of a Prony series. It is worth noting that $E_\alpha(-\varepsilon^\alpha t^\alpha)$ tends to unity as $t \to 0^+$, therefore, the damping kernel function of the FMNS model is nonsingular at the time origin (recall that the damping kernel of the Biot model suffers singularity at the time origin), and one has $\sum_{j=1}^{p} b_j \approx 1$.

Provided the damping kernel approximated by a Prony series, the convolution integral $\bar{I}_\alpha(t)$ can be approximated as follows,

$$\bar{I}_\alpha(t) \approx \sum_{j=1}^{p} b_j e^{-a_j \varepsilon t} * \dot{x}(t) \tag{4.13}$$

and then a recursive method can be developed to numerically solve Eq.(4.10). To this end, letting $t = nh$, $n = 0, 1, 2, ..., N-1$, the following recursive relation is considered

$$I_j(n+1) = \int_0^{nh+h} e^{-a_j \varepsilon (t-\tau)} \dot{x}(\tau) d\tau \approx e^{-a_j \varepsilon h} I_j(n) + \frac{h}{2}\left[e^{-a_j \varepsilon h} \dot{x}(n) + \dot{x}(n+1)\right] \tag{4.14}$$

with $j = 1, 2, ..., p$. By substituting the above relation into Eq.(4.13), one can evaluate $\bar{I}_\alpha(t)$ in a recursive manner as follows,

$$\bar{I}_\alpha(n+1) \approx \sum_{j=1}^{p} b_j I_j(n+1) \approx \mathbf{L}_{1\times p}\mathbf{I}_{p\times 1}(n) + \tau_1 \dot{x}(n) + \tau_0 \dot{x}(n+1) \tag{4.15}$$

where the vectors $\mathbf{L}_{1\times p} = \{L_1, L_2, ..., L_p\}$ and $\mathbf{I}_{p\times 1} = \{I_1, I_2, ..., I_p\}^T$ are used, and the coefficients can be respectively determined as follows,

$$L_j = b_j e^{-a_j \varepsilon h},\ \tau_1 = \frac{h}{2}\sum_{j=1}^{p} b_j e^{-a_j \varepsilon h} \approx \frac{h}{2} E_\alpha(-\varepsilon^\alpha h^\alpha),\ \tau_0 = \frac{h}{2}\sum_{j=1}^{p} b_j \approx \frac{h}{2}.$$

Substituting Eq.(4.15) into Eq.(4.10) gives

$$m\ddot{x}(n+1)+(k-k_N)x(n+1)+k_\alpha\tau_0\dot{x}(n+1) = f(n+1)-k_\alpha\left[\mathbf{L}_{1\times p}\mathbf{I}_{p\times 1}(n)+\tau_1\dot{x}(n)\right] \tag{4.16}$$

which can be expressed in a more compact form as follows,

$$m\ddot{x}(n+1) + c_0\dot{x}(n+1) + k_e x(n+1) = f_e(n+1) \tag{4.17}$$

where $k_e = k - k_N$, $c_0 = \tau_0 k_\alpha$, $f_e(n+1) = f(n+1) - k_\alpha\left[\mathbf{L}_{1\times p}\mathbf{I}_{p\times 1}(n) + \tau_1\dot{x}(n)\right]$. Eq.(4.17) can be readily solved by using established numerical integration schemes, e.g., Newmark's method or Runge-Kutta method. It should be mentioned that by utilizing the above recursive procedure, one can reduce the overall computational complexity of solving Eq.(4.10) from $O(N^2)$ to $O(N)$.

Of course, provided the Prony series to approximate the Mittag-Leffler relaxation function, one can also physically interpret them as the relaxation function of a Maxwell-Weichert model and reformulate Eq.(4.10) as a second-order differential equation coupled with a series of first-order differential equations (e.g., see reference [33]). However, this formulation increases the structural dimensions for dynamic analyses due to the additional degrees of freedom, which may compromise the computational efficiency for large-scale simulation problems, e.g., the soil-structure interaction simulation of nuclear power plant, where the soil dynamics is modeled by using rate-independent damping elements [51]. Moreover, because a theoretical Maxwell-Weichert model doesn't consist of any mass element, the resulting mass matrix of the whole structural system is singular, which may cause potential problems for dynamic analyses by applying conventional methods [49]. The above recursive formulation neither increases the structural matrix dimension nor causes a problem of singular matrix (as to be discussed below), and thus it is preferred for the dynamic analysis of a structural model with RILD.

4.3.2 Extension to MDF structural systems

Here, for brevity, a two-degree-of-freedom system incorporated with the FMNS model is considered. The governing equation of motion can be expressed in matrix as follows,

$$\mathbf{m}\ddot{\mathbf{x}}(t) + (\mathbf{k} - \mathbf{k}_N)\mathbf{x}(t) + \int_0^t \mathbf{G}(t-\tau)\dot{\mathbf{x}}(\tau)d\tau = -\mathbf{m}\mathbf{J}_{2\times 1}\ddot{x}_g(t) \tag{4.18}$$

where $\mathbf{m}$ and $\mathbf{k}$ are the mass and stiffness matrices of the primary structural system, respectively; $\mathbf{k}_N$ is the stiffness matrix due to the negative stiffness elements; $\mathbf{G}(t)$ is the damping kernel matrix of fractional-order Maxwell elements; $\mathbf{x}(t)$ is the displacement vector relative

to the ground; $\mathbf{J}_{2\times1}$ is the identity vector. These matrices and vectors are specified as follows,

$$\mathbf{m} = \begin{bmatrix} m_1 & \\ & m_2 \end{bmatrix},\ \mathbf{k} = \begin{bmatrix} k_1+k_2 & -k_2 \\ -k_2 & k_2 \end{bmatrix},\ \mathbf{k}_N = \begin{bmatrix} {}_1k_N+{}_2k_N & -{}_2k_N \\ -{}_2k_N & {}_2k_N \end{bmatrix},$$

$$\mathbf{G}(t) = \begin{bmatrix} {}_1k_\alpha\bar{G}_1(t)+{}_2k_\alpha\bar{G}_2(t) & -{}_1k_\alpha\bar{G}_2(t) \\ -{}_2k_\alpha\bar{G}_2(t) & {}_2k_\alpha\bar{G}_2(t) \end{bmatrix},\ \mathbf{x} = \begin{Bmatrix} x_1 \\ x_2 \end{Bmatrix},\ \mathbf{J}_{2\times1} = \begin{Bmatrix} 1 \\ 1 \end{Bmatrix}.$$

In order to solve Eq.(4.18) in a recursive manner, by defining the following matrices

$$\mathbf{T} = \begin{bmatrix} 1 & -1 \\ 0 & 1 \end{bmatrix},\ \mathbf{k}_\alpha^{\mathrm{D}} = \begin{bmatrix} {}_1k_\alpha & 0 \\ 0 & {}_2k_\alpha \end{bmatrix},\ \bar{\mathbf{G}}_{\mathrm{D}}(t) = \begin{bmatrix} \bar{G}_1(t) & 0 \\ 0 & \bar{G}_2(t) \end{bmatrix}.$$

one can express the damping kernel matrix as follows,

$$\mathbf{G}(t) = \mathbf{T}\mathbf{k}_\alpha^{\mathrm{D}}\bar{\mathbf{G}}_{\mathrm{D}}(t)\mathbf{T}^T \tag{4.19}$$

where the superscript ' T ' denotes the transpose operation. Then, one can reformulate the matrix operation of the following convolution integral

$$\bar{\mathbf{I}}(t) = \mathbf{G}(t) * \dot{\mathbf{x}}(t) = \mathbf{T}\mathbf{k}_\alpha^{\mathrm{D}}\bar{\mathbf{G}}_{\mathrm{D}}\mathbf{T}^T * \dot{\mathbf{x}}(t) = \mathbf{T}\mathbf{k}_\alpha^{\mathrm{D}}\mathbf{R}(t) \tag{4.20}$$

where

$$\mathbf{R}(t) = \bar{\mathbf{G}}_{\mathrm{D}}(t)\mathbf{T}^T * \dot{\mathbf{x}}(t) = \bar{\mathbf{G}}_{\mathrm{D}}(t) * \dot{\mathbf{\Delta}}(t) \tag{4.21}$$

with $\dot{\mathbf{\Delta}}(t) = \mathbf{T}^T\dot{\mathbf{x}}(t)$. Assume that the damping kernel $\bar{G}_i(t)$ is approximated by using Prony series as follows,

$$\bar{G}_i(t) \approx \sum_{j=1}^{p} {}_jb_i \cdot e^{-{}_ja_i\cdot t} \tag{4.22}$$

Then, by using Eq.(4.15), one has

$$R_i(n+1) = \bar{G}_i(t) * \dot{\Delta}_i(t) \approx \mathbf{L}_i\mathbf{I}_i(n) + \frac{h}{2}\bar{G}_i(h)\dot{\Delta}_i(n) + \frac{h}{2}\bar{G}_i(0)\dot{\Delta}_i(n+1) \tag{4.23}$$

where $\mathbf{L}_i = \{{}_1L_i, {}_2L_i, ..., {}_pL_i\}$ and $\mathbf{I}_i = \{{}_1I_i, {}_2I_i, ..., {}_pI_i\}^T$ are $1\times p$ and $p\times1$ vectors, respectively; their components are given as follows,

$${}_jL_i = {}_jb_i \cdot e^{-{}_ja_i\cdot h},\ \ {}_jI_i(n+1) = e^{-{}_ja_i\cdot h}\cdot {}_jI_i(n) + \frac{h}{2}e^{-{}_ja_i\cdot h}\dot{\Delta}_i(n) + \frac{h}{2}\dot{\Delta}_i(n+1),$$

respectively, with $i = 1, 2$; $j = 1, 2, ..., p$. The above relations can also be reformulated in more compact forms as follows,

$$\mathbf{L}_i = \mathbf{b}_i e^{-h\mathbf{a}_i},\ \mathbf{I}_i(n+1) = e^{-h\mathbf{a}_i}\mathbf{I}_i(n) + \frac{h}{2}e^{-h\mathbf{a}_i}\mathbf{J}_{p\times1}\dot{\Delta}_i(n) + \frac{h}{2}\mathbf{J}_{p\times1}\dot{\Delta}_i(n+1). \tag{4.24}$$

where $\mathbf{b}_i = \{{}_1b_i, {}_2b_i, ..., {}_pb_i\}$ and $\mathbf{a}_i = \mathrm{Diag}\{{}_1a_i, {}_2a_i, ..., {}_pa_i\}$ are $1\times p$ vector and $p\times p$ diagonal matrix, respectively.

Define the following matrix and vector, respectively,

$$\mathbf{L}_{\mathrm{D}} = \begin{bmatrix} \mathbf{L}_1 & \mathbf{0} \\ \mathbf{0} & \mathbf{L}_2 \end{bmatrix}, \mathbf{I}_{\mathrm{V}} = \begin{Bmatrix} \mathbf{I}_1 \\ \mathbf{I}_2 \end{Bmatrix},$$

and recall that $\dot{\boldsymbol{\Delta}}(t) = \mathbf{T}^T\dot{\mathbf{x}}(t)$, one can express Eq.(4.23) in matrix as follows,

$$\mathbf{R}(n+1) = \mathbf{L}_{\mathrm{D}}\mathbf{I}_{\mathrm{V}}(n) + \frac{h}{2}\left[\bar{\mathbf{G}}_{\mathrm{D}}(h)\mathbf{T}^T\dot{\mathbf{x}}(n) + \bar{\mathbf{G}}_{\mathrm{D}}(0)\mathbf{T}^T\dot{\mathbf{x}}(n+1)\right] \tag{4.25}$$

Substituting Eq.(4.25) into Eq.(4.20) gives

$$\bar{\mathbf{I}}(n+1) = \mathbf{T}\mathbf{k}_\alpha^{\mathrm{D}}\mathbf{L}_{\mathrm{D}}\mathbf{I}_{\mathrm{V}}(n) + \frac{h}{2}\mathbf{G}(h)\dot{\mathbf{x}}(n) + \frac{h}{2}\mathbf{G}(0)\dot{\mathbf{x}}(n+1) \tag{4.26}$$

Letting $\boldsymbol{\Psi} = \mathbf{T}\mathbf{k}_\alpha^{\mathrm{D}}\mathbf{L}_{\mathrm{D}}$, $\mathbf{c}_h = \frac{h}{2}\mathbf{G}(h)$ and $\mathbf{c}_0 = \frac{h}{2}\mathbf{G}(0)$, one can reformulate the above equation as follows,

$$\bar{\mathbf{I}}(n+1) = \boldsymbol{\Psi}\mathbf{I}_{\mathrm{V}}(n) + \mathbf{c}_h\dot{\mathbf{x}}(n) + \mathbf{c}_0\dot{\mathbf{x}}(n+1) \tag{4.27}$$

Substituting Eq.(4.27) into Eq.(4.18) gives

$$\mathbf{m}\ddot{\mathbf{x}}(n+1) + \mathbf{c}_0\dot{\mathbf{x}}(n+1) + (\mathbf{k} - \mathbf{k}_N)\mathbf{x}(n+1) = -\mathbf{m}\mathbf{J}_{2\times1}\ddot{x}_g(n+1) - \boldsymbol{\Psi}\mathbf{I}_{\mathrm{V}}(n) - \mathbf{c}_h\dot{\mathbf{x}}(n) \tag{4.28}$$

Similar to the case of an SDF system, one can express the above equation as follows,

$$\mathbf{m}\ddot{\mathbf{x}}(n+1) + \mathbf{c}_0\dot{\mathbf{x}}(n+1) + \mathbf{k}_e\mathbf{x}(n+1) = \mathbf{f}_e(n+1) \tag{4.29}$$

where $\mathbf{k}_e = \mathbf{k} - \mathbf{k}_N$ and $\mathbf{f}_e(n+1) = -\mathbf{m}\mathbf{J}_{2\times1}\ddot{x}_g(n+1) - \boldsymbol{\Psi}\mathbf{I}_{\mathrm{V}}(n) - \mathbf{c}_h\dot{\mathbf{x}}(n)$. It can be verified that Eq.(4.29) can generalize Eq.(4.17) as a special case. These equations can be readily solved by using established numerical integration schemes.

It should be mentioned that although the above method is formulated for dynamic analyses of structural systems incorporated with the FMNS model, with minor revision, it can also be readily extended for analyzing other types of non-viscously damped systems [94]. Different types of models have different damping kernels, and thus different sets of Prony series coefficients may be used for approximation, but the above formulation is still applicable for dynamic analyses of those systems. For example, Spanos and Tsavachidis [42] used the Prony series to approximate the damping kernel of the Biot model. Even in the case of viscous damping, one has $\bar{G}_i(t) = \delta(t)$, which may be approximated by using a Prony series with ${}_ja_i \to \infty$ and $\sum_{j=1}^{p} {}_jb_i = 1$, and then one has $\mathbf{L}_{\mathrm{D}} = \mathbf{0}$ and $\mathbf{c}_h = \mathbf{0}$, and consequently Eq.(4.29) reduces to the governing equation of a conventional viscously damped system. In this sense, the above recursive method is thought to be a general method for structural dynamic analyses.

4.3.3 Parameter estimation of the Prony series

For a given number of p, the Prony series shown in Eq.(4.12) contain $2p$ parameters (a_j and $b_j, j = 1, 2, ..., p$) to be estimated for the approximation of a target function (e.g., the Mittag-Leffler relaxation function is considered in this study). For this purpose, both time-domain and frequency-domain methods can be used.

Provided that a target function is estimated at discrete equally-spaced time points $t_n = (n-1)h$ $(1 \leq n \leq N)$, e.g., letting $g_n = E_\alpha(-\varepsilon^\alpha t_n^\alpha)$, the parameter vectors $\mathbf{a} = \{a_1, a_2, ..., a_p\}^T$ and $\mathbf{b} = \{b_1, b_2, ..., b_p\}^T$ may be estimated by pursuing a best fit to the target function in the sense of least-squares of approximation errors

$$\chi_1^2(\mathbf{a}, \mathbf{b}) = \sum_{n=0}^{N-1} \epsilon_n^2 = \sum_{n=0}^{N-1} \left(g_n - \mathbf{b}^T e^{-\mathbf{a}\varepsilon t_n} \right)^2 \tag{4.30}$$

where the subscript '1' indicates the estimation error with respect to the time-domain data.

Due to the exponential term involved with $\mathbf{a}$, the above problem suffers strong nonlinearity. Some iterative algorithms for nonlinear regression analyses may be used to solve this strongly nonlinear problem, but this results in high computational burden. Alternatively, the least squares Prony method [93] may be used to overcome this challenge by separating the original highly nonlinear regression problem into a relatively easier polynomial factoring and a linear least square subproblems, for both of which reasonably fast algorithms are available for the solutions. An introduction of this method is given as follows.

Least-squares Prony method

The least-squares Prony method is known as a classical time-domain method for parameter estimation problems. Provided that a target function $g(t)$ is estimated at discrete equally-spaced time points from 0 to $(N-1)h$, the error between the target function and a Prony series can be expressed as follows,

$$\epsilon_n = g_n - \sum_{j=1}^{p} b_j z_j^n \tag{4.31}$$

for $n = 0, 1, 2, ..., N-1$, where $z_j = \exp[(-a_j \varepsilon h)]$. One can express the above equations in matrix as follows,

$$\begin{Bmatrix} \epsilon_0 \\ \epsilon_1 \\ \vdots \\ \epsilon_{N-1} \end{Bmatrix} = \begin{Bmatrix} g_0 \\ g_2 \\ \vdots \\ g_{N-1} \end{Bmatrix} - \begin{bmatrix} z_1^0 & z_2^0 & \cdots & z_p^0 \\ z_1^1 & z_2^1 & \cdots & z_p^1 \\ \vdots & \vdots & \ddots & \vdots \\ z_1^{N-1} & z_2^{N-1} & \cdots & z_p^{N-1} \end{bmatrix} \begin{Bmatrix} b_1 \\ b_2 \\ \vdots \\ b_p \end{Bmatrix} = \{g\} - \mathbf{Ab}. \tag{4.32}$$

If $N = 2p$, one may obtain an exact solution to the above matrix equation (i.e., $\epsilon_n = 0$, $n = 0, 1, ..., 2p-1$), and a Prony series can be designed to exactly represent the target function over the sample points. However, in most applications, one has $N \gg 2p$ and a best estimation of the Prony series may exist in the sense of least squares of the errors.

In order to separately determine z_j and b_j, it is crucial to construct a homogeneous linear constant-coefficient difference equation with z_j $(j = 1, 2, ..., p)$ as its solution. To this end, a polynomial $\phi(z)$ is defined with the exponents z_j as its roots, and can be expanded as follows

$$\phi(z) = \prod_{j=1}^{p}(z - z_j) = \sum_{k=0}^{p} \gamma_k z^{p-k} \tag{4.33}$$

with $\gamma_0 = 1$. Then, letting $\mathbf{A}_i$ denote a sub-matrix of $\mathbf{A}$ in Eq.(4.32), which contains the elements from the i-th to $(i + p)$-th rows. Notice that the matrix $\mathbf{A}$ has a Vandermonde structure, one has

$$\mathbf{A}_i = \begin{bmatrix} z_1^{i-1} & z_2^{i-1} & \cdots & z_p^{i-1} \\ z_1^{i} & z_2^{i} & \cdots & z_p^{i} \\ \vdots & \vdots & \ddots & \vdots \\ z_1^{i+p-1} & z_2^{i+p-1} & \cdots & z_p^{i+p-1} \end{bmatrix} = \begin{bmatrix} z_1^{0} & z_2^{0} & \cdots & z_p^{0} \\ z_1^{1} & z_2^{1} & \cdots & z_p^{1} \\ \vdots & \vdots & \ddots & \vdots \\ z_1^{p} & z_2^{p} & \cdots & z_p^{p} \end{bmatrix} \begin{Bmatrix} z_1^{i-1} \\ z_2^{i-1} \\ \vdots \\ z_p^{i-1} \end{Bmatrix} = \mathbf{A}_1 \cdot \{z^{i-1}\} \tag{4.34}$$

From Eq.(4.32), one can similarly obtain the following matrix equations

$$\{\epsilon\}_i = \{g\}_i - \mathbf{A}_i \mathbf{b} = \{g\}_i - \mathbf{A}_1 \cdot \{z^{i-1}\}\mathbf{b} \tag{4.35}$$

for $i = 1, 2, ..., N - p$, where $\{\epsilon\}_i = \{\epsilon_{i-1}, \epsilon_i, ..., \epsilon_{i+p-1}\}^T$, and $\{g\}_i = \{g_{i-1}, g_i, ..., g_{i+p-1}\}^T$. Define the following $(p + 1) \times 1$ vectors

$$\{\gamma\} = \{\gamma_0, \gamma_1, ..., \gamma_{p-1}, \gamma_p\}^T, \quad \{\check{\gamma}\} = \{\gamma_p, \gamma_{p-1}, ..., \gamma_1, \gamma_0\}^T.$$

where the above checked symbol denotes an order reverse operation with respect to a vector. Left-multiplying Eq.(4.35) by $\{\check{\gamma}\}^T$ gives

$$\bar{\epsilon}_i = \{\check{\gamma}\}^T\{\epsilon\}_i = \{\check{\gamma}\}^T\{g\}_i - \{\check{\gamma}\}^T\mathbf{A}_1 \cdot \{z^{i-1}\}\mathbf{b} = \{\check{\gamma}\}^T\{g\}_i = \{\check{g}\}_i^T\{\gamma\} \tag{4.36}$$

for $i = 1, 2, ..., N - p$, where the term involving $\mathbf{b}$ vanishes because z_j $(j = 1, 2, ..., p)$ are the roots of the Eq.(4.33). Recall that $\gamma_0 = 1$, the above equations can be expressed in matrix as follows,

$$\{\bar{\epsilon}\} = \begin{Bmatrix} \bar{\epsilon}_1 \\ \bar{\epsilon}_2 \\ \vdots \\ \bar{\epsilon}_{N-p} \end{Bmatrix} = \begin{Bmatrix} g_p \\ g_{p+1} \\ \vdots \\ g_{N-1} \end{Bmatrix} + \begin{bmatrix} g_{p-1} & g_{p-2} & \cdots & g_0 \\ g_p & g_{p-1} & \cdots & g_1 \\ \vdots & \vdots & \ddots & \vdots \\ g_{N-2} & g_{N-3} & \cdots & g_{N-p-1} \end{bmatrix} \begin{Bmatrix} \gamma_1 \\ \gamma_2 \\ \vdots \\ \gamma_p \end{Bmatrix} = \{g'\} + \mathbf{B} \cdot \{\gamma\} \tag{4.37}$$

From the above equation, one can obtain a best estimation of the polynomial coefficients $\{\gamma\}$ in the sense of least squares. With the estimated coefficients $\{\gamma\}$, one can numerically estimate the roots z_j $(j = 1, 2, ..., p)$ of the polynomial in Eq.(4.33). To this end, for example, one can refer to the algorithm by Jenkins [95].

With the roots z_j $(j = 1, 2, ..., p)$, one can estimate the coefficients a_j $(j = 1, 2, ..., p)$. Then,

one can estimate the remaining unknown coefficients b_j $(j = 1, 2, ..., p)$ by solving the following matrix equation

$$\begin{Bmatrix} g_0 \\ g_2 \\ \vdots \\ g_{p-1} \end{Bmatrix} - \begin{bmatrix} z_1^0 & z_2^0 & \dots & z_p^0 \\ z_1^1 & z_2^1 & \dots & z_p^1 \\ \vdots & \vdots & \ddots & \vdots \\ z_1^{p-1} & z_2^{p-1} & \dots & z_p^{p-1} \end{bmatrix} \begin{Bmatrix} b_1 \\ b_2 \\ \vdots \\ b_p \end{Bmatrix} = \begin{Bmatrix} 0 \\ 0 \\ \vdots \\ 0 \end{Bmatrix} \tag{4.38}$$

in which it is assumed that the designed Prony series exactly fits the target function at the first p sample points. Alternatively, with respect to Eq.(4.32), one can design a Prony series so that it can provide a best fit to the target function over all the sample points of investigation in the sense of least squares. In this study, the later strategy is employed. It should be mentioned that by using the above method, a_j and b_j $(j = 1, 2, .., p)$ are generally complex-valued. However, in most cases, their imaginary parts are typically negligible, and it is enough to only use their real parts for approximation of the target function. An example of applying the Prony method is given by Spanos and Tsavachidis [42] who discussed the dynamic analysis of a structural model with the Biot model.

Frequency-domain methods

The parameter estimation can also be made in the frequency domain. To this end, a Prony series is designed so that its Fourier transform can be used to approximate a target digital filter over a frequency range of interest.

Here, a target digital filter is chosen as the inverse Fourier transform of the Mittag-Leffler relaxation function and is given as follows,

$$\Lambda_t(i\omega) = \mathscr{F}^{-1}[E_\alpha(-\varepsilon^\alpha t^\alpha)] = \frac{(i\omega)^{\alpha-1}}{(i\omega)^\alpha + \varepsilon^\alpha} \tag{4.39}$$

where the subscript 't' indicates the target digital filter. The Fourier transform of a p-th order Prony series can be obtained as follows,

$$\bar{\Lambda}(i\omega) = \sum_{j=1}^{p} \frac{b_j}{i\omega + a_j\varepsilon} \tag{4.40}$$

It should be pointed out that the r.h.s. of Eq.(4.40) physically represents the impedance function of a Maxwell-Wiechert model consisting of p spring-dashpot branches coupled in parallel. In such a case, a_j and b_j can be physically interpreted as the normalized relaxation frequency (also known as the pole of force-velocity transfer function) and stiffness of the j-th branch, respectively. As $p \to \infty$, such a model can be used to physically represent the Biot model [32].

Provided that the target digital filter are specified at N discrete equally-spaced frequency sample points, say $\Omega = \{\omega_0, \omega_1, ..., \omega_{N-1}\}^T$, one may find a best estimation set of the parameter vectors $\mathbf{a} = \{a_1, a_2, ..., a_p\}^T$ and $\mathbf{b} = \{b_1, b_2, ..., b_p\}^T$ with respect to Eq.(4.40) in the

sense of least squares of approximation errors

$$\chi_2^2(\mathbf{a},\mathbf{b}) = \sum_{\mu=0}^{N-1} \left|\Lambda_t(i\omega_\mu) - \bar{\Lambda}(i\omega_\mu)\right|^2 \tag{4.41}$$

with $\omega_\mu \in \Omega$, where the subscript '2' indicates the estimation error with respect to the frequency-domain data. According to the Parseval's theorem, if N is sufficiently large, one has the following relation

$$\chi_2^2(\mathbf{a},\mathbf{b}) = \frac{1}{N}\chi_1^2(\mathbf{a},\mathbf{b}) \tag{4.42}$$

which can be derived by applying the discrete Fourier transform (DFT) method. In a general case, in order to simultaneously estimate the parameters of the Prony series from Eq.(4.41), one may use some iterative algorithms (e.g., see reference [96]) for solving this nonlinear regression problem.

However, for brevity, one can assume that the parameter vector $\mathbf{a}$ is specified as a priori, and consequently, the above problem can be formulated as a linear least-squares problem with respect to the unknown parameter vector $\mathbf{b}$ as follows,

$$\min \;\; \chi_2^2(\mathbf{b}) = \sum_{\mu=1}^{M}\left[\Lambda_t'(\omega_\mu) - \sum_{j=1}^{p}\Theta_{\mu j}' b_j\right]^2 + \sum_{\mu=1}^{M}\left[\Lambda_t''(\omega_\mu) - \sum_{j=1}^{p}\Theta_{\mu j}'' b_j\right]^2 \tag{4.43}$$

where $\Lambda_t'(\omega)$ and $\Lambda_t''(\omega)$ denote the real and imaginary parts of the target digital filter, respectively; and $\Theta_{\mu j}'$ and $\Theta_{\mu j}''$ can be expressed as follows,

$$\Theta_{\mu j}' = \frac{\varepsilon a_j}{\omega_\mu^2 + \varepsilon^2 a_j^2},\; \Theta_{\mu j}'' = \frac{-\omega_\mu}{\omega_\mu^2 + \varepsilon^2 a_j^2}.$$

Or in a more compact form, one can also formulate the above problem as follows,

$$\min \;\; \chi_2^2(\mathbf{b}) = \|\mathbf{\Lambda}_t - \mathbf{\Theta}\mathbf{b}\|_2 \tag{4.44}$$

where $\mathbf{\Lambda}_t$ and $\mathbf{\Theta}$ denote the target data vector and the so-called design matrix of a fitting problem, respectively, and they are given as follows,

$$\mathbf{\Lambda}_t = \begin{Bmatrix} \Lambda_t'(\Omega) \\ \Lambda_t''(\Omega) \end{Bmatrix},\; \mathbf{\Theta} = \begin{bmatrix} \Theta_1'(\Omega) & \Theta_2'(\Omega) & \cdots & \Theta_p'(\Omega) \\ \Theta_1''(\Omega) & \Theta_2''(\Omega) & \cdots & \Theta_p''(\Omega) \end{bmatrix}.$$

It should be mentioned that the above method has the freedom to specify the normalized relaxation frequency a_j $(j = 1, 2, ..., p)$ as a priori. This feature may be very useful in some applications, because the flexibility of specifying $\mathbf{a}$ may make it possible to approximate the target filter at any finite frequency range of interest. In the case of $N = p$, the above method results in an exact fitting of the target filter at those frequency points specified by $\mathbf{a}$, and an interpolation approximation of the target filter at the overall frequency range of investigation. An example of applying such a method is given by Genta and Amati [33] who use the word 'tuning' to represent this concept. In a more general case, one may have

$N \gg p$, and the above method results in a least-squares approximation of the target filter at a frequency range of interest.

To apply both the time- and frequency-domain methods, one requires an efficient method for a linear least-squares problem. For this purpose, either the singular value decomposition (SVD) method or the covariance method may be used. In this study, to solve the above problem, the covariance method is use first, because it is usually faster than the SVD method. If the first attempt fails to find the solution, e.g., when the normal matrix is close to be singular, the SVD method is used instead.

The remaining problem is to determine the number of exponentials p (i.e., the order of a Prony series). One may estimate it by using some order election rules or an SVD method. In either case, the maximum order is limited to $p \leq N/2$. A straightforward (but computationally expensive) method of determining the order p is to gradually increase the order from unity, and evaluate the parameters by using one of the above methods, and repeat the iterative processes until a certain error criterion is met.

For example, provided that the Mittag-Leffler relaxation function is estimated at time sample points over [0, 10] with a step length of 0.01 s, a time-domain (least-squares Prony) method is used for parameter estimation of the Prony series. Fig. 4.2 plots the error index in terms of χ_1^2 against the order of Prony series with respect to different tunable parameters. It is shown that a higher-order Prony series results in a better approximation of the target function. This example verifies the feasibility of the above strategy of estimating the required order p.

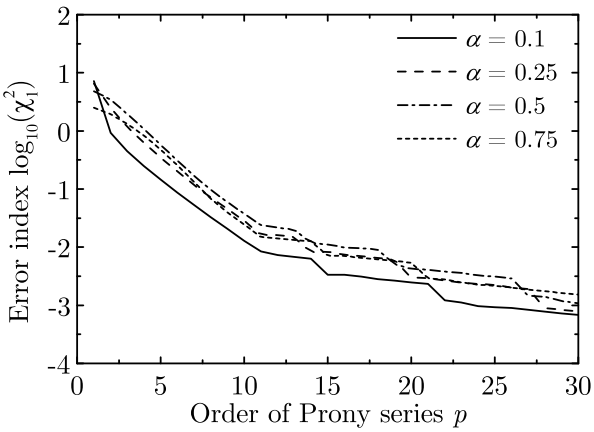

FIGURE 4.2: Approximation error of the estimated Prony series

4.3.4 Discussion on the application

Next, the application of the above recursive method for structural dynamic analyses is discussed, and its computational efficiency (in terms of both speed and accuracy) is compared to that of the L1-algorithm-based method (referred to as L1-algorithm) with a cutoff number

of $N_0 = 0.1N$. For this purpose, a linear SDF system ($T = 4.0$ s and $\eta = 0.1$) is considered here as an analytical example, and time history analyses are conducted by using the El Centro wave recorded in the 1940 Imperial Valley earthquake.

Fig. 4.3 compares the computational costs of the above recursive method with respect to the variations of the order of Prony series p (left) and the tunable parameter α (right), respectively. It is shown that the recursive method has a computational complexity of order $O(N)$, and it can be even faster than the L1-algorithm ($N_0 = 0.1N$). Moreover, from all the cases of investigation, the number p (when it is relatively small) and the tunable parameter α are found to have limited effects on the CPU time of dynamic analyses by using the recursive method. This suggests that by using the recursive method, a fractional-order system may be efficiently analyzed without significant increase of computational burden, compared with a conventional integer-order ($\alpha = 1$) system.

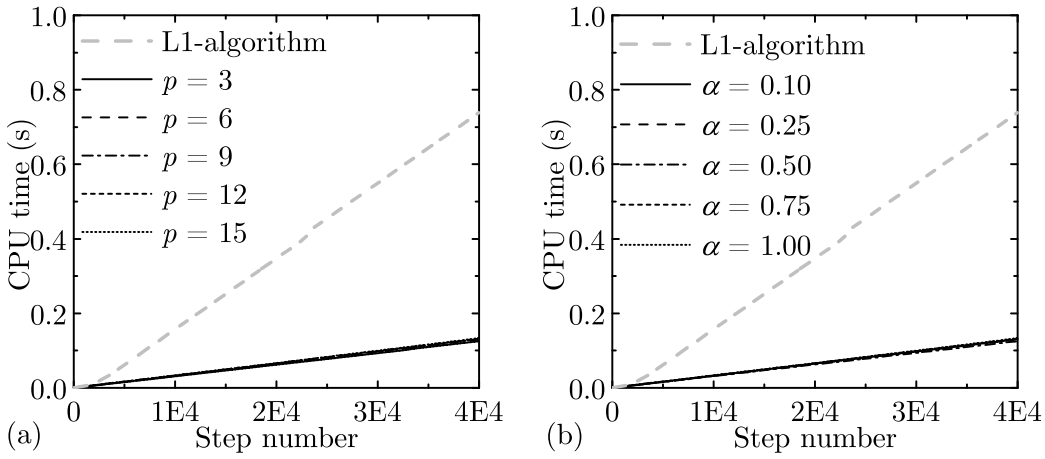

FIGURE 4.3: Comparison between the CPU times with respect to different (a) orders of Prony series ($\alpha = 0.1$), and (b) tunable parameters ($p = 9$).

Fig. 4.4 shows the percentage errors of the above recursive method in terms of the displacement peak (left) and RMS values (right) with respect to the variation of the tunable parameter, compared to the case of L1-algorithm ($N_0 = 0.1N$). Furthermore, letting $\alpha = 0.1$, Fig. 4.5 compares the percentage errors of the above recursive method for analyzing structures with different periods in terms of the displacement peak and RMS values. It is shown in these figures that the percentage errors in terms of both displacement peak and RMS values can be reduced to negligible levels if a sufficient high order Prony series is used for approximation (e.g., $p \geq 9$).

The above comparison studies suggest that the above recursive method can be used to efficiently analyze a structural model incorporated with the fractional-order RILD without significant loss of accuracy.

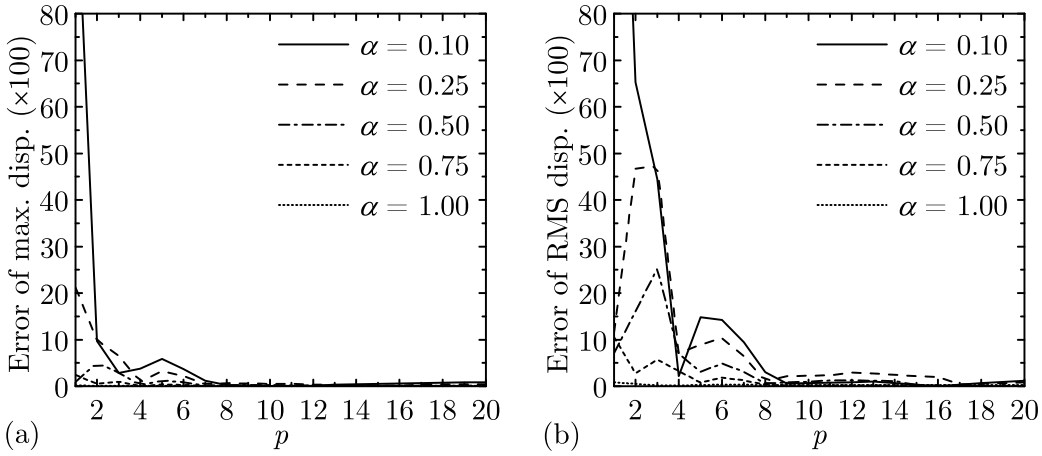

FIGURE 4.4: Percentage errors in terms of displacement (a) peak value and (b) RMS value for the proposed model with different tunable parameters

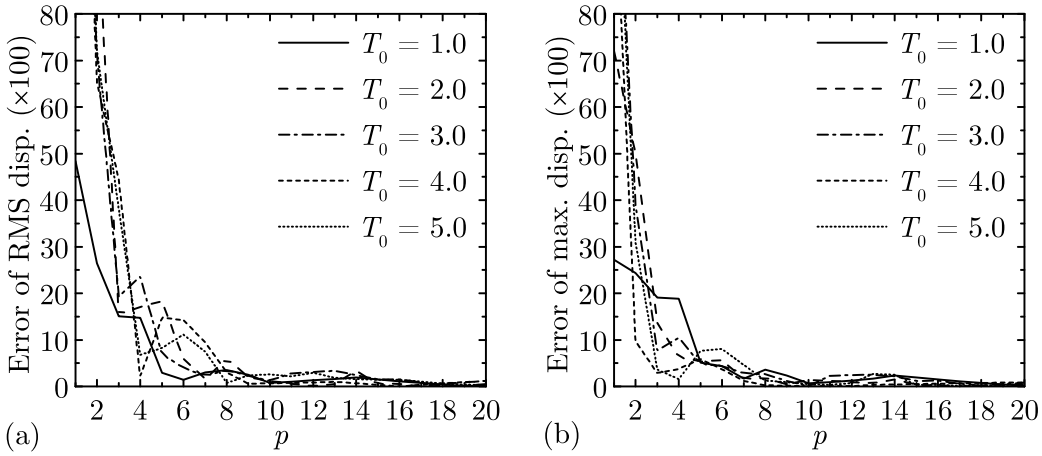

FIGURE 4.5: Percentage errors in terms of displacement (a) peak value and (b) RMS value with respect to different structural periods

4.4 Application for simulating the structural inherent damping

Here, the applicability of the FMNS model to approximate the behavior of ideal RILD for simulating the structural inherent damping is discussed, and the effectiveness of the developed method is further verified and compared with those of existing methods. For this purpose, a 10-story benchmark building structure incorporated with RILD is used as an analytical example, as shown in Fig. 4.6, and its structural parameters are listed in Table 4.1.

The yielding behavior of the resistant stiffness element is taken in account, and it is modeled by using a bilinear elasto-plastic stiffness element instead of a linear spring element, as shown in Fig. 4.6. The initial stiffness ${}_jk_1$, post-yielding stiffnesses ${}_jk_2$, and yielding deformation ${}_jx_y$ of the bilinear stiffness element at each story are listed in Table 4.1. The post-yielding stiffness ratio is assumed as 0.2, i.e., ${}_jk_2 = 0.2\ {}_jk_1$, and the yielding deformation is assumed to vary with the initial stiffness, i.e., ${}_jx_y = {}_1x_y/{}_1k_1 \cdot {}_jk_1$.

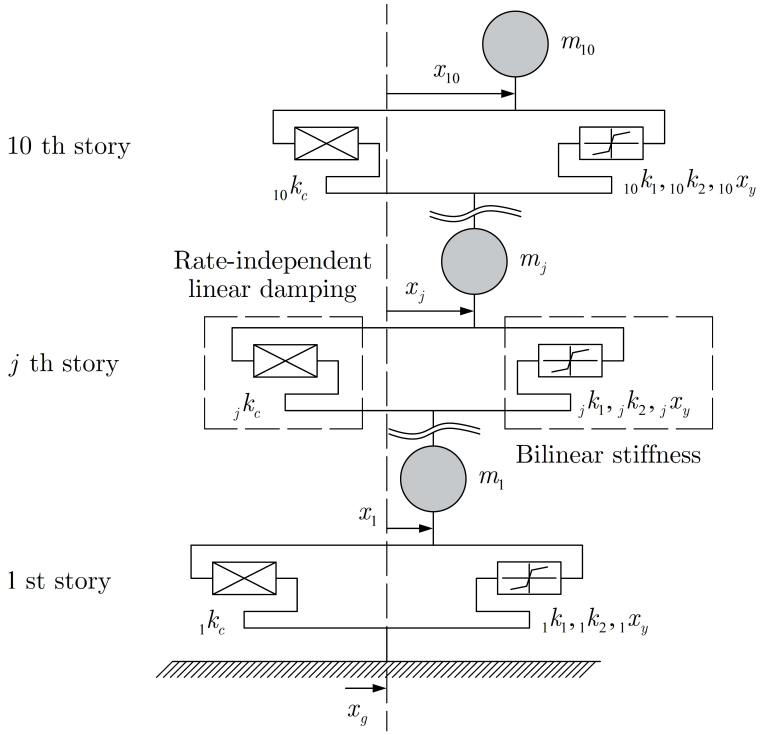

FIGURE 4.6: A 10-story benchmark building structure incorporated with RILD

Modal analysis is conducted for the undamped example structure in the initial linear state, and the modal characteristics are indicated in Table 4.2. It should be noticed that the first three modes contribute more than 95% of the participating mass.

TABLE 4.1: Structural parameters

Story number	m_j (ton)	${}_jk_1$ (kN/m)	${}_jk_2$ (kN/m)	${}_jx_y$ (m)	$\lvert{}_jk_c\rvert$ (kN/m)
1	700	279 960	55 992	0.036	27 996
2	682	383 550	76 710	0.050	38 355
3	680	383 020	76 604	0.050	38 302
4	676	328 260	65 652	0.043	32 826
5	670	306 160	61 232	0.040	30 616
6	667	291 890	58 378	0.038	29 189
7	660	244 790	48 958	0.032	24 479
8	656	220 250	44 050	0.029	22 025
9	649	186 110	37 222	0.024	18 611
10	875	158 550	31 710	0.021	15 855

In this study, the damping function of the ideal RILD element at the j-th story, ${}_jk_c$, is assumed to be proportional to the corresponding tangent stiffness, i.e.,

$$ {}_jk_c = i\eta \cdot {}_jk_t \cdot \mathrm{sgn}(\omega),\ j = 1, 2, ..., 10. \tag{4.45}$$

with $j = 1, 2, ..., 10$, where the loss factor is assumed to be uniform in the entire structure,

TABLE 4.2: Natural frequencies of the example structure (primary linear state)

Mode number	Natural period (s)	Natural frequency (rad/s)	(Hz)	Participating mass ratio (%)
1	2.01	3.13	0.50	82.07
2	0.75	8.33	1.33	11.36
3	0.46	13.69	2.18	3.65
4	0.33	18.89	3.01	1.43
5	0.26	23.97	3.81	0.66
6	0.22	28.16	4.48	0.37
7	0.20	32.08	5.11	0.21
8	0.18	35.52	5.65	0.14
9	0.16	39.61	6.30	0.06
10	0.14	44.19	7.03	0.05

e.g., $\eta = 0.1$ is used; ${}_jk_t$ denotes the tangent stiffness of the resisting stiffness element at the j-th story. Due to the noncausality of the ideal RILD element, a nonlinear response history analysis of the above structure is impractical when the yielding behavior of structural elements is taken into account, e.g., in order to investigate the seismic performance of the structure subjected to extreme ground motions. In such cases, causal RILD elements can be used instead of the ideal noncausal RILD element.

4.4.1 Linear response history analyses

Here, the FMNS model is compared with the Nakamura model [45] in terms of computational efficiency for response history analyses, as indicated in Table 4.3. For reference, the ideal RILD model is also considered and analyzed by using the frequency response analysis method when the structural elements remain linearly elastic.

TABLE 4.3: Different methods for dynamic analysis of a structure with RILD

Model	Analysis method	Comput. cost	Nonlinear simulation
Ideal RILD	Frequency response analysis	Low	×
Nakamura	Nakamura (2007)	Low	⊙
FMNS	Prony-series recursive	Low	⊙

×: Not applicable ⊙: Applicable

For the Nakamura model, a focused frequency range of interest from 0 to $\omega_m = 20\pi$ rad/s is considered (and the damping function beyond the frequency ω_m is assumed to vanish). Then, by conducting the Hilbert transform in Eq.(3.27) defined in the sense of Cauchy principal value, one can obtain an analytical expression of the normalized damping function of Nakamura model as follows,

$$Z_{\mathrm{N}}(i\omega) = \frac{2}{\pi}\left[\frac{1}{\omega_m} + \left(\frac{\omega}{\omega_m} - \frac{1}{2}\right)\ln\left(\frac{\omega_m}{\omega} - 1\right)\right] + i \tag{4.46}$$

and then to approximate an ideal RILD element at the j-th story by using the Nakamura model, one has

$$ {}_jk_{\mathrm{N}} = \eta \cdot {}_jk_{\mathrm{t}} \cdot Z_{\mathrm{N}}(i\omega) \tag{4.47} $$

In order to transform the above equation into the time domain, the method suggested by Nakamura [45] is used here. To this end, a length-M FIR-type filter is used to approximate the normalized damping function as follows,

$$ Z_{\mathrm{N}}(i\omega) \approx i\omega\bar{c}_0 + \sum_{n=1}^{M-1} \bar{k}_n e^{-i\omega nT} \tag{4.48} $$

where T denotes the sample time interval; $\bar{c}_0$ and $\bar{k}_n$ denote the coefficients used in velocity and displacement terms, respectively. Those coefficients can be readily estimated by using a linear regression method. Here, letting $\omega_m = 20\pi$ rad/s (i.e., 10 Hz, such a frequency range covers the natural frequencies of the structure indicated in Table 4.2), $M = 19$, $T = 0.05$ s.

Fig. 4.7 shows the recovered damping function of the Nakamura model from the approximation in Eq.(4.48), as well as those of the ideal RILD and FMNS models. For the Nakamura model, two different cases are considered: 1) an original one (referred to as Nakamura I), and 2) a modified one (referred to as Nakamura II) with its real part added by 1.05 to fit that of the proposed element at the center of the frequency range (5 Hz), as shown in Fig. 4.7(a). It should be mentioned that such a modification doesn't affect the causality of the model, and is also suggested by Nakamura [45] to control the accuracy for a specific frequency range.

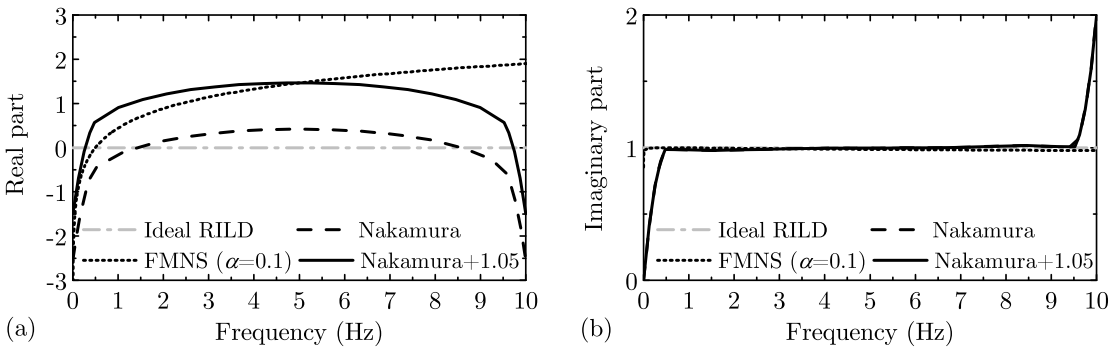

FIGURE 4.7: Damping functions of different RILD elements

For the proposed FMNS model, the cutoff frequency is set as the fundamental natural frequency of the primary linear structure, i.e., $\varepsilon = 3.14$ rad/s (0.5 Hz), and the tunable parameter α is fixed as 0.1 here. An approximation of the ideal RILD element at the j-th story by using the FMNS model is given as follows,

$$ {}_jk_{\mathrm{P}} = \eta \cdot {}_jk_{\mathrm{t}} \cdot Z_{\alpha}(i\omega) = \eta \cdot {}_jk_{\mathrm{t}} \cdot \beta_{\alpha} \frac{(i\omega)^{\alpha} - \varepsilon^{\alpha}}{(i\omega)^{\alpha} + \varepsilon^{\alpha}} \tag{4.49} $$

with $j = 1, 2, ..., 10$. Response history analyses are conducted by using the above developed recursive method, provided that the damping kernel is approximated by using a 9-th order

Prony series, so that the computational burden can be thought to be comparable to that for the 18-term Nakamura model.

To verify the accuracy of the FMNS method for approximation of the ideal RILD model, the seismic responses of differently damped structures subjected to the El Centro wave (N-S component) are investigated, respectively. Here, the peak ground velocity (PGV) of the ground motion is scaled as 0.25 m/s (corresponding to the design level earthquake in the practice used in Japan) so that the excited structures remain linearly elastic. In this case, time history analyses of the ideal RILD system can be conducted by using the frequency response analysis method.

Four different RILD elements are compared: ideal RILD, Nakamura I, Nakamura II, and FMNS. Response history analysis codes are run on an computer with an Intel Core 7, 3.40 GHz with 16 GB RAM, and the CPU times for separately analyzing the ideal RILD, the Nakamura, and the FMNS systems are 1.337, 2.564, and 2.594 s, respectively (with a time step length of 0.002 s, and a total time range of 81.92 s provided). This comparison verifies that the computational burden of the proposed method is comparable with that of the Nakamura method.

Fig. 4.8 shows the peak seismic responses at each story of differently damped structures, in terms of relative displacement, interstory drift, relative velocity, and absolute acceleration. It is suggested from this overall comparison that both the Nakamura and FMNS models can provide a good approximation of the ideal RILD in a general sense when used in the example structure.

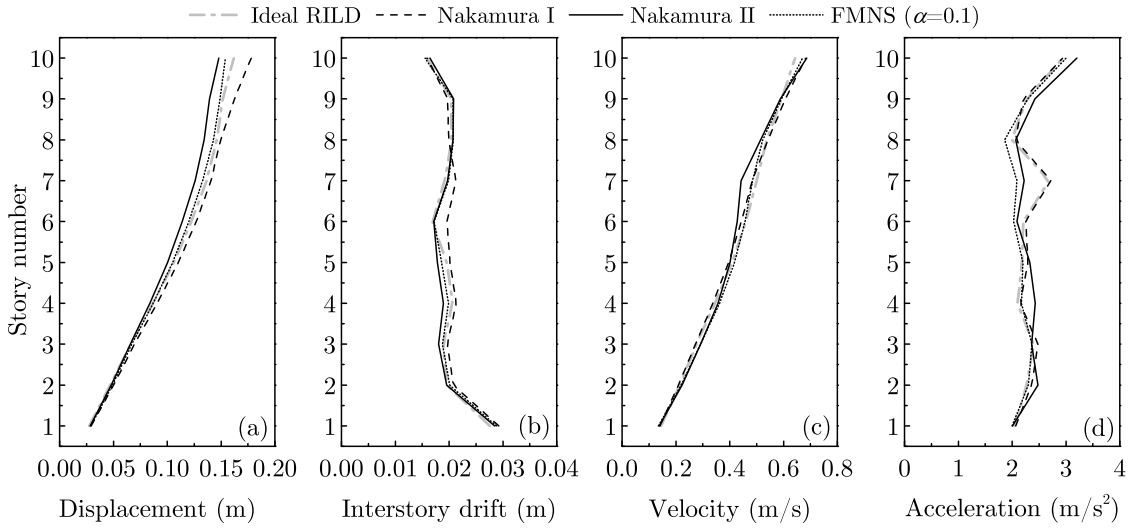

FIGURE 4.8: Peak seismic responses of differently damped structures

Fig. 4.9 compares the hysteresis loops of different RILD elements at the first story (where the largest deformation occurs) of the structure. It is shown that the hysteresis loop of the Nakamura I model has a negative skew (Fig. 4.9(a)), whereas that of the Nakamura II model has a positive skew (Fig. 4.9(b)). As an intermediate of the previous two cases, the hysteresis loop of the proposed model provides a best fit to that of the ideal RILD model (Fig. 4.9(c)). Indeed, a tunable value smaller than 1.05 may be used to modify the damping function of

the Nakamura model (say Nakamura III), so that the hysteresis loop can well fit that of the ideal RILD element. However, no further effort is made here to find such a value because it may be dependent on the structural characteristics and the frequency content of ground motions.

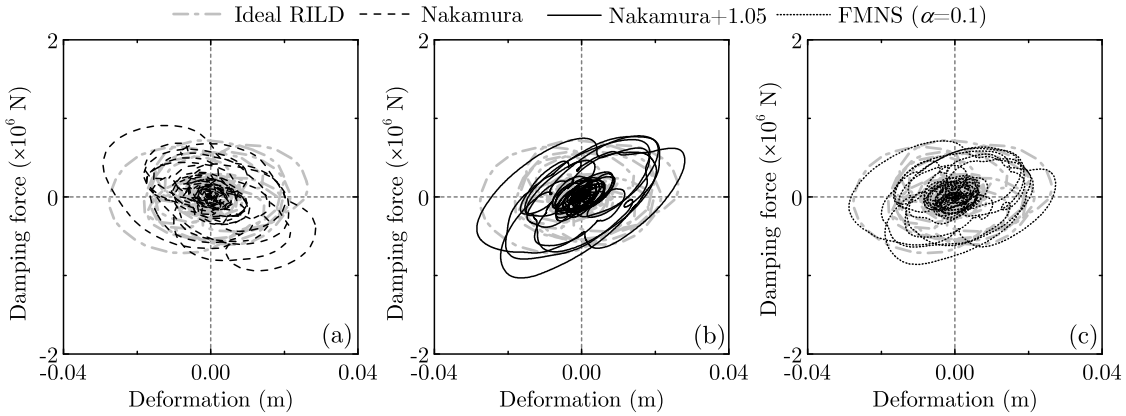

FIGURE 4.9: Hysteresis loops of different RILD elements at the first story of the structure

Table 4.4 summaries the maximum values among the seismic responses at each story of differently damped structures subjected to the El Centro wave, in terms of relative displacement, interstory drift, relative velocity, and absolute acceleration. Generally speaking, both the Nakamura and FMNS models can provide a good approximation of the ideal RILD. Particularly, the Nakamura I system can provide a best fit of the ideal RILD system in terms of the acceleration response at the expense of increased displacement responses. The Nakamura II system provides a better approximation in terms of interstory drift, at the expense of increased acceleration response. The FMNS model provides an intermediate approximation between the previous two cases in terms of interstory drift and acceleration, and a best approximation of the ideal RILD in terms of response displacement and velocity.

TABLE 4.4: Maximum seismic responses of differently damped structures (PGV = 25 cm/s, linear state)

Model	Displacement (cm)	Interstory drift (cm)	Velocity (cm/s)	Acceleration (cm/s^2)
Ideal RILD	16.1 (1.00)	2.76 (1.00)	64.5 (1.00)	294 (1.00)
Nakamura I	17.7 (1.10)	2.94 (1.07)	68.4 (1.06)	293 (1.00)
Nakamura II	14.8 (0.92)	2.86 (1.04)	68.7 (1.07)	321 (1.09)
FMNS	15.4 (0.96)	2.88 (1.04)	67.1 (1.04)	300 (1.02)

Note: the number in the parenthesis means the ratio to the response of the ideal RILD system.

The above comparison suggests that the FMNS model can be considered as an alternative model to approximate the ideal RILD. When it is incorporated into a structural system, response history analyses can be readily carried out by using the developed recursive method,

and the computational efficiency is comparable with that of the Nakamura model.

For the application of the Nakamura model, in order to control the accuracy for a frequency range specified by the threshold parameter ω_m, one may need to use an additional turnable value to correct the simultaneous stiffness term. To this end, trial calculations may be required to find a suitable value. Moreover, as pointed out in reference [45], the accuracy of calculating the damping function of the Nakamura model by the Hilbert transform at low-frequency ranges may be low. This may compromise its applicability in low-frequency structures.

However, for the FMNS model, one can readily set the cutoff frequency ε as the fundamental natural frequency of the structure, and the tunable parameter α as a small value (e.g., 0.1 may be used) so that this model can simulate the rate-independent dissipation behavior over a considerable frequency range. Moreover, the FMNS model can be readily used in low-frequency structure without suffering accuracy problems associated with the calculation of damping function, and the developed recursive method can be applied to conduct the response history analysis with a comparable computational burden as the Nakamura method. This is thought to be a potential advantage of the FMNS model over the Nakamura model for applications in low-frequency structures.

4.4.2 Nonlinear response dynamic analyses

Here, the seismic responses of the example structure subjected to strong ground motion are investigated by taking the nonlinear behavior of structural stiffness elements into account. To this end, the FMNS model is used instead of the ideal RILD element, and its dynamic stiffness is given in Eq. (4.49).

For comparison, the tangent-stiffness-proportional (TSP) damping model and the modal damping model [7] are also considered here. For the TSP damping model, one has the damping matrix given as follows,

$$\mathbf{c}_{\mathrm{t}}^{\mathrm{TSP}} = \frac{\eta}{{}_1\omega_1}\mathbf{k}_{\mathrm{t}} \tag{4.50}$$

where ${}_1\omega_1$ denotes the fundamental natural frequency from an eigenvalue analysis by using the initial stiffness matrix of the undamped structure.

For the modal damping model, the damping matrix is updated by conducting an eigenvalue analysis at each iterative step according to the tangent stiffness matrix (referred to as nonlinear modal damping (NLM) model). More specifically, the damping matrix $\mathbf{C}_{\mathrm{t}}$ of the NLM model is specified as a diagonal matrix with the j-th element as follows,

$${}_jC_{\mathrm{t}} = \eta\frac{{}_jK_{\mathrm{t}}}{{}_j\omega_{\mathrm{t}}} = \eta \cdot {}_j\omega_{\mathrm{t}} \cdot {}_jM_{\mathrm{t}} \tag{4.51}$$

where ${}_jK_{\mathrm{t}}$, ${}_jM_{\mathrm{t}}$, and ${}_j\omega_{\mathrm{t}}$ denote the modal stiffness, mass, and frequency of the j-th mode, respectively, which are estimated at each step in an analysis according to the tangent stiffness matrix of the structure. Then, the damping matrix can be recovered from the modal

damping matrix as follows,

$$\mathbf{c}_t^{\mathrm{NLM}} = \left(\mathbf{m}\boldsymbol{\Phi}_t\mathbf{M}_t^{-1}\right)\mathbf{C}_t\left(\mathbf{M}_t^{-1}\boldsymbol{\Phi}_t^T\mathbf{m}\right) \tag{4.52}$$

where $\boldsymbol{\Phi}_t$ denotes the modal matrix consisting of the normalized eigenvectors, which is updated at each step according to the tangent stiffness matrix. Notice that $\mathbf{M}_t$ and $\mathbf{C}_t$ are diagonal, the above equation can be reformulated as follows,

$$\mathbf{c}_t^{\mathrm{NLM}} = \eta\ \mathbf{m}\left(\sum_{j=1}^{J}\frac{{}_j\omega_t}{{}_jM_t}\cdot{}_j\phi_t\cdot{}_j\phi_t^T\right)\mathbf{m} \tag{4.53}$$

where J denotes the number of modes considered in the analysis. In this study, all the modes of the structure are taken into account for response history analyses, i.e., $J = 10$ for the example structure. Because an eigenvalue analysis is required for each iterative step in a nonlinear dynamic analysis, the computational burden of this method is thought to be relatively heavy.

For example, the seismic performances of the three differently damped structures subjected to the El Centro wave are investigated. In order to compare the responses of the three structures under different intensity-level earthquakes, the PGV of the El Centro wave is scaled as 25, 50, and 75 cm/s, respectively, which correspond to the design level, maximum considerable level, and an excessive level earthquakes in the design practice used in Japan.

Figs. 4.10-4.12 compares the peak seismic responses at each story of the structures subjected to different intensity-level earthquakes, respectively. Relatively small differences between seismic responses of the three structures are observed in terms of relative displacement, interstory drift, and relative velocity. However, the floor response accelerations at high stories of the TSP structure are obviously lower than those of the other two structures. This is in good agreement with the fact that the stiffness (both initial and tangent) proportional damping models underestimate the high-mode responses of structure because of the assumed excessive damping ratios at those modes. From the comparison between the seismic performances of the other two systems, it is suggested that under different different level earthquakes, the seismic responses of the FMNS system matches well with those of the NLM system in terms of the four performance indexes.

To further examine the seismic performance of the FMNS and NLM damping elements subjected to different intensity-level earthquakes, Fig. 4.13 compares the hysteresis loops of the two types of damping elements at the first story of the structure subjected to different intensity-level earthquakes. It can be observed from Fig. 4.13 that the FMNS model performs similarly as the nonlinear modal damping model in a general sense.

For the FMNS model, the damping force is proportional with the tangent stiffness of the bilinear stiffness element at the same story, and therefore, it is sensitive to the state transformation of the later. For example, as shown in Fig. 4.13(c), the damping force of the proposed model abruptly decreases to a much lower level at a deformation of about 0.1 m, which is companied with the state transformation of the structural stiffness element at the same story, as shown in Fig. 4.14(c). For the NLM model, a similar property can

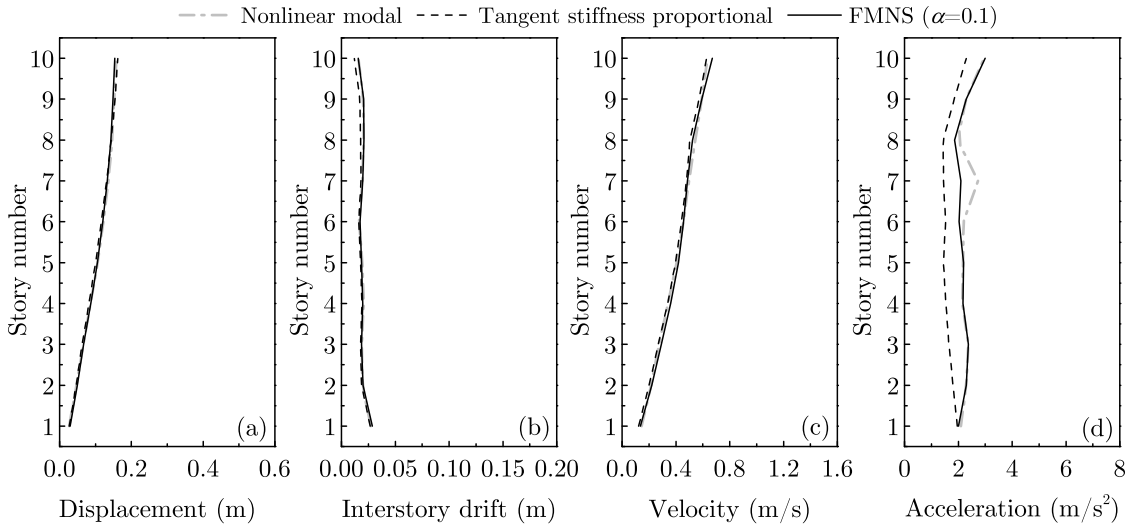

FIGURE 4.10: Peak seismic responses of differently damped structures (PGV=25 cm/s)

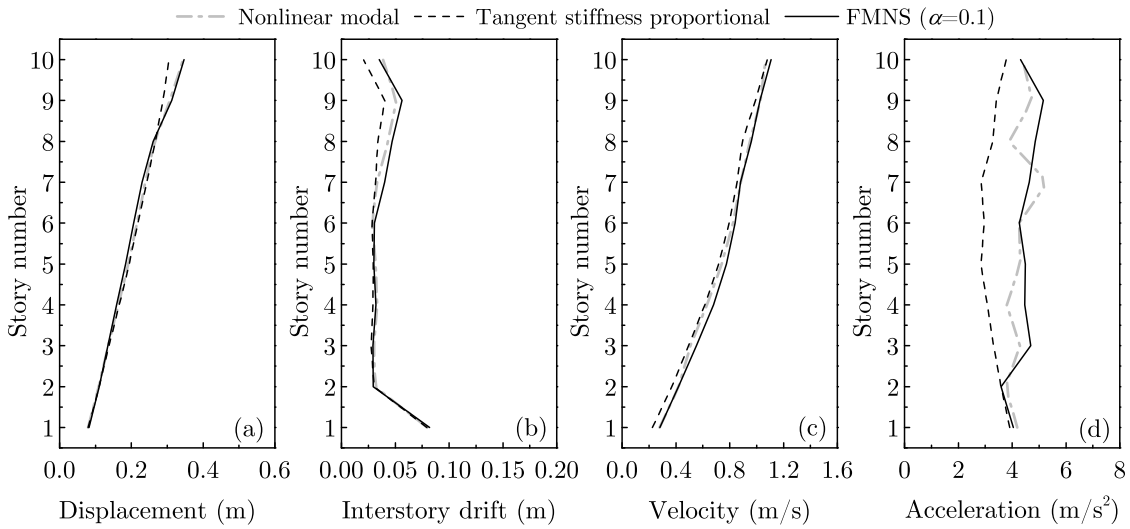

FIGURE 4.11: Peak seismic responses of differently damped structures (PGV=50 cm/s)

also be observed from Fig. 4.13(c), whereas the damping force shows less sensitivity to the state transformation of the structural stiffness element. This is partly because its damping coefficient is indirectly related with the structural stiffness through the modal characteristics of the whole structure at the very moment.

Table 4.5 summaries the maximum values among the seismic responses at each story of the above three types of structures subjected to different intensity-level earthquakes, in terms of relative displacement, interstory drift, relative velocity, and absolute acceleration. Generally speaking, the seismic responses of the structure incorporated with the FMNS model match well with those of the NLM system under different level earthquakes, whereas

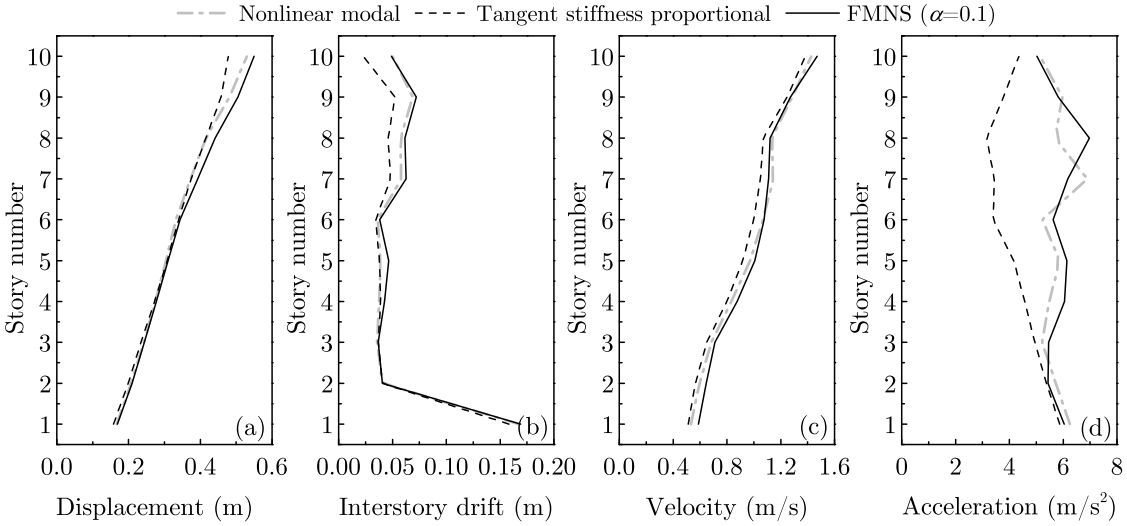

FIGURE 4.12: Peak seismic responses of differently damped structures (PGV=75 cm/s)

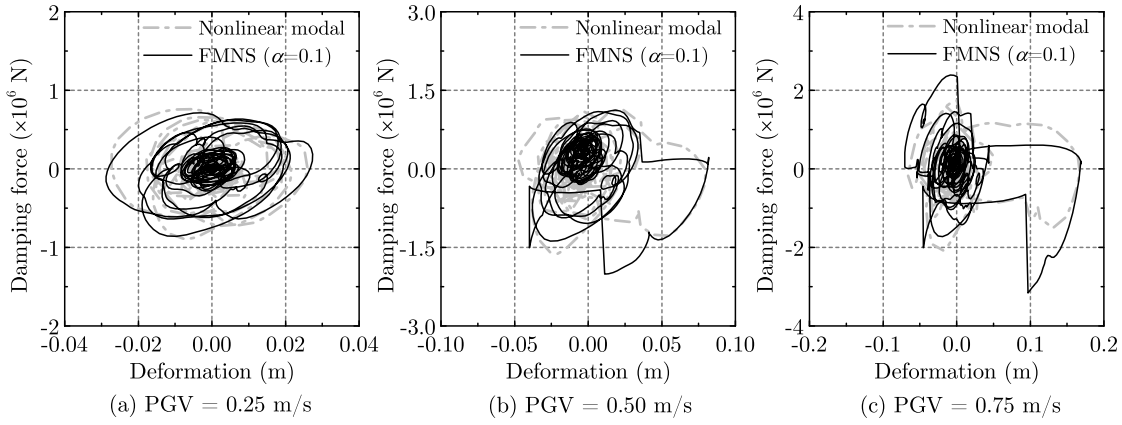

FIGURE 4.13: Hysteresis loops of damping elements at the 1st story

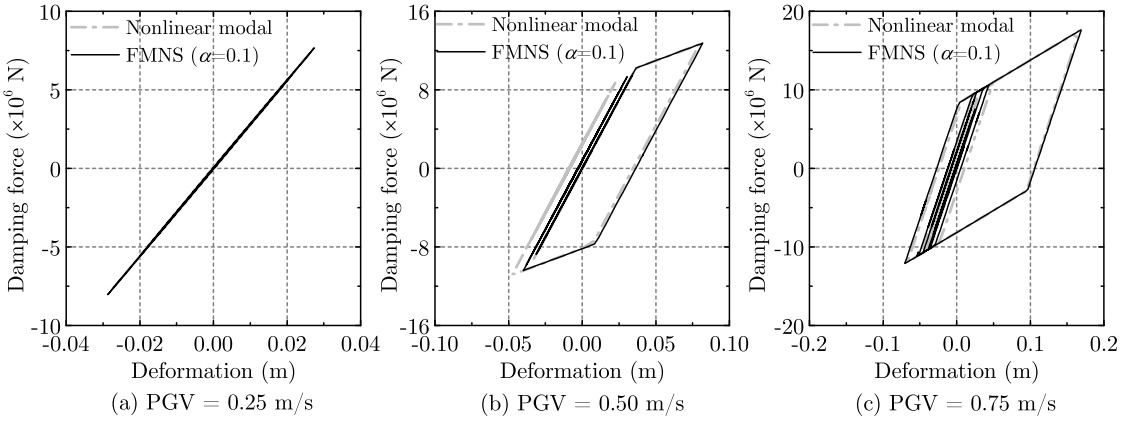

FIGURE 4.14: Hysteresis loops of the stiffness elements at the 1st story

those of the TSP system are obviously lower in terms of maximum floor response acceleration and relative displacement (except for PGV = 25 cm/s).

TABLE 4.5: Maximum seismic responses of differently damped structures

PGV (cm/s)	Damping model	Displacement (cm)	Interstory drift (cm)	Velocity (cm/s)	Acceleration (cm/s^2)
25	NLM	15.9	2.74	63.5	295
	TSP	16.2 (1.02)	2.67 (0.97)	62.9 (0.99)	230 (0.78)
	FMNS	15.4 (0.97)	2.88 (1.05)	67.1 (1.06)	300 (1.02)
50	NLM	34.4	7.97	1.07	531
	TSP	30.5 (0.89)	7.95 (1.00)	1.08 (1.01)	391 (0.73)
	FMNS	34.7 (1.01)	8.19 (1.03)	1.11 (1.04)	516 (0.97)
75	NLM	53.0	16.7	1.43	690
	TSP	47.8 (0.90)	15.8 (0.95)	1.38 (0.97)	587 (0.85)
	FMNS	55.0 (1.04)	16.9 (1.01)	1.47 (1.03)	697 (1.01)

Note: the number in the parenthesis means the ratio to the response of the NLM system.

Indeed, the simulation of inherent damping mechanism of structural elements (or materials), especially when the nonlinear behavior is involved, is a very complicated problem, which is still kept open for discussion. From the above comparison with the NLM model, however, one can at least conclude that the FMNS model, which can simulate the rate-independent dissipation behavior of many solid materials [23] over a considerable frequency range, is readily used as a candidate model for simulating the structural inherent damping in nonlinear simulation problems. Moreover, in terms of the accuracy of evaluating the structural seismic response, the FMNS model is comparable with the NLM model.

If the computational efficiency is concerned, e.g., for those large-scale simulation problems where thousands or more degree of freedoms are used in the numerical simulation, the proposed model is thought to be superior than the NLM model. In order to construct the modal damping matrix for the later, eigenvalue analyses are conducted at each iterative step, which is computational expensive for those problems. However, for the FMNS model, those time-consuming calculations for the modal characteristics are not necessary. For analyzing the example structure separately incorporated with the FMNS and NLM models subjected to the El Centro wave (with a time step of 0.004 s and a record length of 81.92 s), the total CPU times are 2.57 and 4.76 s, respectively, by running the codes on a computer with an Intel Core 7, 3.40 GHz with 16 GB RAM. For those large-scale simulation problems, the difference in computational efficiency is expected to much larger.

4.4.3 Parametric studies

In the above comparison studies, the tunable parameter α is fixed as 0.1 for application of the proposed FMNS model, and it has been shown that this contributes to a good approximation of the ideal RILD and it may be used as a competitive model to the Nakamura and NLM models for simulating the structural inherent damping. Here, parametric studies are

conducted to further investigate the effect of the tunable parameter α on the performance of the FMNS system subjected to different intensity-level earthquakes.

For this purpose, letting $\alpha = 0.10, 0.25, 0.50, 0.75, 1.0$, respectively, the FMNS model is used instead of the ideal RILD element in the ten-story example structure for simulating the structural inherent damping, and response history analyses are conducted by applying the recursive method on the basis of a Prony series with an order of 9 (i.e., $p = 9$), except for the case of $\alpha = 1.0$, where the proposed model reduces to a first-order system [49] (i.e., $p = 1$ is used in the recursive procedure). The ratio of the peak response of the structure to the case of $\alpha = 0.1$ is used as a performance index to indicate the sensitivity of the seismic performance of the structure with respect to the variation of the tunable parameter α.

Figs. 4.15-4.17 compare the peak response ratios of the FMNS system with different tunable parameters when subjected to the El Centro wave with a scaled PGV of 25, 50, 75 cm/s. It is shown that the response displacement of the structure is generally insensitive to the variation of the tunable parameter α, whereas the floor-response acceleration shows strong dependence on this parameter. The larger the tunable parameter α, the larger response ratios in terms of floor-response acceleration are observed. In the case of $\alpha = 1.0$, the largest response ratio in terms of floor-response acceleration can exceed 150%. This means that the floor-response acceleration of the structure may be obviously overestimated if the FMNS model with a large value of α (e.g., $\alpha \geq 0.5$) is used instead of the ideal RILD for simulating the structural inherent damping.

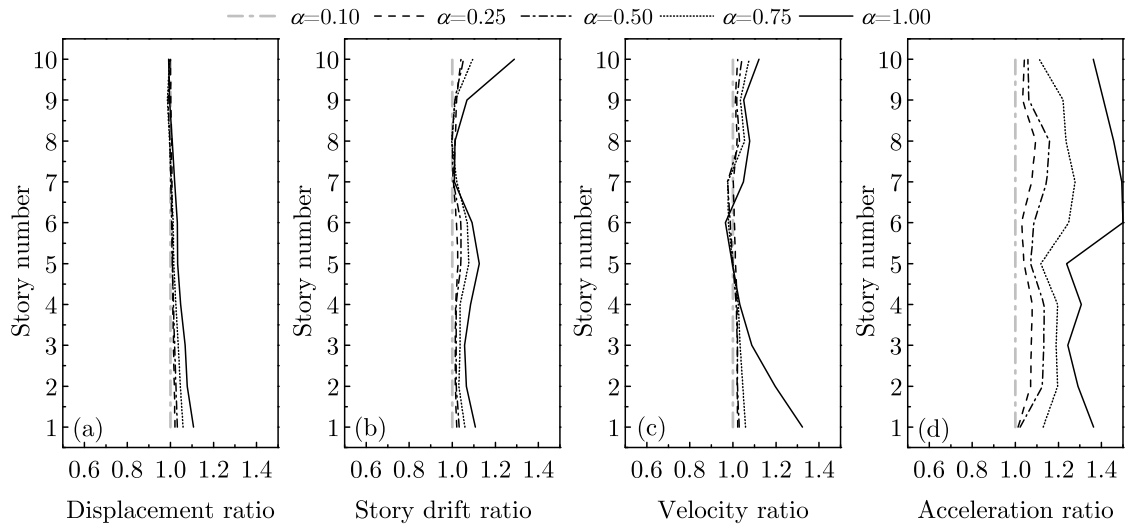

FIGURE 4.15: Peak response ratios of a structure with the proposed model (PGV=25 cm/s)

Recall that the closer to unity the tunable parameter α is, the lower loss modulus of the FMNS model has in the frequency range higher than the cutoff frequency (typically equal to the fundamental natural frequency), as shown in Fig. 3.3. In other words, with a value of α close to unity, the FMNS model results in an underestimated damping ratio at high modes of the structure by defining the damping functions in Eq.(4.49). Consequently, the high mode responses containing dominating high frequency components are overestimated, which is

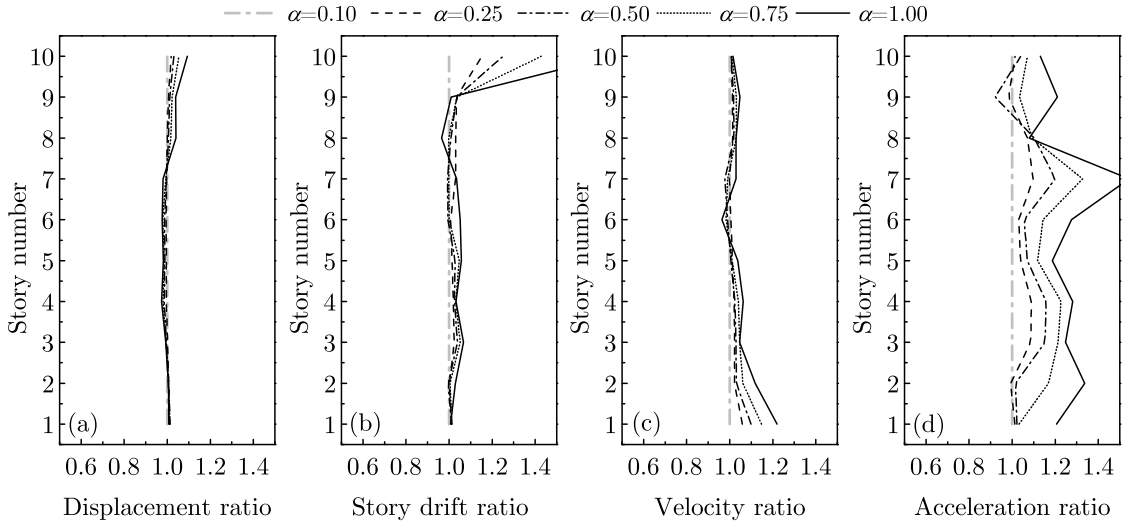

FIGURE 4.16: Peak response ratios of a structure with the proposed model (PGV=50 cm/s)

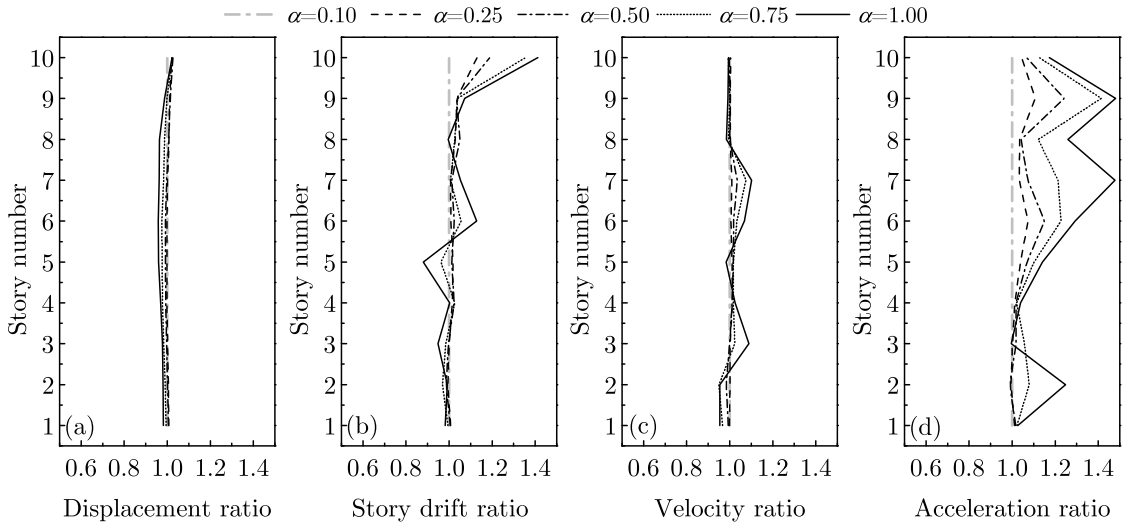

FIGURE 4.17: Peak response ratios of a structure with the proposed model (PGV=75 cm/s)

finally reflected in the analysis result of floor-response acceleration of the structure. This can be readily verified by comparing the Fourier amplitude spectra of the time histories of floor-response accelerations. For example, Fig. 4.18 compares the Fourier amplitude spectra of the time histories of floor-response accelerations at the seventh story (where the largest response ratio occurs) of the structure subjected to different intensity-level earthquakes. As expected above, it is observed from Fig. 4.18 that in the case of $\alpha = 1.0$, the structure with the FMNS model yields much larger responses in high frequency ranges when compared with the case of $\alpha = 0.1$.

Similarly, it is observed from Fig. 4.15-4.17 that the response ratio in terms of interstory drift at the rooftop of the structure also shows strong dependence on the tunable parameter

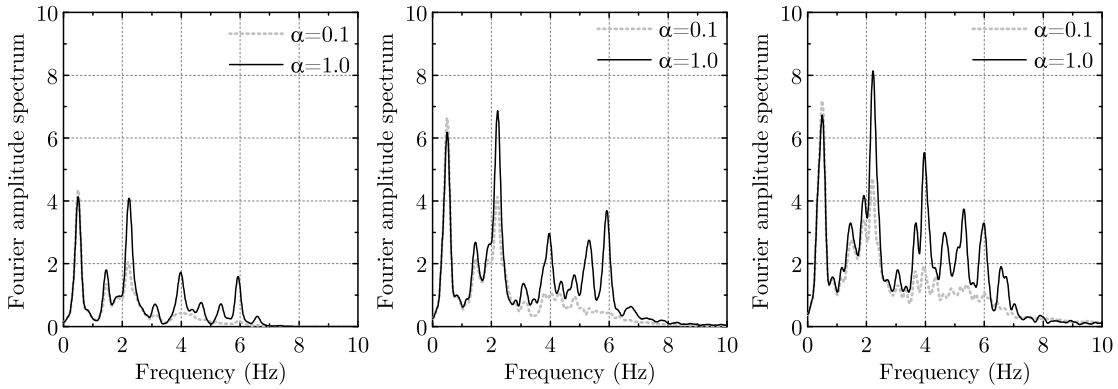

FIGURE 4.18: Fourier amplitude spectra of the floor response accelerations at the 7th story

α. This is also thought to be partly because larger tunable parameters result in underestimated damping ratios at high modes of the FMNS structural system.

Fig. 4.19 compares the hysteresis loops of the FMNS model with different tunable parameters at the top story of the structure. It is shown that compared with the case of PGV = 25 cm/s, the difference between the deformations of the two models are even larger when subjected to higher intensity-level earthquakes. It should be mentioned that the rapid change of damping force in Fig. 4.19 (b) and (c) suggests the state transformation of the structural bilinear stiffness element, because the damping force of the propose model is updated with the tangent stiffness of the structural element.

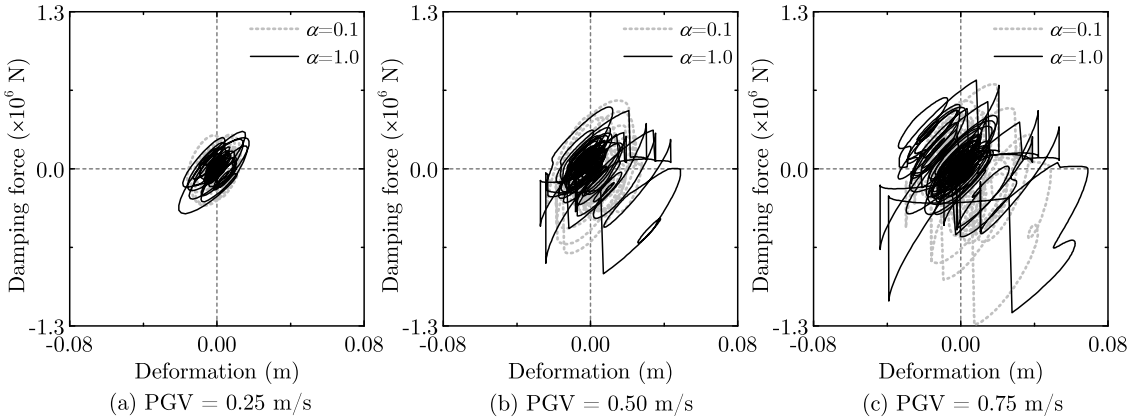

FIGURE 4.19: Hysteresis loops of the damping elements at the top story

For comparison, Fig.4.20 shows the hysteresis loops of the proposed models at the first story (where the largest interstory drift occurs) of the structure. Different from the seismic responses at higher stories, the displacement response at the first story is mostly dependent on the low mode responses. In both the cases of $\alpha = 0.1$ and $\alpha = 1.0$, the proposed models provide a good estimation of the first modal damping ratio. Therefore, in these two cases, the proposed models at the first story performs similarly, even when the structural element

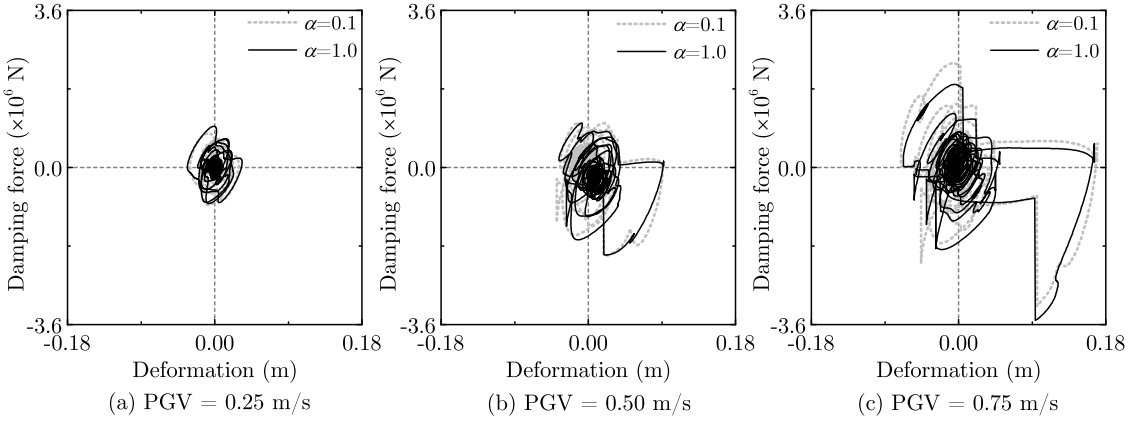

FIGURE 4.20: Hysteresis loops of the damping elements at the 1st story

yields under an excessive level earthquake (Fig. 4.20 (c)).

The above parametric studies suggest that for the application of the proposed FMNS model to simulate the structural inherent damping in an MDF structure, the tunable parameter α should be as a small value to control the accuracy of predicting the seismic responses of the structure, especially in terms of floor-response acceleration. For such applications, a value of $\alpha = 0.1$ is suggested so that the structural damping ratios at high modes can be properly specified. On one hand, an even smaller value of α may be used, but the improvement in the simulation accuracy is found to be limited. On the other hand, a much larger tunable parameter (e.g., $\alpha = 1.0$) results in the underestimated damping ratios at high modes, and consequently the seismic responses in terms of floor-response acceleration may be largely overestimated.

4.5 Chapter conclusions

In this chapter, time-domain methods for dynamic analyses of a structural model incorporated with RILD are discussed. The difficulty of applying the ideal RILD for nonlinear time history analyses is overcome by using the FMNS model proposed in Chapter 3 instead, and a computationally efficient recursive method is developed by using a Prony series to approximate the Mittag-Leffler relaxation function, which is the damping kernel function of the FMNS model. For practical applications, it is necessary to estimate the characteristic parameters of a Prony series, and to this end, both time- and frequency-domain methods are discussed. Comparison between the developed recursive method with the L1-algorithm-based method developed in Chapter 3 suggests that the former can be more computationally efficient without compromising the simulation accuracy.

In order to verify the effectiveness of the developed method, the application of the FMNS model for simulating the structural inherent damping is discussed. For this purpose, a ten-story benchmark building model is used as an analytical example. First, linear response history analyses are conducted to examine the seismic performance of the example structure separately incorporated with the ideal RILD, Nakamura models (an original one and

a modified one with increased storage modulus), and the FMNS model. Comparison studies between the seismic responses of these differently damped structures suggest that both the Nakamura and the FMNS models can be used as an good candidate for approximating the ideal RILD, and also these two causal models can be analyzed with comparable computational efficiencies. A potential advantage of the FMNS model over the Nakamura model may exist in the determination of the model tunable parameters for application in a low-frequency structure. For the Nakamura model, trial calculations may be required to determine those parameters for controlling the accuracy, which may be difficult for applications in low-frequency structures because this model may suffer relatively low accuracy in calculating the damping function in low frequency range by using the Hilbert transform. However, for the FMNS model, the model parameters can be readily determined for applications, and the damping function can be readily calculated without suffering low accuracy in low frequency region associated with the use of Hilbert transform.

Furthermore, the FMNS model is compared with the tangent stiffness proportional damping model and the nonlinear modal damping model for simulating the structural inherent damping. The seismic performance of the example structure separately incorporated with the three different damping models is examined by taking the nonlinearities of structural elements into account. The seismic responses of the three types of structures subjected to different intensity-level earthquakes are compared. It is shown that the FMNS model is comparable with the nonlinear modal damping model in terms of the simulation accuracy of structural seismic responses, but it is superior to the later in terms of computational efficiency for nonlinear time history analyses.

Lastly, parametric studies are conducted to investigate the effect of the tunable parameter α on the seismic performance of the FMNS structural system. It is suggested that for the application of the FMNS model to simulate the structural damping in an MDF structure, a small value of α (e.g., $\alpha = 0.1$ is suggested in this study) is preferred so that the structural damping ratios at high modes can be properly specified. A much larger value (e.g., $\alpha = 1.0$) may result in underestimated damping ratios at high modes, and consequently the seismic responses in terms of floor-response acceleration can be largely overestimated.

Chapter 5

Conclusions and Future Work

It is well known that rate-independent linear damping (RILD) suffers an issue of noncausality, which hinders its use for practical applications. On the one hand, although RILD is expected to be a straightforward model for the simulation of structural inherent damping, the noncausal property makes it challenging to numerically implement RILD in a nonlinear response history analysis for the performance evaluation of a building structure subjected to extreme ground motions. On the other hand, RILD is also found to have important applications for the seismic response control of a low-frequency structure, because it can achieve effective displacement reduction at the expense of lower damping force compared with other damping types, but because of its noncausality, it is impossible to physically realize RILD by using real-life devices, which can be installed in an actual building structure for seismic protection purposes.

5.1 Conclusions

In this dissertation, aimed at facilitating the practical applications of RILD in the above two situations, novel causal models which can mimic the behavior of an ideal RILD model were proposed. The main conclusions are drawn as follows,

1) For the purpose of seismic protection of a low-frequency structure subjected to strong ground motions, a causal passive mechanical model which consists of a conventional Maxwell element and a linear negative stiffness element coupled in parallel was proposed (labeled as MNS model). The proposed MNS model creates a time-domain representation of a bilinear digital filter, and is thought to be much simpler in the senses of both physical realization and numerical simulation compared with existing causal models. In order to physically realize the MNS model for practical applications, one can readily create a conventional Maxwell element by arranging an oil damper and a coil spring coupled in series, and equivalently create a linear negative stiffness element by reducing the horizontal stiffnesses of the primary structure (or isolators). Alternatively, a passive device which creates linear negative stiffness within the deformation range of interest was also designed, making the MNS model more attractive for mimicking the behavior of an ideal RILD model. Furthermore, comparisons between the seismic responses of five-story base-isolated structures incorporated with the MNS and linear viscous damping models exemplified the feasibility of the MNS model to

mimic ideal RILD in reducing the floor-response acceleration without increasing the displacement. Therefore, the proposed MNS model is expected to be a viable option for improving the seismic performance of low-frequency structures subjected to strong ground motions.

2) By generalizing the bilinear digital filter into a fractional-order one, a novel causal model was proposed for achieving an improved approximation of the ideal RILD model in the sense of an extended frequency range, over which the rate-independent dissipation behavior may be tracked by adjusting a tunable parameter (say α). Such a model can be represented by a fractional-order Maxwell element coupled in parallel with a linear negative stiffness element(labeled as FMNS model), which is a generalization of the MNS model. Both passive and semi-active methods were suggested to physically realize the FMNS model. Furthermore, the relationships between the FMNS model with existing causal models for RILD (e.g., Biot, Makris, Maxwell-Wiechart, and Keivan models) are revealed and proved. It is suggested that the FMNS model can be considered as a unified causal model for RILD because it can encompass other existing causal models. On the basis of the newly revealed relationships between different causal models and the well established ones, a unified framework of causal models for RILD was constructed. For numerical implementation of the FMNS model, a time-domain analysis method was developed by directly calculating the fractional derivative on the basis of the so-called L1 algorithm, and the computational efficiency can be largely improved without significant loss of accuracy if the fixed memory principle is applied. Comparisons between the seismic responses of five-story base-isolated structures incorporated with different causal RILD models suggested that the FMNS model with $\alpha = 1$ (i.e. the MNS model) can be used as a simple option to approximate the behavior of ideal RILD for use in a nonlinear base-isolation system, and the seismic performance of the structure is not compromised when compared with other more complicated causal RILD models.

3) For further accelerating the dynamic analysis of a structural model with the FMNS model, a recursive method was developed by using a Prony series to approximate the damping kernel of the FMNS model in terms of Mittag-Leffler relaxation function, which can avoid the calculation of the fractional derivative for response history analyses. The developed method can be readily embedded into the established numerical integration schemes for response history analyses of an MDF system. For practical application of this method, both time- and frequency-domain methods were discussed to estimate the characteristic parameters of a Prony series. Moreover, it was shown that this recursive method can be more computationally efficient than the L1-algorithm-based method without compromising the simulation accuracy. In terms of application of the FMNS model for simulating the structural inherent damping, a ten-story benchmark building model was used as an analytical example with the nonlinearities

of structural stiffness elements taken into account. Comparisons between the performance of the FMNS model with those of the ideal RILD, Nakamura, tangent stiffness proportional, and nonlinear modal damping models were made when they were separately incorporated into the example structure to simulate the structural inherent damping. It is suggested that the FMNS model can be used as a competitive candidate for simulating the structural inherent damping when compared with the Nakamura and nonlinear modal damping models. Furthermore, parametric studies were conducted to investigate the effect of the tunable parameter α on the seismic performance of the FMNS system. It was suggested that in terms of application for simulating the structural inherent damping, the FMNS model with $\alpha = 1$ (i.e. the MNS model) may largely overestimate the seismic responses in terms of floor-response acceleration because of underestimated damping ratios at high modes. Therefore, a much smaller tunable parameter (e.g., $\alpha = 0.1$) was recommended for this application so that the structural damping ratios at high modes can be properly specified.

5.2 Future work

5.2.1 Further performance improvement on the MNS model

In terms of application of RILD for seismic protection of a base-isolated structure subjected to strong ground motions, the simple MNS model is expected to be a viable option without compromising the seismic performance, when compared with other more complicated causal RILD models. However, it should be noted that this model may suffer limited capability of the displacement control of a low-frequency structure subjected to extreme ground motions containing dominating low-frequency components.

For the development of MNS model, a linear negative stiffness element (LNSE) is thought to play a critical role. It can either be conceptually created by equivalently reducing the horizontal stiffness of primary structure (or of isolator), or be physically implemented by using some passive negative stiffness devices. To mimic the behavior of RILD, the stiffness of an LNSE should be dependent on the required damping ratio to achieve a specified performance target. However, to avoid the structural instability, the stiffness (absolute value) of an LNSE should be at most not larger than that of the primary structure (or of isolator). This implies that there is a limiting damping ratio, say ξ_{lim}, for applying the MNS model for seismic control. In frequent earthquake events, a relatively small damping ratio may be used to constraint the isolator deformation within an acceptable range; however, in a severe earthquake event, a damping ratio larger than ξ_{lim} may be demanded to achieve this goal, and the resulting LNSE may provide a stiffness (absolute value) larger than that of the primary structure, resulting in a problem of structural instability. This suggests that the MNS model may fail to provide further deformation reduction beyond this limit. Therefore, further efforts are necessary to be made to overcome this challenge and improve the performance of the MNS model for seismic protection of a low-frequency structure subjected to extreme earthquake events.

5.2.2 Physical realization of the FMNS model

The FMNS model consists of a fractional-order Maxwell element coupled in parallel with an LNSE. In terms of its physical realization, the remaining challenge is to physically realize a fractional-order Maxwell element. One may develop novel real-life damping devices on the basis of the reported experiments on some devices and materials, which were simulated by using such a fractional model. Alternatively, one can also passively realize the FMNS model in an equivalent manner. The equivalence between the FMNS model with the TMW model suggests that one may passively realize the FMNS model by developing a combination system consisting of multiple damping devices coupled with each other in parallel, which can be readily realized in practical applications. Several alternative damping devices are available for this purpose, and the Maxwell element can be competitive due to its simplicity, and also the corresponding design method is well established and discussed in this dissertation.

One can also physically realize the FMNS model by employing semi-active devices, which can generate the desired damping force by the FMNS model. For this purpose, an efficient time-domain analysis technique is required to numerically implement the FMNS model. The L1-algorithm-based method may be readily used and the computational efficiency can be largely improved by applying the fixed memory principle without significant loss of accuracy. Furthermore, it is worth noting that more advanced algorithms are also available to permit the variation of step length, or the application of spectral methods for high order (in accuracy) simulations. However, it may be still challenging to embed those advanced methods into the established numerical integration schemes (e.g., Newmark integration scheme).

5.2.3 Application of RILD in a high-rise building structure

In this study, to illustrate the application of the FMNS model for the simulation of structural inherent damping, a ten-story benchmark building structure is used as an analytical example. The nonlinearity of the structural element is considered by using a bilinear stiffness element, which may be not typically used in the design practice. Typical and refined models to take the nonlinearities of structural stiffness elements in account will be used in the future work.

The seismic performance of a high-rise building structure incorporated with RILD is of particular interest in the future work for both the purposes of seismic response control and simulation of structural inherent damping. In both cases, the methods developed in this study can be readily used to conduct response history analyses. Moreover, the application of RILD for the vibration control of high-rise building structure in various loading conditions (earthquake, wind, or blast loading, and so on) may also be explored. For this purpose, a design method for optimal placement of the damping devices in the structural may also be necessary.

Bibliography

[1] I Takewaki, S Murakami, K Fujita, S Yoshitomi, and M Tsuji. "The 2011 off the Pacific coast of Tohoku earthquake and response of high-rise buildings under long-period ground motions". In: *Soil Dynamics and Earthquake Engineering* 31.11 (2011), pp. 1511–1528.

[2] Nobuo Mimura, Kazuya Yasuhara, Seiki Kawagoe, Hiromune Yokoki, and So Kazama. "Damage from the Great East Japan Earthquake and Tsunami-a quick report". In: *Mitigation and Adaptation Strategies for Global Change* 16.7 (2011), pp. 803–818.

[3] Masanori Iiba, Tatsuya Azuhata, Namihiko Inoue, and Shigeru Hirano. "Behavior of seismically isolated structures for houses by the 2011 off the Pacific coast of Tohoku earthquake, Part 2: Field investigation and correction between displacement and ground motion". In: *Proceedings of the Annual Meeting by Architecture institute of Japan (AIJ), Nagoya, Japan*. 2012 (in Japanese).

[4] Masato Motosaka and Kazuya Mitsuji. "Building damage during the 2011 off the Pacific coast of Tohoku Earthquake". In: *Soils and foundations* 52.5 (2012), pp. 929–944.

[5] N. Inoue and Ikago K. *Displacement control design of buildings*. Maruzen Publishing Co.,Ltd., 2012 (in Japanese).

[6] Kohju Ikago and Norio Inoue. "Behavior of rate-independent linear damping incorporated into long-period structures subjected to strong ground motions". In: *Proceedings of the 6th World Conference on Structural Control and Monitoring, Barcelona, Spain*. 2014, pp. 1116–1124.

[7] Anil K Chopra. *Dynamics of structures: theory and applications to earthquake engineering*. Vol. 2. Prentice Hall Englewood Cliffs, NJ, 1995.

[8] Charles W Bert. "Material damping: An introductory review of mathematic measures and experimental technique". In: *Journal of Sound and Vibration* 29.2 (1973), pp. 129–153.

[9] B Lord Rayleigh J W S. *The Theory of Sound*. Vol. 1. London, Macmillan and co., 1877.

[10] Dionisio Bernal. "Viscous damping in inelastic structural response". In: *Journal of Structural Engineering* 120.4 (1994), pp. 1240–1254.

[11] John F Hall. "Problems encountered from the use (or misuse) of Rayleigh damping". In: *Earthquake engineering and structural dynamics* 35.5 (2006), pp. 525–545.

[12] Finley A Charney. "Unintended consequences of modeling damping in structures". In: *Journal of structural engineering* 134.4 (2008), pp. 581–592.

[13] Farzin Zareian and Ricardo A Medina. "A practical method for proper modeling of structural damping in inelastic plane structural systems". In: *Computers and structures* 88.1-2 (2010), pp. 45–53.

[14] Anil K Chopra and Frank McKenna. "Modeling viscous damping in nonlinear response history analysis of buildings for earthquake excitation". In: *Earthquake Engineering and Structural Dynamics* 45.2 (2016), pp. 193–211.

[15] Naohiro Nakamura. "Extended Rayleigh damping model". In: *Frontiers in Built Environment* 2 (2016), p. 14.

[16] Naohiro Nakamura. "Time history response analysis using extended Rayleigh damping model". In: *Procedia engineering* 199 (2017), pp. 1472–1477.

[17] J Enrique Luco and Armando Lanzi. "A new inherent damping model for inelastic time-history analyses". In: *Earthquake Engineering and Structural Dynamics* 46.12 (2017), pp. 1919–1939.

[18] John F Hall. "Performance of viscous damping in inelastic seismic analysis of moment-frame buildings". In: *Earthquake Engineering and Structural Dynamics* 47.14 (2018), pp. 2756–2776.

[19] William Thomson Kelvin. *Elasticity and heat*. A. and C. Black, 1880.

[20] Bertram Hopkinson and Trevor G Williams. "The elastic hysteresis of steel". In: *Proceedings of the Royal Society of London. Series A, Containing Papers of a Mathematical and Physical Character* 87.598 (1912), pp. 502–511.

[21] FE Rowett. "Elastic hysteresis in steel". In: *Proceedings of the Royal Society of London. Series A, Containing Papers of a Mathematical and Physical Character* 89.614 (1914), pp. 528–543.

[22] George A Lindsay. "A study of the longitudinal vibration of wires". In: *Physical Review* 3.6 (1914), p. 397.

[23] AL Kimball and DE Lovell. "Internal friction in solids". In: *Physical Review* 30.6 (1927), p. 948.

[24] BJ Lazan. "A study with new equipment of the effects of fatigue stress on the damping capacity and elasticity of mild steel". In: *Transactions of American Society for Metals* (1950), pp. 499–558.

[25] Red Bishop. "The treatment of damping forces in vibration theory". In: *Journal of the Royal Aeronautical Society* 59.539 (1955), pp. 738–742.

[26] TJ Reid. "Free vibration and hysteretic damping". In: *The Aeronautical Journal* 60.544 (1956), pp. 283–283.

[27] P Lancaster. "Free vibration and hysteretic damping". In: *The Aeronautical Journal* 64.592 (1960), pp. 229–229.

[28] Stephen H Crandall. *Dynamic response of systems with structural damping*. Tech. rep. Massachusetts Institute of Technology, Cambridge, Massachusetts, 1961.

[29] William Jolly Duncan and HM Lyon. *Calculated flexural-torsional flutter characteristics of some typical cantilever wings*. Aeronautical Research Committee, 1937.

[30] Theodore Theodorsen. "Mechanism of flutter, a theoretical and experimental investigation of the flutter problem". In: *NACA Report 689* (1940).

[31] M. A. Biot. "Linear thermodynamics and the mechanics of solids". In: Proceedings of the 3rd U.S. National Congress of Applied Mechanics, ASME, New York. 1958, pp. 1–18.

[32] TK Caughey. "Vibration of dynamic system with linear hysteretic damping (linear theory)". In: *Proceedings of 4th U.S. National Congress of Applied Mechanics, 1962*. Vol. 1. ASCE. 1962, pp. 87–97.

[33] G Genta and N Amati. "On the equivalent viscous damping for systems with hysteresis". In: *Atti della Accademia delle Scienze di Torino* 32 (2009), pp. 21–43.

[34] Anna Reggio and Maurizio De Angelis. "Modelling and identification of structures with rate-independent linear damping". In: *Meccanica* 50.3 (2015), pp. 617–632.

[35] Ronald L Bagley and J Torvik. "Fractional calculus-a different approach to the analysis of viscoelastically damped structures". In: *AIAA journal* 21.5 (1983), pp. 741–748.

[36] L Gaul, P Klein, and S Kemple. "Damping description involving fractional operators". In: *Mechanical Systems and Signal Processing* 5.2 (1991), pp. 81–88.

[37] HK Milne. "The impulse response function of a single degree of freedom system with hysteretic damping". In: *Journal of Sound Vibration* 100 (1985), pp. 590–593.

[38] Jose A Inaudi and James M Kelly. "Linear hysteretic damping and the Hilbert transform". In: *Journal of Engineering Mechanics* 121.5 (1995), pp. 626–632.

[39] Jose A Inaudi and Nicos Makris. "Time-domain analysis of linear hysteretic damping". In: *Earthquake Engineering and Structural Dynamics* 25.6 (1996), pp. 529–546.

[40] Nicos Makris. "The causal hysteretic element". In: *Journal of engineering mechanics* 123.11 (1997), pp. 1209–1214.

[41] Nicos Makris and Jian Zhang. "Time-domain viscoelastic analysis of earth structures". In: *Earthquake Engineering and Structural Dynamics* 29.6 (2000), pp. 745–768.

[42] Pol D Spanos and Spyro Tsavachidis. "Deterministic and stochastic analyses of a nonlinear system with a Biot visco-elastic element". In: *Earthquake engineering and structural dynamics* 30.4 (2001), pp. 595–612.

[43] Giuseppe Muscolino, Alessandro Palmeri, and Francesco Ricciardelli. "Time-domain response of linear hysteretic systems to deterministic and random excitations". In: *Earthquake engineering and structural dynamics* 34.9 (2005), pp. 1129–1147.

[44] Naohiro Nakamura. "Improved methods to transform frequency-dependent complex stiffness to time domain". In: *Earthquake engineering and structural dynamics* 35.8 (2006), pp. 1037–1050.

[45] Naohiro Nakamura. "Practical causal hysteretic damping". In: *Earthquake Engineering and Structural Dynamics* 36.5 (2007), pp. 597–617.

[46] Anna Reggio, Maurizio De Angelis, and Raimondo Betti. "A state-space methodology to identify modal and physical parameters of non-viscously damped systems". In: *Mechanical Systems and Signal Processing* 41.1-2 (2013), pp. 380–395.

[47] Ashkan Keivan, Brian M Phillips, Masahiro Ikenaga, and Kohju Ikago. "Causal realization of rate-independent linear damping for the protection of low-frequency Structures". In: *Journal of Engineering Mechanics* 143.9 (2017), p. 04017058.

[48] Ashkan Keivan, Brian M Phillips, and Kohju Ikago. "Adaptive causal realization of rate-independent linear damping". In: *Engineering Structures* 167 (2018), pp. 256–271.

[49] H Luo, C Chong, K Ikago, A Keivan, and BM Phillips. "Passive implementation of rate-independent linear damping using a negative stiffness element". In: Proceedings of the 11th U.S. National Conference in Earthquake Engineering, Earthquake Engineering Research Institute, Los Angeles, CA. 2018.

[50] H Luo, K Ikago, C Chong, A Keivan, and BM Phillips. "Performance of low-frequency structures incorporated with rate-independent linear damping". In: *Engineering Structures* 181 (2019), pp. 324–335.

[51] Yuli Huang, Richard Sturt, and Michael Willford. "A damping model for nonlinear dynamic analysis providing uniform damping over a frequency range". In: *Computers and Structures* 212 (2019), pp. 101–109.

[52] F Mastroddi, F Martarelli, M Eugeni, and C Riso. "Time-and frequency-domain linear viscoelastic modeling of highly damped aerospace structures". In: *Mechanical Systems and Signal Processing* 122 (2019), pp. 42–55.

[53] Nicos Makris and MC Constantinou. "Fractional-derivative Maxwell model for viscous dampers". In: *Journal of Structural Engineering* 117.9 (1991), pp. 2708–2724.

[54] Pol D Spanos and Georgios I Evangelatos. "Response of a non-linear system with restoring forces governed by fractional derivatives—Time domain simulation and statistical linearization solution". In: *Soil Dynamics and Earthquake Engineering* 30.9 (2010), pp. 811–821.

[55] Keith Oldham and Jerome Spanier. *The fractional calculus theory and applications of differentiation and integration to arbitrary order*. Vol. 111. Elsevier, 1974.

[56] Nicos Makris. "Rigidity-plasticity-viscosity: can electrorheological dampers protect base-isolated structures from near-source ground motions?" In: *Earthquake Engineering and Structural Dynamics* 26.5 (1997), pp. 571–592.

[57] Nicos Makris and Shih-Po Chang. "Effect of viscous, viscoplastic and friction damping on the response of seismic isolated structures". In: *Earthquake Engineering and Structural Dynamics* 29.1 (2000), pp. 85–107.

[58] WL He, AK Agrawal, and JN Yang. "Novel semiactive friction controller for linear structures against earthquakes". In: *Journal of Structural Engineering* 129.7 (2003), pp. 941–950.

[59] Jose A Inaudi. "Modulated homogeneous friction: a semi-active damping strategy". In: *Earthquake Engineering and Structural Dynamics* 26.3 (1997), pp. 361–376.

[60] T J Nashif, I G Jones, and J P Henderson. *Vibration damping*. Wiley, New York, 1988.

[61] TK Caughey and A Vijayaraghavan. "Free and forced oscillations of a dynamic system with "linear hysteretic damping"(non-linear theory)". In: *International Journal of Non-Linear Mechanics* 5.3 (1970), pp. 533–555.

[62] SH Crandall. "The hysteretic damping model in vibration theory". In: *Proceedings of the Institution of Mechanical Engineers, Part C: Mechanical Engineering Science* 205.1 (1991), pp. 23–28.

[63] Jose A Inaudi and James M Kelly. "Linear hysteretic damping and the Hilbert transform". In: *Journal of Engineering Mechanics* 121.5 (1995), pp. 626–632. ISSN: 0733-9399.

[64] Erik H Vanmarcke. "Properties of spectral moments with applications to random vibration". In: *Journal of the engineering mechanics division* 98.2 (1972), pp. 425–446.

[65] Gokhan Pekcan, John B Mander, and Stuart S Chen. "Fundamental considerations for the design of non-linear viscous dampers". In: *Earthquake engineering and structural dynamics* 28.11 (1999), pp. 1405–1425. ISSN: 1096–9845.

[66] Kang-Min Choi, Hyung-Jo Jung, Heon-Jae Lee, and Sang-Won Cho. "Seismic protection of base-isolated building with nonlinear isolation system using smart passive control strategy". In: *Structural Control and Health Monitoring* 15.5 (2008), pp. 785–796.

[67] G Yang, BF Spencer, JD Carlson, and MK Sain. "Large-scale MR fluid dampers: modeling and dynamic performance considerations". In: *Engineering structures* 24.3 (2002), pp. 309–323.

[68] F Weber and M Maślanka. "Precise stiffness and damping emulation with MR dampers and its application to semi-active tuned mass dampers of Wolgograd Bridge". In: *Smart Materials and Structures* 23.1 (2013), p. 015019.

[69] Alan Sternberg, René Zemp, and Juan Carlos de la Llera. "Multiphysics behavior of a magneto-rheological damper and experimental validation". In: *Engineering Structures* 69 (2014), pp. 194–205.

[70] Lyan-Ywan Lu, Ging-Long Lin, and Ming-Hsiang Shih. "An experimental study on a generalized Maxwell model for nonlinear viscoelastic dampers used in seismic isolation". In: *Engineering Structures* 34 (2012), pp. 111–123.

[71] Apostolos A Sarlis, Dharma Theja R Pasala, MC Constantinou, AM Reinhorn, Satish Nagarajaiah, and DP Taylor. "Negative stiffness device for seismic protection of structures". In: *Journal of Structural Engineering* 139.7 (2012), pp. 1124–1133.

[72] Tong Sun, Zhilu Lai, Satish Nagarajaiah, and Hong-Nan Li. "Negative stiffness device for seismic protection of smart base isolated benchmark building". In: *Structural Control & Health Monitoring* 7 (2017), e1968.

[73] H Luo, Y Hanzawa, and K Ikago. "Seismic performance enhancement of a base-isolation structure by using a passive rate-independent damping model". In: *Proceedings of the 7th Asia Conference on Earthquake Engineering, Bangkok, Thailand*. 2018, pp. 1–8.

[74] Andrew Gemant. "A method of analyzing experimental results obtained from elasto-viscous bodies". In: *Physics* 7.8 (1936), pp. 311–317.

[75] M Caputo and F Mainardi. "A new dissipation model based on memory mechanism". In: *Pure and applied Geophysics* 91.1 (1971), pp. 134–147.

[76] Ronald L Bagley and Peter J Torvik. "On the fractional calculus model of viscoelastic behavior". In: *Journal of Rheology* 30.1 (1986), pp. 133–155.

[77] Michael J Lighthill, Michael James Lighthill, et al. *An introduction to Fourier analysis and generalised functions*. Cambridge University Press, 1958.

[78] Izrail Solomonovich Gradshteyn and Iosif Moiseevich Ryzhik. *Table of integrals, series, and products*. Academic press, 2014.

[79] N Makris. "Stiffness, flexibility, impedance, mobility, and hidden delta function". In: *Journal of engineering mechanics* 123.11 (1997), pp. 1202–1208.

[80] Alekseĭ Ivanovich Markushevich. *Theory of functions of a complex variable*. Vol. 296. American Mathematical Society, 2005.

[81] Mário N Berberan-Santos. "Properties of the Mittag-Leffler relaxation function". In: *Journal of Mathematical Chemistry* 38.4 (2005), pp. 629–635.

[82] Chan Ghee Koh and James M Kelly. "Application of fractional derivatives to seismic analysis of base-isolated models". In: *Earthquake engineering and structural dynamics* 19.2 (1990), pp. 229–241.

[83] Stefan G Samko, Anatoly A Kilbas, and Oleg I Marichev. "Fractional integrals and derivatives: theory and applications". In: (1993).

[84] Igor Podlubny. *Fractional differential equations: an introduction to fractional derivatives, fractional differential equations, to methods of their solution and some of their applications*. Elsevier, 1998.

[85] Kai Diethelm. "Numerical approximation of finite-part integrals with generalised compound quadrature formula". In: *IMA Journal of Numerical Analysis* 17 (1997), pp. 479–493.

[86] Neville J Ford and A Charles Simpson. "The numerical solution of fractional differential equations: speed versus accuracy". In: *Numerical Algorithms* 26.4 (2001), pp. 333–346.

[87] Hiroshi Nasuno and Nobuyuki Shimizu. "Power time numerical integration algorithm for nonlinear fractional differential equations". In: *Journal of Vibration and control* 14.9-10 (2008), pp. 1313–1332.

[88] Eid H Doha, Ali H Bhrawy, and SS Ezz-Eldien. "Efficient Chebyshev spectral methods for solving multi-term fractional orders differential equations". In: *Applied Mathematical Modelling* 35.12 (2011), pp. 5662–5672.

[89] Nicholas Hale and Alex Townsend. "Fast and accurate computation of Gauss–Legendre and Gauss–Jacobi quadrature nodes and weights". In: *SIAM Journal on Scientific Computing* 35.2 (2013), A652–A674.

[90] Lijing Zhao and Weihua Deng. "Jacobian-predictor-corrector approach for fractional differential equations". In: *Advances in Computational Mathematics* 40.1 (2014), pp. 137–165.

[91] Nicholas Hale and Sheehan Olver. "A fast and spectrally convergent algorithm for rational-order fractional integral and differential equations". In: *SIAM Journal on Scientific Computing* 40.4 (2018), A2456–A2491.

[92] Giancarlo Genta and Nicola Amati. "Hysteretic damping in rotordynamics: An equivalent formulation". In: *Journal of Sound and Vibration* 329.22 (2010), pp. 4772–4784.

[93] S Lawrence Marple Jr. *Digital spectral analysis with applications*. Englewood Cliffs, NJ, Prentice-Hall, Inc., 1987.

[94] Sondipon Adhiakri. "Classical normal modes in nonviscously damped linear systems". In: *AIAA journal* 39.5 (2001), pp. 978–980.

[95] Michael A. Jenkins. "Algorithm 493: Zeros of a real polynomial [c2]". In: *ACM Transactions on Mathematical Software (TOMS)* 1.2 (1975), pp. 178–189.

[96] SMFD Syed Mustapha and TN Phillips. "A dynamic nonlinear regression method for the determination of the discrete relaxation spectrum". In: *Journal of Physics D: Applied Physics* 33.10 (2000), p. 1219.